



Jesús Daniel Fernández Escalante

**Relative permeability measurement and
two-phase flow visualization in micromodels of
vugular porous media**

Dissertação de Mestrado

Dissertation presented to the Programa de Pós-graduação em Engenharia Mecânica of PUC-Rio in partial fulfillment of the requirements for the degree of Mestre em Engenharia Mecânica.

Advisor : Prof. Márcio da Silveira Carvalho
Co-advisor: Dr. Jorge Antonio Avendaño Benavides

Rio de Janeiro
April 2023



Jesús Daniel Fernández Escalante

**Relative permeability measurement and
two-phase flow visualization in micromodels of
vugular porous media**

Dissertation presented to the Programa de Pós-graduação em Engenharia Mecânica of PUC-Rio in partial fulfillment of the requirements for the degree of Mestre em Engenharia Mecânica. Approved by the Examination Committee.

Prof. Márcio da Silveira Carvalho

Advisor

Departamento de Engenharia Mecânica – PUC-Rio

Dr. Jorge Antonio Avendaño Benavides

Co-advisor

Departamento de Engenharia Mecânica – PUC-Rio

Prof. Tanguy Le Borgne

Conseil National des Astronomes et Physiciens (CNAP) –
University of Rennes

Prof. Vladimir Alvarado Basante

Department of Chemical Engineering – University of Wyoming

Rio de Janeiro, April the 18th, 2023

All rights reserved.

Jesús Daniel Fernández Escalante

Bachelor's degree in Chemical Engineering from Universidad de Los Andes (Venezuela) in 2017

Bibliographic data

Fernández Escalante, Jesús Daniel

Relative permeability measurement and two-phase flow visualization in micromodels of vugular porous media / Jesús Daniel Fernández Escalante; advisor: Márcio da Silveira Carvalho; co-advisor: Jorge Antonio Avendaño Benavides. – 2023.

99 f.: il. color. ; 30 cm

Dissertation (master's degree) - Pontifícia Universidade Católica do Rio de Janeiro, Department of Mechanical Engineering, 2023

Includes bibliography

1. Engenharia Mecânica – Thesis. 2. Vugular porous media;. 3. PDMS-glass micromodels;. 4. Two-phase flow;. 5. Relative permeability;. 6. Microfluidics;. I. Carvalho, Márcio. II. Avendaño Benavides, Jorge Antonio. III. Pontifícia Universidade Católica do Rio de Janeiro. Department of Mechanical Engineering. IV. Title.

CDD: 621

Acknowledgments

The present work is the result of a long journey of learning and working, during which I have experienced support in many ways for which I am grateful.

I thank God, the source of all life and knowledge, Jesus Christ His Son, the source of all love and goodness, and the Holy Spirit, the impetus of all our searching and the source of all power.

I thank my parents who have guided me on the path of the search for truth and who have laid the foundations of my life, my actions and my feelings.

I thank my academic advisor Professor Márcio Carvalho and co-advisor Jorge Avendaño for their excellent guidance, dedication and commitment in the formulation, development, and review of this work.

I thank the researchers of the Laboratory of Microhydrodynamics and Flow in Porous Media (LMMP), who were always willing to contribute their experience to the further development of my work.

I thank my friends Andrea Mora, Amanda Pessoa, Clarice de Amorim, Vivian Mendes, Carlos Sánchez and Pedro Calderano, who made my path easier and in whose friendship I found a treasure.

Last, but not least, I thank the Pontifical Catholic University of Rio de Janeiro, which has scientifically trained generations of professionals and fostered their human development. In the community of its professors and students, I was able to learn a new language and get to know the *joie de vivre* and genuine values of Brazilian culture.

This study was financed in part by the Coordenação de Aperfeiçoamento de Pessoal de Nível Superior - Brasil (CAPES) - Finance Code 001.

Abstract

Fernández Escalante, Jesús Daniel; Carvalho, Márcio (Advisor); Avendaño Benavides, Jorge Antonio (Co-Advisor). **Relative permeability measurement and two-phase flow visualization in micromodels of vugular porous media**. Rio de Janeiro, 2023. 99p. Dissertação de mestrado – Departamento de Engenharia Mecânica, Pontifícia Universidade Católica do Rio de Janeiro.

It is estimated that 50% of world's oil and gas reserves are held in naturally fractured carbonate reservoirs. One of the biggest challenges in this type of formation is its heterogeneous nature. Besides the presence of fractures that longitudinally connect the porous medium, vugs at different scales and distributions are scattered throughout the porous matrix. These cavities cause fluid flow characteristics to significantly differ from those of conventional homogeneous pore structure reservoirs and bring the need to evaluate equivalent petrophysical properties of the heterogeneous medium. In this study, a microfluidic approach is used to determine the water and oil relative permeability curves and phase distribution profiles in 2D micromodels of vugular porous media. Steady-state water-oil injection experiments were performed in these devices at different fractional flows, while monitoring the dynamics of the pressure drop and visualizing the fluid displacement at the pore scale. Live-image acquisition through fluorescence microscopy made it possible to examine the evolution of the saturation of water and oil phases. The direct comparison between the relative permeability curves of well-characterized vugular porous media and their porous matrix showed that the incorporation of vugs leads to (i) higher equivalent absolute permeability, especially with longer cavities and higher vug density, (ii) increased oil occupancy in the porous matrix, due to less efficient water invasion into the porous matrix, and (iii) higher relative permeability to water, which flows preferentially through the vugular space. These results are consistent with the oil-wet nature of micromodels, since the vugs are offering less capillary resistance to the flow of the non-wetting phase. Our low-cost microfluidic approach will likely allow us to systematically study more complex vugular-fractured systems.

Keywords

Vugular porous media; PDMS-glass micromodels; Two-phase flow; Relative permeability; Microfluidics;

Resumo

Fernández Escalante, Jesús Daniel; Carvalho, Márcio; Avendaño Benavides, Jorge Antonio. **Medição da permeabilidade relativa e visualização do escoamento de duas fases em micromodelos de meios porosos vugulares**. Rio de Janeiro, 2023. 99p. Dissertação de Mestrado – Departamento de Engenharia Mecânica, Pontifícia Universidade Católica do Rio de Janeiro.

Estima-se que 50% das reservas mundiais de petróleo e gás sejam mantidas em reservatórios carbonáticos naturalmente fraturados. Um dos maiores desafios neste tipo de formações é a sua heterogeneidade. Além da presença de fraturas que conectam longitudinalmente o meio poroso, *vugs* em diferentes escalas e distribuições estão espalhados por toda a matriz porosa. Essas cavidades tornam as características do escoamento de fluidos significativamente diferentes daquelas dos reservatórios convencionais de estrutura porosa homogênea, e trazem a necessidade de avaliar propriedades petrofísicas equivalentes para o meio heterogêneo. Neste estudo, uma abordagem microfluídica é usada para determinar as curvas de permeabilidade relativa de água e óleo e os perfis de distribuição das fases em micromodelos 2D de meios porosos vugulares. Experimentos de injeção simultânea de água-óleo em estado estacionário foram realizados a diferentes fluxos fracionários de água, monitorando a dinâmica da queda de pressão e visualizando o deslocamento de fluidos na escala de poros. A aquisição de imagens em tempo real por microscopia de fluorescência permitiu examinar a evolução da saturação das fases. A comparação direta entre as curvas de permeabilidade relativa dos meios porosos vugulares com aquela da matriz porosa mostrou que a incorporação de *vugs* leva a (i) maior permeabilidade absoluta equivalente, especialmente com cavidades mais longas e em maior número, (ii) aumento da ocupação de óleo na matriz porosa, devido à invasão de água menos eficiente, e (iii) maior permeabilidade relativa à água, que flui preferencialmente pelo espaço vugular. Esses resultados são consistentes com a natureza molhável ao óleo dos micromodelos, uma vez que os *vugs* oferecem menor resistência capilar ao fluxo da fase não molhante. Nossa abordagem microfluídica de baixo custo provavelmente nos permitirá estudar sistematicamente configurações mais complexas de meios porosos heterogêneos.

Palavras-chave

Meios porosos vugulares; Micromodelos de PDMS-vidro; Escoamento de duas fases; Permeabilidade relativa; Microfluídica;

Table of contents

1	Introduction	14
1.1	Problem statement	14
1.2	Motivation	15
2	Theoretical Framework	17
2.1	Naturally occurring porous media	17
2.2	Intrinsic properties of porous media	17
2.3	Other properties: Surface wettability and capillary pressure	19
2.4	Capillary and viscous effects on two-phase flow	20
2.5	Relative permeability	22
2.6	Relative permeability measurement	24
2.6.1	Unsteady state methods	24
2.6.2	Steady-state methods	25
2.7	Waterflooding processes in porous media	26
2.8	Heterogeneous porous media	28
3	State of the art and dissertation goals	30
3.1	Pore space topology and single-phase flow in vugular porous media	30
3.2	Numerical modeling of single-phase flow in vugular porous media	31
3.3	Simplified modeling approaches of vugular porous media	32
3.4	Two-phase flow in vugular porous media	33
3.5	Flow regimes of multi-phase flow in porous media	36
3.6	Research gaps	37
3.7	Dissertation goals	38
4	Materials and methods	39
4.1	General description of experiments	39
4.2	Fluids and their properties	43
4.3	PDMS/glass porous media micromodels	44
4.3.1	Porous media design	44
4.3.2	Mold fabrication	46
4.3.3	PDMS stamps and micromodel sealing	46
4.3.4	Pressure measurement holes	48
4.4	Geometric characterization of micromodels	48
4.5	Surface wettability characterization	50
4.6	Experimental procedure	51
4.6.1	Single-phase flow Experiments	51
4.6.2	Two-phase flow Experiments: Relative Permeability Measurement	51
4.6.3	Two-phase flow Experiments: Oil displacement by water injection	52
4.7	Image acquisition	53
4.8	Image processing	53
5	Results and discussions	56
5.1	Characterization of the PDMS-glass porous media micromodels	56

5.1.1	Dimensions and pore space features	56
5.1.2	Hydraulic Properties: Absolute Permeability of the porous matrix	59
5.1.3	Equivalent Absolute Permeability of the vugular micromodels	59
5.2	Temporal behavior of pressure drop and fluid saturation during steady-state two-phase flow in the porous media micromodels	61
5.3	Accounting for oil saturation in the porous media micromodels	66
5.4	Accounting for water saturation in the porous matrix and vug domains of porous media micromodels	70
5.5	Morphological details of the oleic phase distribution in the porous matrix of micromodels with and without vugs	76
5.6	Sensitivity of two-phase flow pressure drop to the inclusion of vugs in the porous media micromodels	77
5.7	Sensitivity of steady-state relative permeability to the inclusion of vugs in the porous media micromodels	81
5.8	Evaluation of oil displacement by water injection in the porous media micromodels with and without vugs	85
6	Conclusions	89
	Bibliography	92

List of figures

Figure 2.1	Contact angle: Schematic depicting the water-oil-solid matrix interface in a porous medium.	19
Figure 2.2	Flow Pattern Diagram for immiscible displacement in porous media.	21
Figure 2.3	Curves of relative permeability to water ($K_{r,w}$) and to oil ($K_{r,o}$) in homogeneous porous media.	23
Figure 2.4	Schematic of oil displacement by waterflooding.	27
Figure 2.5	Vuggy rock domains.	29
Figure 4.1	Simplified diagram of the micromodel-flooding set-up.	39
Figure 4.2	Photograph of the micromodel-flooding set-up.	40
Figure 4.3	Injection system details.	42
Figure 4.4	Experimental setup on the microscope motorized stage.	42
Figure 4.5	General design of the 2D porous media micromodels.	45
Figure 4.6	Vugular porous media micromodels.	45
Figure 4.7	Transfer sequence of the porous matrix and T_2 vugular porous media designs from the photomasks to the final devices.	47
Figure 4.8	Details of the inlet/outlet flow lines and pressure measurement points in the PDMS/glass micromodel.	48
Figure 4.9	Confocal microscopy-based method to determine average height of the PDMS/glass porous media micromodels.	49
Figure 4.10	Contact angle measurement scheme for a sessile drop of aqueous phase on PDMS and glass surfaces in an oleic phase atmosphere.	50
Figure 4.11	Individual tile of the porous media occupied by the oleic and aqueous phases.	54
Figure 4.12	Illustration of the segmentation step in image processing.	54
Figure 5.1	Porous matrix micromodel saturated with the oleic phase.	57
Figure 5.2	Vugular porous media micromodels saturated with the oleic phase	57
Figure 5.3	Size distribution of straight and constricted channels of the porous media micromodels.	58
Figure 5.4	Calculation of absolute permeability (K_{abs}) in the porous matrix micromodel.	59
Figure 5.5	Calculation of absolute (K_{abs}) and equivalent permeability (K_{eq}) in the porous media micromodels with and without vugs.	60
Figure 5.6	Pressure drop (ΔP) and water saturation (S_w) in the porous matrix micromodel after 30 minutes of simultaneous flow of water and oil at 2 ml/h and $f_w = 0.5$.	61
Figure 5.7	Pore-scale visualization of the oleic and aqueous phases when simultaneously flowing at steady state through the porous matrix micromodel ($f_w = 0.5$).	62

Figure 5.8	Transition of the pressure drop (ΔP) and water saturation (S_w) in the porous matrix micromodel when the fractional flow of water is changed from 0.9 to 1, at total flow rate of 2 ml/h.	64
Figure 5.9	Pore-scale visualization of the oleic and aqueous phases when simultaneously flowing through the porous matrix micromodel at $f_w = 0.9$ and 1.	65
Figure 5.10	Pressure drop (ΔP) and water saturation (S_w) in the porous matrix micromodel after 60 minutes of flow of water at 2 ml/h ($f_w = 1$).	65
Figure 5.11	Pore-scale visualization of the oleic and aqueous phases in the porous matrix micromodel after 60 minutes of flow of water at 2 ml/h ($f_w = 1$).	66
Figure 5.12	Oil saturation (S_o) in the porous matrix micromodel and in the whole porous medium of T_1 to T_3 vugular micromodels as a function of the fractional flow of water (f).	67
Figure 5.13	Pore-scale visualization of the aqueous and oleic phases when simultaneously flowing ($f_w = 0.3$) at steady state through the porous media micromodels with and without vugs.	68
Figure 5.14	Oil saturation (S_o) in the porous matrix micromodel and in the porous matrix domain of T_1 to T_3 vugular micromodels as a function of the fractional flow of water (f).	69
Figure 5.15	Oil saturation in the porous matrix versus oil saturation in the whole porous medium of micromodels.	70
Figure 5.16	Vug-scale visualization of the aqueous and oleic phases when simultaneously flowing ($f_w = 0.3, 0.8$ and 1) at steady state through the porous media micromodels with and without vugs.	71
Figure 5.17	Vug-scale visualization of the aqueous and oleic phases when simultaneously flowing ($f_w = 0.3, 0.8$ and 1) at steady state through the porous media micromodels with and without vugs.	72
Figure 5.18	Vug-scale visualization of the aqueous and oleic phases when simultaneously flowing ($f_w = 0.3, 0.8$ and 1) at steady state through the porous media micromodels with and without vugs.	73
Figure 5.19	Water saturation in the vug domain versus water saturation in the porous matrix domain of vugular micromodels.	75
Figure 5.20	Distribution of the oleic phase in the porous matrix without vugs and in the porous matrix of the vugular media T_2 as a function of the oil unit size.	77
Figure 5.21	Steady-state pressure drop during the flow of water and oil in the porous media micromodels as a function of the water saturation in the whole porous medium.	78
Figure 5.22	Transition of the pressure drop across the porous media micromodels when the fractional flow of water is changed from 0.9 to 1.	80

Figure 5.23 Relative permeability to the aqueous ($K_{r,w}$) and to the oleic ($K_{r,o}$) phases in the porous matrix without vugs and in the vugular porous media micromodels as a function of water saturation (S_w).	81
Figure 5.24 Relative permeability to the aqueous phase ($K_{r,w}$) as a function of the relative permeability to the oleic phase ($K_{r,o}$) in the porous matrix without vugs and in the vugular porous media micromodels.	83
Figure 5.25 Remaining oil saturation in the porous media micromodels after water injection up to water breakthrough and steady state.	86
Figure 5.26 Steady-state water/oil distributions in the porous media micromodels with and without vugs after water injection in the oil displacement experiments.	87

List of tables

- Table 4.1 Viscosity (μ) and interfacial tension (γ_{wo}) measured at 22° C for fluids of system 1 and system 2. 43
- Table 5.1 Characteristics of the *water relative permeability endpoints* in the porous media micromodels. $S_{o,1}$ is the remaining oil saturation in the whole porous medium, $S_{o,2}$ is the remaining oil saturation in the porous matrix domain, $K_{eff,w}$ is the effective permeability to water, and $K_{r,w}$ is the relative permeability to water. 84

“Science is not a set of facts but a way of giving order, and therefore of giving unity and intelligibility, to the facts of nature.”

Jacob Bronowski, *The Educated man in 1984*.

1 Introduction

1.1 Problem statement

Naturally fractured-vuggy carbonate reservoirs have tremendous potential as suppliers of oil and gas, holding approximately 50% of the world's hydrocarbon reserves [1, 2, 3]. In the Brazilian scenario, the giant pre-salt fields located in deep waters off the coast of the Espírito Santo and Santa Catarina states have been widely characterized as fractured-vuggy carbonate formations [4, 5]. Carbonate oil reservoirs, in practical comparison with sandstone reservoirs, have lower oil recovery factors and, in terms of estimation of accurate and reliable petrophysical properties, fluid flow mobilization phenomena are still not fully understood. One of the biggest challenges in this type of formation is its heterogeneous nature [6, 7]. The rock matrix, in addition to the fractures, is characterized by the superposition of several families of pores and fluid conduits at different scales and distributions, result of various dissolution processes including geochemical reactions and sedimentation around fossils [8, 9, 10].

A simplified view of the multiscale heterogeneities in carbonates allows to conceptualize them as a system formed by (i) a homogeneous matrix of intergranular pores, (ii) a system of macropores or vugs that are some orders of magnitude larger than the intergranular pores, and (iii) the system of fractures [2, 3, 11]. In that sense, a vugular porous medium is made up of a porous matrix with vugs scattered throughout its body, and depending on whether they are connected to each other, they can be defined as separate-vug pores or touching-vug pores [6, 8]. The presence of these free-flow cavities has a high impact on the physics of fluid flow through the porous matrix and brings the need to evaluate equivalent petrophysical properties for the vugular porous media [2, 12, 13, 14, 15].

1.2

Motivation

Two-phase flow in porous media is complex and is usually described by Darcy's law using relative permeability curves, which reflect the ability of a porous medium to let fluids pass through them. It depends directly on the structure of the intergranular and vugular porous space and on the local saturation of fluids [2, 14, 16]. Traditionally, permeability is determined using laboratory-based measurements on plug samples from well cores. However, for vugular porous media, due to the large scale and complexity of the heterogeneities, obtaining representative and reliable samples is difficult [7, 17].

Vugs can have a wide variety of geometries and be multi-spatial distributed [18]. Therefore, comparing and scaling samples may be a challenging task. It has been extensively demonstrated that conventional methods of interpreting experimental data, valid for intergranular porosity media, are inadequate in heterogeneous vugular reservoirs [13, 19]. High anisotropy, locally dependent properties, absolute equivalent permeabilities that may vary by orders of magnitude, and anomalous shapes in relative permeability curves have been documented from core-flooding experiments in carbonate rocks [2, 12, 15, 20, 21].

In recent years, the wide versatility and control over digital rock models have helped to describe and model fluid flow processes in vuggy reservoirs, particularly in relation to the effect of vugular space structure on single-phase flow characteristics [17, 22, 23, 24]. This approach involves scanning rock samples for pore space topology information or developing conceptual models, formulating equations to describe fluid flow in both the porous matrix and vugular space, and solving these equations to obtain equivalent properties [10, 25]. Nevertheless, experimental data continues to be necessary for the validation of many of these models and for a better understanding of the fluid mobilization and transport processes in more complex systems, such as those that involve multi-phase flow.

Understanding the physics of multiphase flow in porous media requires not only measurement of macroscopic properties but also observations within the porous media, at the pore scale [9, 26]. Microscopic phase distribution, pore occupancy mechanisms and flow patterns are some examples of these valuable and limited observations. Furthermore, in vuggy formations, the role of vugs as free-flow and fluid storage regions, and the interactions of the vugs with the porous matrix and other neighboring vugs are information of particular interest. It may determine the sweep efficiency, for example, in oil displacement operations by waterflooding [9, 14, 27].

The only direct method for obtaining insights into fluid flows originating from natural heterogeneities of a specific reservoir may be fluid flow analysis for core-plug samples [28]. However, the opacity of the rock makes it impossible to use direct visualization techniques to monitor pore-scale fluid flow in simple core-flooding experiments. Sophisticated imaging techniques such as X-ray computed tomography (CT) have become quite popular for acquiring 3D porosity distributions in heterogeneous media [25, 26, 29]. Nevertheless, the process of collecting high-resolution images under fluid flow conditions may be expensive and time-consuming. In some circumstances, the only information that can be accessed is the overall fluid saturation in sections of the core [13, 14, 20].

An intermediate point between a digital rock model and a core-plug sample is visualization of rock analogs by microfluidic approaches using porous media micromodels. These are devices with a 2D or 3D connected porous network, which are used to investigate and visualize small-scale fluid flow dynamics [30, 31]. A powerful tool of porous media micromodelling is the ability to control pore structure parameters such as pore shape, size, connectivity, and distribution [32]. Moreover, microfluidic experiments not only give a qualitative description of fluid displacement at the pore scale but also, when coupled to a pressure drop and flow rate measurement system, allow these process variables to be correlated to the nature and structure of the porous medium.

This work aims to collect information on how the flow of water and oil through a microfluidic porous medium is affected by the presence of vugs designed with different configurations. Reliable measurements of pressure drop and fluid saturations are correlated with fluid flow phenomena observed at the pore scale and macroscopic fluid distributions in the entire porous medium, allowing us to perform relative permeability calculations. It is contemplated that the collected information may be useful for the validation of numerical simulations of two-phase flow in vugular porous media.

2

Theoretical Framework

This chapter presents the conceptual background of this thesis. First, porous media and their intrinsic properties are defined. Then, some variables that affect two-phase flow in porous media, such as capillarity, surface wettability and viscosity ratio, are addressed. In addition, relative permeability is formally defined and experimental measurement techniques are explained. Finally, a brief review on oil displacement by water injection, and some characteristics of heterogeneous porous media, especially vugular media, are discussed.

2.1

Naturally occurring porous media

In the context of this research, naturally occurring porous media refer to rocks from underground formations that contain hydrocarbon reserves. Part of the domain of these rocks is occupied by a persistent solid phase, called *solid matrix*. The remaining part, referred to as *pore space*, is occupied either by a single fluid phase, or by several fluid phases, e.g., gas, water, and oil. In order to enable the flow and transport of fluids across the porous media, the configuration of the pore space must meet specific criteria regarding the concept of connectivity. At least some of the pores comprising the void space should be interconnected [33].

2.2

Intrinsic properties of porous media

Two approaches can be established to characterize a porous medium. At the microscopic level, also called *pore scale*, the structure is expressed in terms of a statistical description of the pore-size distribution, degree of interconnection and orientation of the pores, and fraction of unconnected pores. At the macroscopic level, instead, bulk parameters, which have been averaged over scales much larger than the pore size, are generally used. Depending on the goal of the study, both approaches are useful and complementary [34].

The macroscopic description of single-phase flow in porous media is commonly addressed in terms of porosity, specific surface area, and absolute

permeability. All these parameters are influenced, to a greater or lesser degree, by the pore structure [35]. Porosity and permeability are typically measured on a laboratory scale using experimental core-flooding systems.

The *effective porosity* (ϕ) of a sample of porous media is defined as the ratio of interconnected pore volume V_p to the total volume V_t of the sample. V_t includes solid as well as non-solid space [36]. Rigby et al. [37] note that porosity can be assessed through volumetric measurements of core samples, such as petrographic image analysis (PIA), mercury injection methods, fluid re-saturation method, or often geological logs. More sophisticated and expensive techniques include X-ray tomography and scanning electron microscopy.

The ratio of the internal solid surface area A_s to the total volume V_t is called *specific surface area* (s) [36]. When a single fluid phase moves through a porous medium, flow resistance is associated to surface forces between the solid and the fluid. These forces are proportional to the surface area and may prevent the flow regardless of high porosity [38].

In macroscopic terms, both the topology and geometry of the porous space will determine the resistance to flow and therefore how permeable the porous medium is. Darcy's law, an empirical equation describing laminar flow of incompressible fluids (Eq. 2-1), is largely used for calculation of fluid flow in porous media.

$$v = K_{abs} \frac{1}{\mu} \frac{\Delta P}{L} \quad (2-1)$$

As described by Honarpour and Mahmood [39] and Ahmed et al. [40], this law relates the flow rate per unit area v of a fluid of known viscosity μ to the pressure gradient across the porous medium $\frac{\Delta P}{L}$. The proportionality factor is called *absolute permeability* (K_{abs}) and measures the ability of porous materials to conduct flow.

It is important to note that absolute permeability is an intrinsic rock property and is measured when the porous medium is 100% saturated with a single fluid phase, which can be liquid or gaseous [40]. Dullien [35] remarks that measurement at a single steady-state flow velocity may permit calculation of permeability from Darcy's law. However, it is recommended and conventional to perform measurements at various low flow velocities, i.e., in the creeping regime, plot the steady-state values against the pressure drop, and fit a straight line to the data. The flow region in which Darcy's law holds linearly is called *Darcy's region of linearity*.

2.3

Other properties: Surface wettability and capillary pressure

When two or more fluid phases are present in a porous medium, different phenomena associated with both fluid-fluid and fluid-solid wall interactions become important. These interactions determine the contact angle of each phase with the solid wall and the interfacial tension between the fluid phases [41].

Figure 2.1 shows a diagram of the equilibrium of forces acting at the oil-water-solid interface in a porous medium. There, γ_{ow} is the oil-water interfacial tension, and γ_{ws} and γ_{os} are the oil and water superficial tensions, respectively [16]. The angle formed between the fluids is named *contact angle* (θ), and it is defined by the so-called Young's equation $\gamma_{os} = \gamma_{ws} + \gamma_{ow} \cos \theta$. By means of this property, the wettability-based behavior of fluid-fluid displacement processes in porous media can be described.

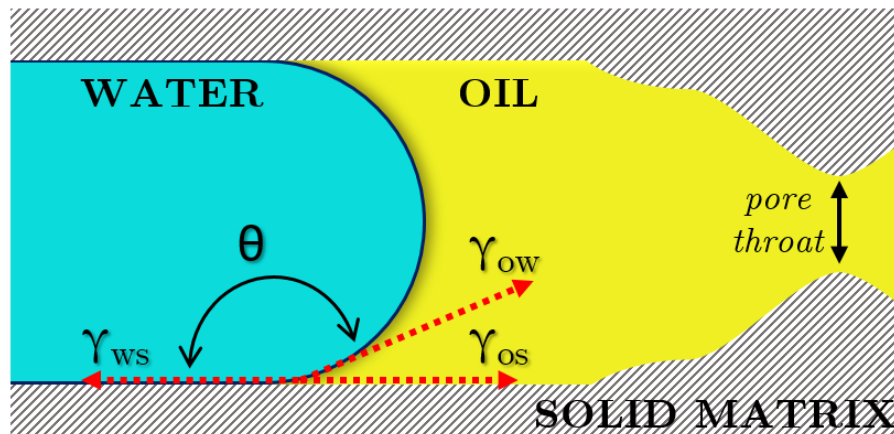


Figure 2.1: Schematic depicting the water-oil-solid matrix interface in a porous medium. The contact angle is determined from the equilibrium of forces between the horizontal projection of the oil-water interfacial tension along the solid surface ($\gamma_{ow} \cos \theta$) and the surface tension of oil (γ_{os}) and water (γ_{ws}), respectively.

Depending on the physicochemical nature of the fluids and the solid, one of the fluids, referred to as the wetting phase, will tend to adhere to the solid ($\theta < 90^\circ$), while the other, referred to as the non-wetting phase, will be farther from the solid surface ($\theta > 90^\circ$). This means that the wetting phase preferentially covers the microscopic solid surface of the porous matrix [42].

Reservoir rocks are typically water-wet from their origin, as rock particles tend to be solely in contact with brine. However, as crude oil migrates into a reservoir from source rock, heavier components of oil adsorb to the rock surface over time. The latter causes reservoir rocks to become less water-wet as they age. Unlike sandstone reservoirs, carbonate rocks are characterized

as neutral-wet or preferentially oil-wet. In this type of reservoir, oil tends to strongly adhere to the rock surface, which inhibits oil recovery by injection of a non-wetting phase, for example, by waterflooding [43, 44, 45].

In processes involving the flow of two immiscible fluid phases, the pressure difference between the two sides of the interface at any point of the porous medium is given by the capillary pressure (P_c). This variable is quantified by Laplace's equation $P_c = 2\gamma_{ow}\cos\theta/r$, where r is the radius of the pore throat and θ is the contact angle of the displacing fluid [42]. In general, a porous medium contain pores with different dimensions and shapes. Pores with larger throats exhibit low P_c , while those with narrow entry channels, supporting interfaces of smaller radius of curvature, exhibit higher P_c . The effect of this additional pressure as a driving or resistance force to pore invasion explains the difference in the dynamics of imbibition (displacement of the non-wetting phase with a favorable P_c) and draining (displacement of the wetting phase with an unfavorable P_c) that is observed in porous media.

2.4

Capillary and viscous effects on two-phase flow

As previously mentioned, capillary effects come into play from capillary pressure originating from the microscopic curvature between water and oil at the pore scale. When a macroscopic pressure gradient is applied through a porous medium, it results in a viscous flow that disturbs the capillary equilibrium. Viscous forces can either stabilize or destabilize the interface, depending on whether the displacing fluid is more viscous or not. Fluid-fluid interfacial tension, surface wettability, and flow velocity are also first-order variables that impact interface stability [46, 47]. At steady-state conditions, the distribution of fluids in the porous medium is a response to the compromise between capillary and viscous effects that occurs during the fluid-fluid displacement.

The flow behavior of a fluid phase invading a porous medium initially saturated with another immiscible fluid can be characterized by two dimensionless numbers: the capillary number $Ca = \mu_2 v_2 / \gamma$, which is the ratio of viscous to capillary forces, and the viscosity ratio $M = \mu_2 / \mu_1$, which is the ratio between the viscosity of the fluids. Here, μ and v are respectively the viscosity and Darcy velocity, and the subscripts 1 and 2 refer to the displaced and displacing fluids, respectively.

Depending upon the capillary number and the viscosity ratio, fluid flow can occur in three different flow regimes: stable displacement, capillary fingering, and viscous fingering. Figure 2.2 outlines this classification proposed by Lenormand et al. [48].

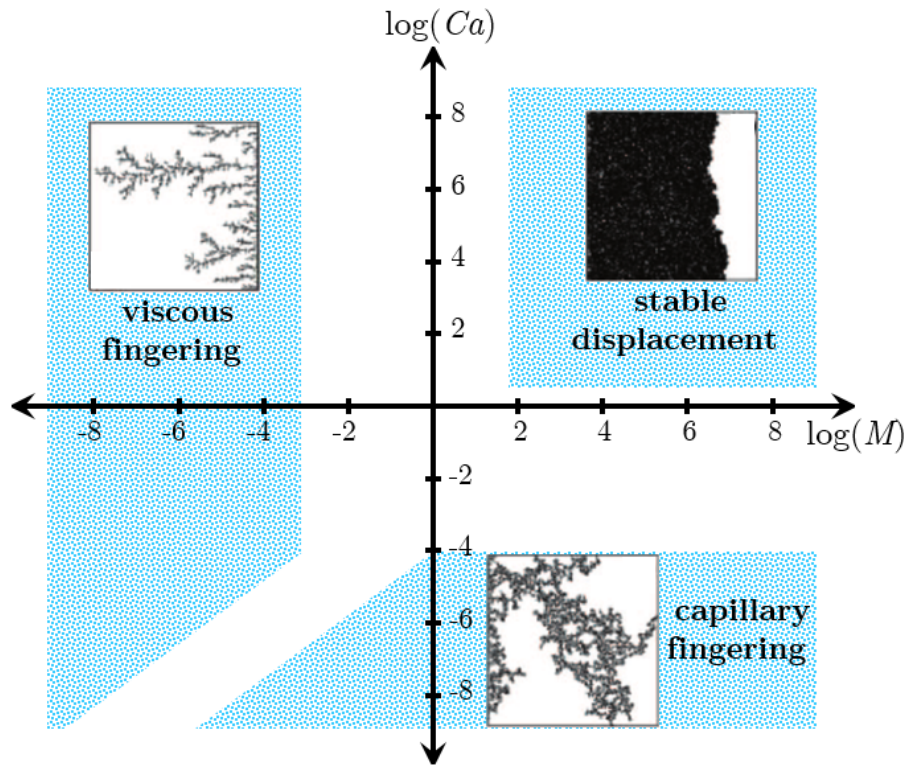


Figure 2.2: Flow Pattern Diagram for immiscible displacement in porous media proposed by Lenormand et al. [48]. Adapted from Niasar and Hassanizadeh [49].

When a more viscous fluid displaces a less viscous fluid ($M > 1$), the pressure drop in the front is associated with the invading phase, leading to (i) stable displacement or (ii) growth of capillary fingering. At high Ca , the displacement is stabilized by viscous effects and the displacement front is approximately flat. The sweep efficiency is very high and the volume of trapped phase behind the displacement front is small. At low Ca , instead, viscous forces are negligible in both fluids and the principal force is due to capillarity. Capillary fingers spread across the porous media and grow in all directions, even backward. Therefore, the displacement front is non-uniform and a large amount of fluid is left behind.

At unfavorable viscosity ratios ($M < 1$), the pressure drop is associated with the displaced phase, and the displacement front is non-uniform. At high Ca , capillary effects are negligible and the growth of viscous fingers governs the invasion of the porous medium. They exhibit tree-like behavior and spread across the porous space, working their way towards the exit. In contrast, at low Ca , fluid movement is controlled by capillary forces leading to the capillary fingering regime described above. In the transition zones between the regimes, both viscous pressure drops of both fluids and capillary forces can play an important role [48, 49].

2.5

Relative permeability

In Section 2.2, *absolute permeability* was defined as an intrinsic property of a porous medium when it is 100% saturated with a single fluid phase. Generally, the flow of fluids in oil reservoirs involves more than one fluid, so the ability of each fluid to flow is reduced by the presence of the other fluids [39]. In that instance, it is more convenient to measure the permeability in reference to each fluid present in the porous medium. Such permeability is the *effective permeability* ($K_{eff,i}$) of the medium to a particular flowing fluid i .

The ratio of effective permeability to absolute permeability is called *relative permeability* ($K_{r,i}$) (Eq. 2-2). In this work, the relative permeability to water and to oil is referred to as $K_{r,w}$ and $K_{r,o}$, respectively; while the effective permeabilities are represented by $K_{eff,w}$ and $K_{eff,o}$ [16, 40]. Darcy's law (Eq. 2-1) has also been used to describe the flow of two immiscible fluid phases in porous media. The extended equation (Eq. 2-3) relates the macroscopic velocity of each fluid to the total pressure gradient by means of the effective permeability [39].

$$K_{r,i} = \frac{K_{eff,i}}{K_{abs}}, \quad (2-2)$$

$$v_i = K_{eff,i} \frac{1}{\mu_i} \frac{\Delta P}{L}, \quad (2-3)$$

The concept of relative permeability provides a very useful dimensionless scale for effective permeability. $K_{r,i}$ values normally range from zero to one regardless of the absolute permeability value [16]. The relative permeability has a first-order dependence on the saturation level in the porous media [39]. When a fluid occupies only a part of the porous space, the geometric characteristics become functions of the fluid saturation, for example, the porosity is replaced by the volumetric fraction of the pore space occupied by the fluid [42]. Figure 2.3 shows a typical curve of relative permeability to water and to oil in homogeneous porous media as a function of water saturation.

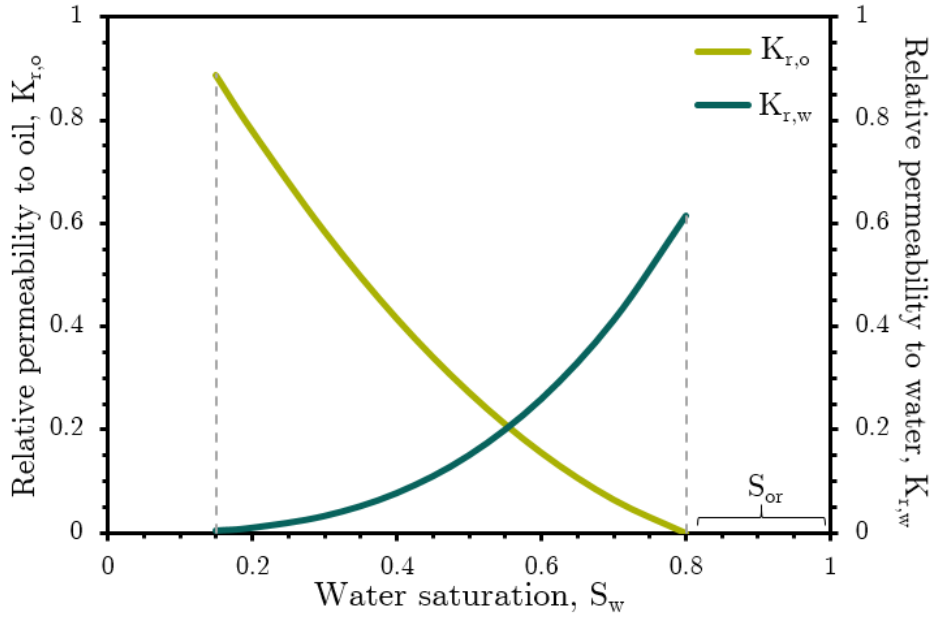


Figure 2.3: Curves of relative permeability to water ($K_{r,w}$) and to oil ($K_{r,o}$) in homogeneous porous media [39]. At the endpoint, when oil no longer flows, $K_{r,o} = 0$ and $K_{r,w}$ exhibits a maximum value.

Lenormand and Lenormand [50] explain the physics of water-oil displacement in porous media from the relative permeability curves. If an oil-wet porous medium is drained, $K_{r,o}$ rapidly decreases as larger pores are invaded first and the flow of oil occurs through smaller pores. Then, as water saturation increases, $K_{r,w}$ goes up rapidly because water becomes the continuous phase. When oil saturation reaches the residual oil saturation, S_{or} , the remaining oil in the porous medium is present as domains around grain contact points and, in the most drained regions, as very thin films covering the solid surface of grains. Oil constitutes a discontinuous and immobile phase that cannot transmit pressure. Consequently, $K_{r,o} = 0$ and $K_{r,w}$ exhibits a maximum value.

It is interesting to note that, depending on the direction of saturation changes, different fluid distributions are possible for each saturation level. Therefore, the relative permeability values obtained for drainage (reduced saturation of the wetting phase) may be different from those for imbibition (increased saturation of the wetting phase) [39]. This phenomenon is called hysteresis.

An additional variable that influences relative permeability is the surface wettability of the porous medium. In general, at a given saturation, the relative permeability to a fluid is greater when it is the non-wetting phase. For example, the relative permeability to water increases and the relative permeability to oil decreases as the system becomes more oil-wet. This has been justified because the wetting phase tends to travel through the smaller

and less permeable pores, while the non-wetting phase travels more easily in the larger pores. Furthermore, when the non-wetting phase begins to be trapped as discontinuous ganglia in the larger pores, these fluid units block the pore throats, reducing the relative permeability to the wetting phase [51].

2.6

Relative permeability measurement

Relative permeability can be measured experimentally either by steady- or unsteady-state laboratory-based methods on core plug samples. In the steady-state methods, oil and water are injected at constant flow rates into the core until saturations reach equilibrium values [51]. For each imposed fractional flow rate, the pressure drop is measured and the fluid saturation is determined by mass balance. The relative permeability is evaluated at each saturation using Darcy's law. On the other hand, in the unsteady-state methods, fluids are not injected simultaneously into the core. Instead, the test involves the displacement of one fluid by injecting the other fluid at a constant flow rate (or constant pressure) [52]. Additional details of both methods are provided below.

2.6.1

Unsteady state methods

Unsteady state methods are popular because a complete set of relative permeability curves can be obtained in a few hours [39]. In general, a fully water-saturated core is first flooded with oil and driven to irreducible water saturation. After that, water is injected into the core at a constant flow rate, and the relative permeability is calculated during the waterflooding operation [51]. Since steady-state is not reached in the porous medium, Darcy's Law does not apply. The experimental data (oil production and inlet pressure) are analyzed and the relative permeability curves are obtained by solving an inverse problem. The Buckley-Leverett equation for linear displacement of immiscible fluids is the basis for all calculations [39, 52].

Despite the fewer instrumentation requirements in this method, many difficulties are inherent in the non-steady state condition. At each fluid saturation level, properties are continually changing, which makes it challenging to properly monitor and account for, and leads to repeatability problems. In addition, the time between the front breakthrough and complete flood out is usually small, introducing computational obstacles. The interpretation techniques involved also have many uncertainties due to gross simplifying assumptions. It

is advisable that relative permeability values obtained from this method be considered only qualitative [39, 51].

2.6.2

Steady-state methods

Steady-state methods for determining permeabilities have the widest application and greatest reliability because capillary phenomena prevail, saturations are measured directly, and the calculation scheme is based on Darcy's law [39]. In general, the two fluid phases are simultaneously injected into the core sample at a constant total flow rate. Once the measured pressure drop across the core remains constant, the system is assumed to be at steady-state. The pressure drop is then measured and used to calculate the effective permeability of each fluid from extended Darcy's Law (Eq. 2-3) [52].

Depending on the previously established injection flow ratio, a specific fluid saturation is reached inside the porous medium. That way, by changing the flow ratio and repeating the pressure measurement as the new steady-state is reached, relative permeability can be calculated over a wide range of saturation levels. During the test, changes are controlled to be unidirectional to avoid hysteresis. At the endpoint, only water is injected into the core until irreducible oil saturation is accomplished. [39, 52].

A disadvantage of steady-state methods is the time required to reach fluid equilibrium at the pore scale, which may take several hours or even days after each change in the injection flow ratio. This could make these methods uneconomical in some cases [52]. In addition, measurement of fluid saturation in the porous medium has to be performed. The reliability of relative permeability curves will depend greatly on the accuracy of this determination. Accuracies of at least 2% are often desirable [39]. There are two approaches to saturation measurement: external and in situ techniques.

The most common *external technique* is based on mass balance. During the test, the cumulative injection and production volumes are measured and the difference is assumed to be retained in the porous media. It provides just an average value of fluid saturation and does not reveal the saturation profile. As expected, significant errors may be introduced when the pore volume of the core is small or the dead volume in the set-up is representative [39, 52].

On the other hand, *in-situ techniques* allow one to measure the amount of fluid inside the core from the response resulting after the application of some type of known stimulus. This response is associated with saturation levels by means of a calibration curve initially constructed, which compares the response of a completely dry and completely saturated core. X-ray absorption

and electrical resistivity are commonly used. These techniques offer higher precision and reliability than external techniques and are capable of measuring point saturations, rather than just average values [39].

Multidimensional scanning techniques, such as micro-computed tomography (μ CT) and nuclear magnetic resonance, have become popular for saturation profiling in sections of rock samples [25, 26, 39, 53, 54]. The application of these techniques aims to obtain additional information about the distribution of fluids throughout the porous media, and thus improve the understanding of the fluid displacement processes described by relative permeability curves.

2.7

Waterflooding processes in porous media

Oil displacement by water injection is the oldest and cheapest method for secondary recovery available nowadays [16]. On average, global recovery factors after primary and secondary oil recovery operations may reach approximately one-third of what was originally present in the reservoir [55].

In this operation, the displacement of oil is driven by the advance of a waterfront across the porous medium. As sketched in Figure 2.4, an applied pressure gradient (ΔP) favors water invasion into the pore space and, consequently, oil production by sweeping out oil-saturated regions. However, when water breaks through, the resistance to water flow is lower and oil recovery becomes considerably less efficient. At least one preferential flow pathway has been created, connecting the inlet and outlet of the porous medium and leaving behind a large amount of oil.

During the waterflooding, the transmission capacity of water and oil across the porous medium follows the trends described by the relative permeability curves. In that sense, characteristics of the waterflooding can be predicted from them. For example, earlier water breakthrough and less efficient oil production due to increases in the water/oil relative permeability ratio [51].

The macroscopic behavior observed in waterflooding operations comes as a consequence of the fluid displacement phenomena that occur at the pore scale. Surface wettability, capillary number, viscosity ratio and structure of the porous medium are major factors controlling the characteristics of the displacement front. Typical conditions in oil recovery operations by waterflooding involve unfavorable viscosity ratios ($M < 1$) and moderate capillary numbers ($Ca \approx 10^{-6}$) [46].

According to the *Flow Pattern Diagram* presented in Figure 2.2, at $M < 1$ and $Ca \approx 10^{-6}$ both viscous fingering (higher viscosity ratios) and

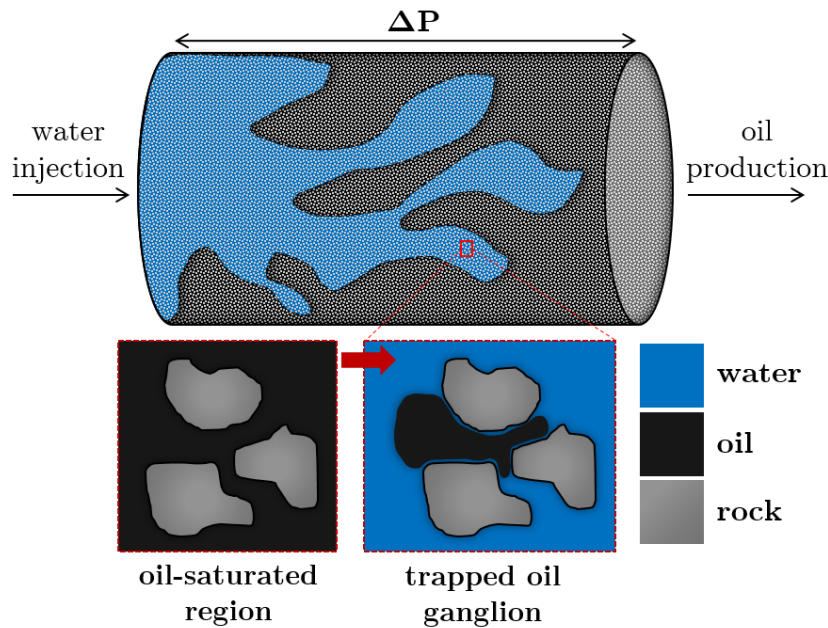


Figure 2.4: Schematic of oil displacement by waterflooding in homogeneous porous media. Preferential flow paths are created, leaving regions unswept, and even in the swept area, some ganglia are trapped by capillary pressure.

capillary fingering (lower viscosity ratios) could control the displacement of the waterfront and, therefore, the distribution of this phase throughout the porous medium. It has been reported that the viscous fingering regime tends to reduce sweep efficiency [56].

Moreover, according to the surface wettability of the rock, the pore space invasion by a wetting or non-wetting phase can be describe as a drainage or imbibition process. In an oil-wet porous medium, the invasion of pores is controlled by the capillary pressure, water must build a threshold pressure difference before it can invade a pore. On the other hand, in a water-wet porous medium, the pore invasion is favored by the capillary pressure serving as a driving force [51, 57].

In a strongly water-wet porous medium, after the water breakthrough, almost all the remaining oil is immobile due to capillary forces. As a consequence, there is little or no additional oil production. Contrastingly, in a strongly oil-wet porous medium, much of the remaining oil is still continuous through films on pore surfaces and may be produced over a long period of simultaneous oil and water production. In general, waterflooding in an oil-wet system is less efficient than in a water-wet one because more water must be injected to recover a given amount of oil [51].

As previously introduced, such a dependence on the way each fluid occupies the pore space causes flow behavior and fluid distribution to exhibit hysteresis when comparing drainage and imbibition processes [42, 58].

2.8

Heterogeneous porous media

The theoretical framework presented in this chapter concludes with some fundamentals of heterogeneities in porous media. Subsequently, in Chapter 3, the state of the art in single and two flow in vugular porous media will be addressed.

A porous medium is said to be homogeneous with respect to some property, such as porosity or permeability, when the value of that property is independent of location. Otherwise, the porous medium is said to be heterogeneous [33, 41]. In that regard, fluid flow behavior in carbonates differs significantly from that of sandstones, especially due to the extremely heterogeneous nature found in these types of formations [1]. Depending on the scale of heterogeneities, different domains may be considered. At macroscopic scale, fractures that longitudinally connect the porous medium; and, on smaller scale but sufficiently larger than the pore scale, vugs that are scattered throughout the porous matrix at different sizes and distributions [17, 59].

Bear [33] defines a *fracture* as a part of the void space in a porous medium domain that has one of its dimensions much smaller than the other two. Numerous factors, such as accumulation of locally high mechanical or thermal stresses, or even presence of zones of mechanical weakness in the rock, can naturally cause fractures in rock formations. The hydraulic properties of these fluid-carrying conduits are distinctly different from those of the porous matrix in which they are embedded. For example, fractures normally exhibit a high permeability with respect to that of the porous matrix surrounding them, so they can increase the absolute permeability of the heterogeneous porous medium by several orders of magnitude and constitute the fluid's dominant pathway [17, 22].

Very different from fractures in terms of geometry, physical appearance, and effect on flow behavior, *vugs* are three-dimensional void spaces occluded in the porous matrix. Their spectrum of scale variation is huge and may range from the mm-scale to the m-scale [6, 8]. These cavities can be formed by a wide variety of processes, including rock dissolution in carbonate formations, intrusion of acidic water, or vesicles created by accumulating and/or escaping gases during the cooling of volcanic magma [33]. The so-called vuggy carbonates are an important type of carbonate oil reservoirs whose heterogeneity is mainly due to the presence of vugs [7]. Figure 2.5 shows some examples of carbonate rock domains.

The strong anisotropy and multi-scale characteristics of vuggy carbonates limit their description as a continuum and, in practical terms, make it

difficult to obtain representative rock samples. Systems with very complex vug-fracture networks may exhibit flow regimes that require specific and different approaches. For example, triple- and multiple-porosity models have been used to describe fluid flow through vuggy reservoirs [3, 33].

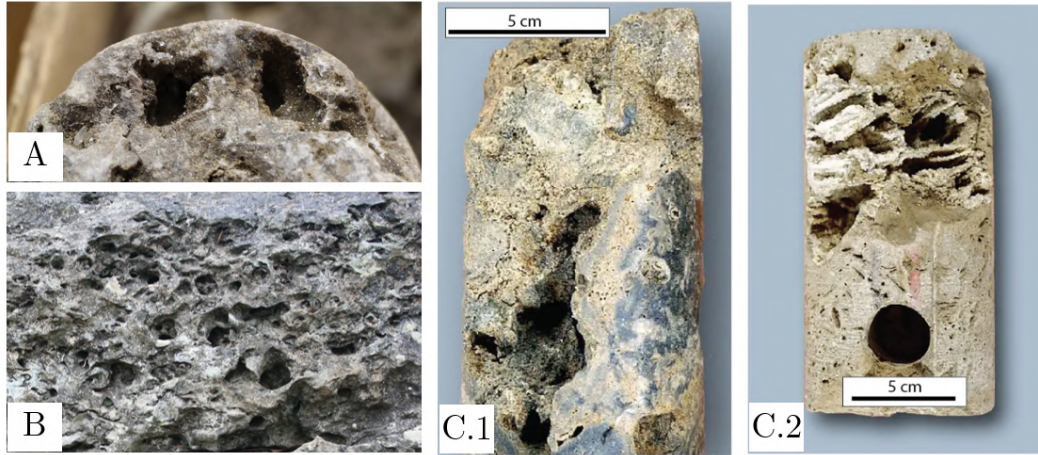


Figure 2.5: Vuggy rock domains: A and B are examples of macro-scale vuggy porosity [60]. C and D are examples of carbonate rock cores typically used in core-flooding experiments [42].

Porosity in carbonate rocks can be classified according to the model described by Lucia [6, 8]. The basis of this classification is the quantitative concept of pore-size distribution, which is intrinsically related to the rock structure and, according to the spatial distribution, controls the permeability of the rock. Three major pore-type classes are distinguished in the model: interparticles, separate-vugs, and touching-vugs.

The pore space located between grains or crystals (interparticle porosity) corresponds to porosity that can be quantified in terms of pore-size distribution or particle-size distribution (as fine as $< 20 \mu\text{m}$, as large as $> 100 \mu\text{m}$). In this work, it is referred to as *porosity of the porous matrix*. The remaining pore space is called *vuggy porosity* and, based on its origin, can be present as dissolved grains, fossil chambers, or irregular cavities in a wide variety of sizes spanning several orders of magnitude.

Depending on the vug structure, *vuggy porosity* may be further subdivided into separate-vugs and touching-vugs.

- ✘ *Separate-Vugs*: those interconnected only through interparticle pores and isolated from each other.
- ✘ *Touching-Vugs*: those that form a system of interconnected vugs either by fractures or by other fracture-like vugs.

3

State of the art and dissertation goals

This chapter presents a review of the most outstanding previous works on experimental characterization and modeling of single-phase flow in vugular porous media. Special attention is also paid to studies that have attempted to explain the behavior of two-phase flow in this type of porous media. At the end, the dissertation goals are formulated.

3.1

Pore space topology and single-phase flow in vugular porous media

The successful interpretation of macroscopic properties measured in a reservoir core sample depends on an accurate characterization of the pore space topology. Throughout the last decade, numerous studies [18, 26, 28, 61, 62, 63], have focused on proposing methods that make it possible to acquire high-quality images of the pore space and that are capable of achieving 2D and 3D representations of rock samples.

Hidajat et al. [61] related the absolute permeability of six vuggy carbonate samples to the vugular space distribution using NRM and X-ray computed tomography (CT) scanning. It was observed that in samples with very fine intergranular space and small to medium isolated vugs, the absolute permeability was low since it is the microporosity in the matrix that controls access to the vugs. When the vugs are connected through microfractures, the permeability was much higher. Samples with regions of high intergranular porosity, capable of forming an interconnected matrix-vugs flow network, were at least 400% more permeable than the other samples.

Okabe and Blunt [26] proposed a pore space reconstruction of vuggy carbonates core samples using microtomography and multiple-point statistics. In that study, the reconstructed 3D vugular space was further divided into subsets, which were individually analyzed in relation to the whole core body. Each subset preserved its own macro-porosity and macro-pore distribution. It was verified that the absolute permeability is controlled by both the small and large-scale structures, and that as the macroporosity is increased, the range of permeabilities of these subsets becomes larger due to the heterogeneous distribution of macro-pores.

Kusanagi et al. [18, 28] performed core-flooding experiments along with numerical simulations on carbonate rock samples. The 3D images revealed that only a part of the pore space effectively contributes to flow (less than 50%), while the other pores contain stagnant fluid. This behavior was consistent with the formation of preferential flow patterns due to heterogeneous porosity distributions within the rocks. Log-normal distributions with different values of geometric mean (m_ϕ), and standard deviation (σ_ϕ) were found. It was suggested that the equivalent permeability of vuggy carbonates (K_{eq}) can be predicted from these two parameters by a relationship of type $K_{eq} = \alpha(m_\phi \times \sigma_\phi^2)^\beta$, where α and β are constants. That is, the higher the geometric mean (reflecting microporosity) and the standard deviation (reflecting spatial correlation of vuggy porosity), the higher the equivalent permeability.

3.2

Numerical modeling of single-phase flow in vugular porous media

Modeling of vugular porous media is traditionally done by two different approaches: the coupled Stokes-Darcy equations and the Stokes-Brinkman equation. In the first one, the porous matrix and the free-flowing vugular space are modeled separately using the Darcy and Stokes equations, respectively. Interfacial conditions along the matrix-vug boundaries are needed in order to couple the two distinct differential equations [17, 59, 64]. Alternatively, using the Stokes-Brinkman approach, a single equation is proposed to describe the flow in both the porous matrix domain and the vugular domain. The latter does not define an explicit interface boundary condition and the equations can be reduced to Stokes equation (in vugs) or Darcy equation (in matrix) by appropriate choice of the parameters [3, 65].

Dali [25] estimated the equivalent absolute permeability of representative 2D sections of carbonate rock samples using the Stokes-Brinkman approach. CT images of the vugular space were artificially manipulated to increase the macroporosity (ϕ_m) of the original macropore distribution. By increasing ϕ_m , isolated vugs became elongated, closer together, or even connected to each other. It was observed that sections with small isolated vugs ($\phi_m < 20\%$), at most, doubled the permeability of the porous matrix. On the other hand, the presence of connected elongated vugs increased the equivalent permeability between 1 and 2 orders of magnitude, with a stronger effect in a low-permeability porous matrix. Consistent with the observations of Okabe and Blunt [26], this study showed also that when comparing different samples with $\phi_m > 20\%$, macroporosity seems not to be the only relevant parameter influencing the equivalent permeability. Other structural parameters associated

with the geometry of vugs and their spacial distribution may have strong effect on the permeability value.

In that regard, Cruz [29] studied the effect of some geometric parameters of vugs by means of Digital Image Analysis (DIA) of carbonate rock cores and solution of the Stokes-Brinkman model for single-phase flow. From the equivalent absolute permeability of different vuggy porosity arrangements, curve fitting showed that this property could be predicted with good precision by a function of type $K_{eq} = K_m + \alpha \cdot \phi_m^{-a} \cdot A^b \cdot L_w^c$, where K_m is the absolute permeability of the porous matrix, A is the surface area of vugs, L_w is the length of vugs in the main direction of flow, and α , a , b and c are fitting parameters. It was observed that the relative position of vugs is not a significant parameter in the samples studied, possibly due to the natural dispersion pattern of the macropores in them. However, it was suggested that this could be a more relevant parameter in more homogeneous rocks with macropore agglomeration. The proposed function considers vug tendency to create free flow pathways by the L_w parameter, while the A parameter distinguishes the structure of macropores between condensed and scattered in regions with similar macroporosity.

3.3

Simplified modeling approaches of vugular porous media

Simplified modeling approaches consider vugs with simple artificial geometries, such as circles and ellipses, embedded in a porous matrix of certain permeability. These approaches are less computationally expensive and allow one to isolate and identify effects that in more complex multi-scale distributions may become less apparent. Most of them solve steady-state single-phase flow based on the Stokes-Brinkman equation in a wide variety of vug geometries and distributions.

Arbogast et al. [22] and Golfier et al. [65] proposed a 2D model with layered vugs embedded in a porous matrix of homogeneous permeability. In this model, vugs can completely connect the porous media according to its continuity through additional meandering or constrained cavities. Arbogast et al. [22] found that the equivalent permeability is moderately sensitive to vug channel shape, very sensitive to vug apertures, and extremely sensitive to the connectivity structure. As has been shown in more realistic models of porous media, vug connectivity is a critical consideration in predicting fluid flow characteristics. Golfier et al. [65] showed that increases in the permeability of the matrix start to be significant from a certain critical value, at which the effect of the embedded channels becomes weaker. That is, fluid flow will be

shared between the vugular channels and the porous matrix.

Popov et al. [23] studied single fluid flow through a 2D porous matrix with randomly distributed elliptical vugs. In general, it was seen that regions with high density of isolated vugs have higher equivalent permeability. In a heterogeneous porous matrix, regions of high permeability can connect isolated vugs that would otherwise be unconnected, leading to creation of high-permeability channels that substantially increase the effective permeability of the whole medium. When the vugs are connected through fractures, the effect depends on their aperture. Short-range fracture networks change the permeability of the medium by a factor of 2 to 4, while long-range, large-aperture fractures may affect this property by several orders of magnitude. The works carried out by Arbogast et al. [22] and Huang et al. [24] achieve similar conclusions.

Huang et al. [24] also studied the effect of vug geometry in a 2D single-vug porous media. Four base cells with cavities of different shapes were studied: (a) disk, (b) square, (c) hexagonal, and (d) cross-shaped, maintaining the same macroporosity and permeability of the matrix in all of them. The percentage deviation regarding the effective permeability of the square-vug porous media was reported as -3.01% (disk), -2.10% (hexagonal), and 187.7% (cross-shaped). These values suggest that the effective permeability of a concave vug is quite different from that of a convex one. Longer cavities in the same direction of flow, or in an extreme case, fracture-like cavities, lead to higher equivalent permeabilities. It is argued that because it is a single-vug cell, the system is practically insensitive to the location of the cavity and the permeability of the porous matrix.

In single-phase flow, it is clear that connectivity, size, geometry, orientation, and distribution of vugs are representative variables affecting the hydraulic behavior of heterogeneous porous media. Of particular interest in this dissertation is how these variables affect the two-phase flow behavior. The next section addresses this topic.

3.4

Two-phase flow in vugular porous media

The first references on multiphase flow in vuggy carbonates report on experimental uncertainties in imbibition and drainage core-flooding experiments. Ehrlich [12], Archer and Wong [19] and Corey and Rathjens [66] state that high vug densities lead to early water breakthrough, reduce sweep efficiency, and consequently oil recovery is lower. Vugs scattered throughout the porous

matrix connect the intergranular space in such a way that inter-vugular or vug-matrix-vug flow channels are created. These channels, depending on the surface wettability, may offer less resistance to the flow of one of the fluids.

Forced imbibition experiments on carbonate samples show that the heterogeneity of the porous medium lead to results that are contradictory to classical fluid flow theories. Archer and Wong [19] noted that relative permeability curves calculated from laboratory waterflooding history by the method of Johnson, Bossler and Nauman [67] are unsatisfactory. They argue that the observed breakthrough time is not that of the main flow front. Ehrlich [12], in co-injection experiments of water and oil, observed that the permeability curves have important plateau regions. This behavior was attributed to sequential displacement of the non-wetting phase, first in the region of connected macroporosity, and then in the matrix and unconnected macropores. It was suggested that when a non-wetting fluid is injected, it will seek its way through the vugular space due to the low capillary pressure required for invasion.

deZabala and Kamath [13] used CT scanning and pressure drop measurements to determine the relative permeability to water in an oil-wet vuggy carbonate rock sample. Anomalies in the shape of the curve were found when determined from non-steady state waterflooding data. The steady-state co-injection method proved to be more accurate. In this case, uncertainties introduced by an early water breakthrough were mitigated. Further oil displacement tests by sequential water injection at increasing flow rates showed that, at the connate water saturation, most of the vuggy porosity is saturated with oil. Then, as water is injected, most of the high porosity regions are quickly swept, leaving large unswept areas in the porous matrix with high oil saturation. At higher flow rates, additional oil is recovered by water penetration into the less porous sections. This sequence of events during waterflooding with increasing flow rates was also observed later by Dabbouk et al. [27].

The analysis of displacement fronts in vuggy carbonates was extensively studied by Vik et al. [15] and Dabbouk et al. [27]. It was reported that, for both miscible displacement and imbibition and drainage processes, the displacement front is distorted by growth of advancing fingers into the vuggy and matrix regions of high permeability. However, when the advanced front moves into a less heterogeneous region, further development is prevented and the front is stabilized. These results may explain the early water breakthrough observed in vugular porous media.

Moctezuma-Berthier et al. [14] determined the oil saturation profiles and displacement kinetics in two water-wet vuggy carbonate rocks during forced

imbibition, analyzing them in terms of vug connectivity. Early breakthrough was associated with the flow of water through a main system of high permeability consisting of connecting vugs. Whereas, piston-like displacement (with most of the oil produced at the water breakthrough) was observed when the macropores are not well connected and only accessible through the matrix. Furthermore, they argue that isolated vugs constitute important oil reservoirs, but also oil traps since this phase remains isolated there once the matrix is invaded by water.

Pairoys et al. [68] performed imbibition and drainage experiments on a homogeneous sandstone core in which three artificial cylindrical vugs were laterally drilled to the main flow direction. During drainage, the vugs were sequentially saturated with oil at near zero capillary pressure, and while saturated, the water/oil front remained immobile in the matrix. During imbibition, early water breakthrough was observed and vug saturation was not sequential but occurred simultaneously with imbibition of the matrix. They conclude that the preferential drainage of vugs in a porous matrix dramatically affects the pressure drop curve, exhibiting plateau regions.

Numerical studies on 3D digital vuggy rocks have emulated the observations from the experimental studies described above, especially, in terms of early water breakthrough, strong anisotropy, hysteresis, and changes in the dynamics of pressure drop and flow pathways during waterflooding [14, 24, 69]. In addition, it has already been observed that the inclusion of vugs in the porous matrix has a significant impact on the relative permeability of the non-wetting phase, even in media with isolated vugs. This phase preferentially flows through the vugular space and connects the porous media. As expected, it has also been reported that the wetting phase preferentially saturates the porous matrix, and therefore its relative permeability is not significantly altered by the inclusion of vugs [9, 32, 69].

Kusanagi et al. [21] conducted a hybrid study comparing numerical simulations with experimental measurements. It is shown that the behavior of steady-state relative permeability curves for water and oil in 3D vuggy carbonate rocks depends on the vug connectivity and distribution. They found three types of relative permeability curves for the non-wetting phase, characterized by changes in its concavity. Concerning a rock with larger vug pores having 2D fracture-like distributions, the curve resulted in a straight line, like the X-shaped model usually used to represent the relative permeability in fractured porous media [70]. In that context, Akin and Erzeybek [69] using a 3D pore network model, postulated that when two or more vugs are close to each other or a vug is significantly longer than the other elements in the

porous network, the medium acts as a fracture one leading to a nearly straight relative permeability curve.

In two-phase flow in vugular porous media, the aforementioned studies evidence that the presence of vugs has an important effect on the fluid flow behavior of the non-wetting phase, which preferentially flows through the vugular space. Consequently, key macroscopic properties such as relative permeability must be carefully considered, since non-uniform fluid phase distributions are found throughout the porous medium. Depending on the structure of the vugular space, the interpretation of results based on average fluid saturations for the entire porous medium can lead to erratic interpretations of the fluid flow behavior. It is notable that experimental data on pore occupancy, phase distribution, and two-phase flow regimes in vugular porous media are very valuable information for the interpretation of relative permeability curves.

3.5

Flow regimes of multi-phase flow in porous media

This section addresses some characteristics of flow regimes found in two-phase mobilization processes in porous media. Conventional theories suggest that when a non-wetting phase is being displaced by a wetting phase, either in carbonate rocks or sandstones, only connected flow pathways and ganglia dynamics can occur at the pore scale [46, 71]. Recent studies of steady-state multiphase flow co-injection in core samples scanned by CT microtomography have shown dynamic changes in the connectivity of phases flowing through the porous media [53, 62, 63]. This phenomenon is referred to as *intermittent pore occupancy* and is not a manifestation of non-wetting phase ganglia advection through the porous space, but rather occurs when the non-wetting phase temporarily forms pathways to increase its conductance [53].

Reynolds et al. [53] reported this flow behavior for a brine- N_2 system in a Bentheimer sandstone at low capillary number (Ca). Comparably, Gao et al. [62] observed intermittent pore occupancy during simultaneous injection of decane and brine at $Ca = 7.5 \cdot 10^{-6}$. In carbonate rocks, Gao et al. [72] and Spurin et al. [63] identified intermittency in the steady-state values of pressure drop and fluid saturation of decane and brine at $Ca \approx 10^{-6}$. Both microporosity and macroporosity regions were occupied intermittently by the wetting and non-wetting phases. This competition was predominantly located in the smaller and intermediate-size pores and throats.

Gao et al. [54] expanded the investigation on decane-brine flow in Bentheimer sandstones over a broader range of capillary numbers. It was found

that at $Ca < 10^{-6}$, the relationship between flow rate and pressure gradient is linear and both phases follow fixed flow pathways. When $Ca \approx 10^{-6}$, the onset of dynamic fluctuations in pressure drop (at constant fractional flow) is identified. Finally, at $Ca \geq 10^{-5}$, the intermittent flow regime dominates the steady-state fluid flow in a significant fraction of the pore space. In this regime, the relationship between capillary number and pressure gradient becomes nonlinear, which was associated with rapid changes in the fluid configuration at the pore scale.

Spurin et al. [73] observed for a brine- N_2 system in carbonates rocks that the relative permeability of the non-wetting phase remains unchanged at low capillary numbers, for which pore geometry controls the location of intermittency. However, as the capillary number increases, higher relative permeabilities were identified. Although the intermittent flow regime tends to reduce the number of larger ganglia, the overall effect is an increase in the non-wetting phase connectivity.

It is suggested that intermittent pore occupancy is governed by the competition between viscous and capillary forces along the porous medium, being the energy introduced by injecting the fluids responsible for the creation of intermittent connections [54]. Additionally, it is indicated that this phenomenon could also be controlled by the heterogeneity of the porous medium and the mobility ratio of the fluids [63]. Most of these observations represent novel advances toward a more realistic understanding of the physics of multi-phase flow in porous media under a wide variety of conditions and injection mechanisms.

3.6 Research gaps

Continuing scientific advances in core flooding experiments and numerical simulations have improved understanding of single-fluid flow behavior in a wide variety of vugular porous media. However, despite best efforts, up to now it has not been possible to experimentally and systematically correlate the macroscopic behavior of two-phase flow observed in vugular porous media with pore-scale physics, and to make comparisons with respect to the behavior of an equivalent porous matrix without vugs. In core flooding experiments, due to difficulties in scanning the fluid flow at the pore scale and obtaining reliable samples [14, 21]; and, in experiments on rock models, due to gross assumptions that limit the realism and, more importantly, to lack of information on the phase distribution throughout the porous medium [9, 32, 69].

3.7

Dissertation goals

The main objective of this work is to visualize and analyze the simultaneous flow of water and oil in micromodels of vugular porous media for the determination of relative permeability, quantification of fluid saturations, and correlation of macroscopic variables with the behavior observed at the pore scale. To achieve this objective, four stages are contemplated:

1. Prototype a porous matrix with a random network of straight and constricted microchannels, and scatter different types of macropores with simple geometries. From these models, manufacture molds that allow the replication of the vugular porous media as PDMS-based micromodels, and provide a complete characterization of their pore space.

2. Assemble a robust setup for micromodel-flooding experiments that ensures both refined fluid flow visualization at the pore scale and measurement of flow rate and pressure drop.

3. Conduct single- and two-phase flow steady-state experiments in porous media micromodels to measure absolute permeability and relative permeability to water and to oil. In particular, evaluate the effect of the incorporation of vugs on the porous matrix in terms of occupancy of the porous space, fluid distribution, and permeability.

4. Perform oil displacement experiments by water injection in the PDMS-based micromodels, and evaluate oil recovery efficiency based on the morphology of the vugular space.

4

Materials and methods

This chapter describes in detail the experimental methodology that was developed to investigate the flow behavior of water and oil in PDMS/glass micromodels with different configurations of porous media.

4.1

General description of experiments

For the design of experiments, three premises were considered:

- (i) simultaneous injection of water and oil into the micromodel;
- (ii) measurement of pressure drop through the porous medium;
- (iii) high-quality visualization of fluid displacement at the pore scale.

To meet these needs, an experimental setup was assembled as shown by the simplified diagram in Figure 4.1 and by the photograph in Figure 4.2. Hereinafter, the experimental set-up is also referred to as the micromodel-flooding setup.

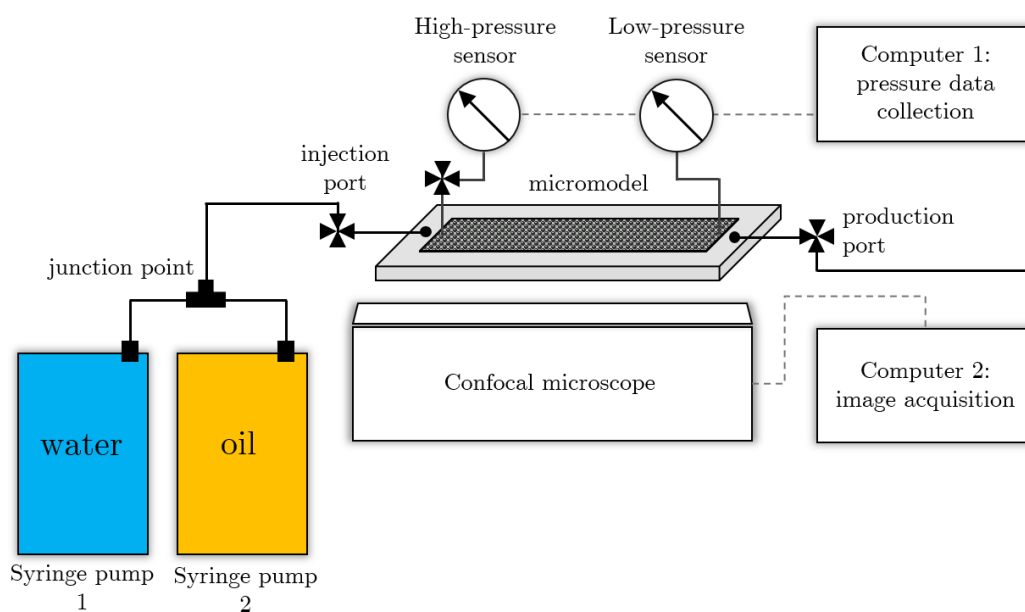


Figure 4.1: Simplified diagram of the micromodel-flooding set-up.

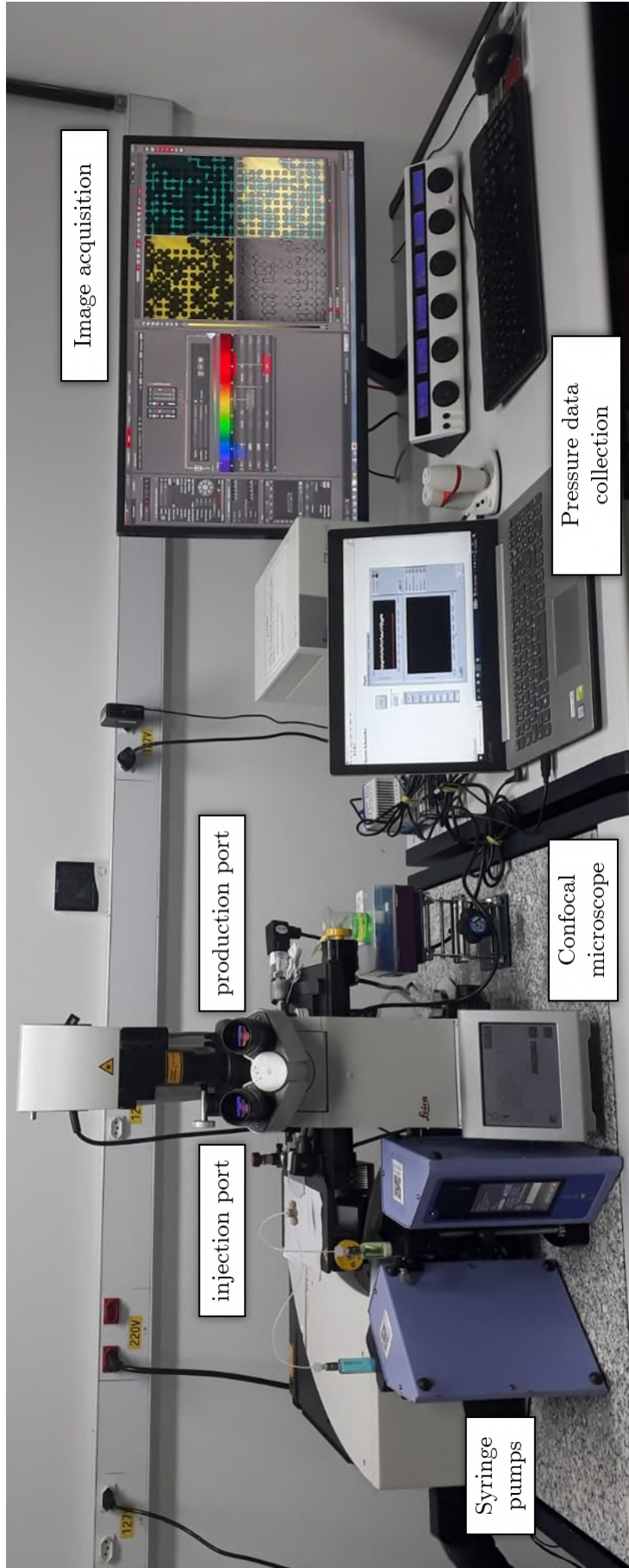


Figure 4.2: Photograph of the micromodel flooding set-up.

Details of the components that make up the micromodel-flooding setup are described below. They are highlighted in Figures 4.3 and 4.4.

1. Flow visualization system

A confocal Laser Scanning Microscope (TCS SP8 from Leica Microsystems) coupled to a computer is used for live visualization and image acquisition. This inverted light microscope have a motorized stage, 4 laser excitation wavelengths (405, 488, 552 and 638 nm) and 4 light detectors (2 PMT SP fluorescence detectors, 1 HyD SP detector and 1 transmitted light detector).

2. Injection system

It is composed of two single-syringe pumps (model Elite 11 from Harvard Apparatus) operated with Hamilton® glass syringes of 10 mL. These pumps supply water and oil at a constant flow rate through PTFE tubing of 794 μm ID (Cole-Parmer). Both flow lines are then connected to a microfluidic tee assembly or junction point (MicroTee), which delivers simultaneous flow of water and oil through PTFE tubing of 250 μm ID (Cole-Parmer). The MicroTee (model P-890 from IDEX) has an internal orifice of 150 μm and dead volume of 58 nL. The two-phase injection system can be switched to single-phase injection mode by interrupting the flow of water or oil from the syringes.

3. Injection and production ports

Two four-way valves (model V-101L from IDEX) placed on the microscope stage direct the flow that is injected into the micromodel through 250 μm ID tubing and that is produced from the micromodel through 794 μm ID tubing. The valve at the production port directs the produced flow to a waste vessel. If necessary, the internal volume of the system can be sealed by closing both valves.

4. Pressure measurement apparatus

A high-pressure sensor (103 kPa with 0.25 kPa accuracy from Velki) and a low-pressure sensor (10 kPa with 0.05 kPa accuracy from WIKA) are connected to the inlet and outlet of the porous media micromodel, respectively. The connection line of the high-pressure sensor is provided with a valve to relieve pressure if needed. Both sensors are connected to a universal analog input module (model NI-9201 from National Instruments) and a computer for pressure data collection.

5. Porous media micromodel

The PDMS/glass micromodel has an inlet and outlet for the injection and production of fluids and two additional holes that are connected to the pressure transducers. A complete description of these micromodels is provided in section 4.3.

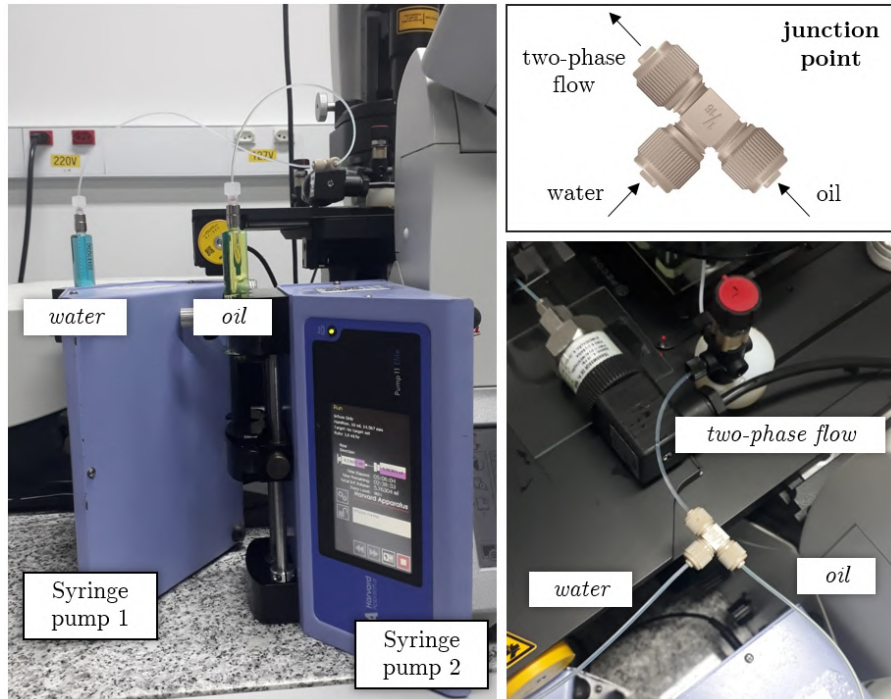


Figure 4.3: Injection system details.

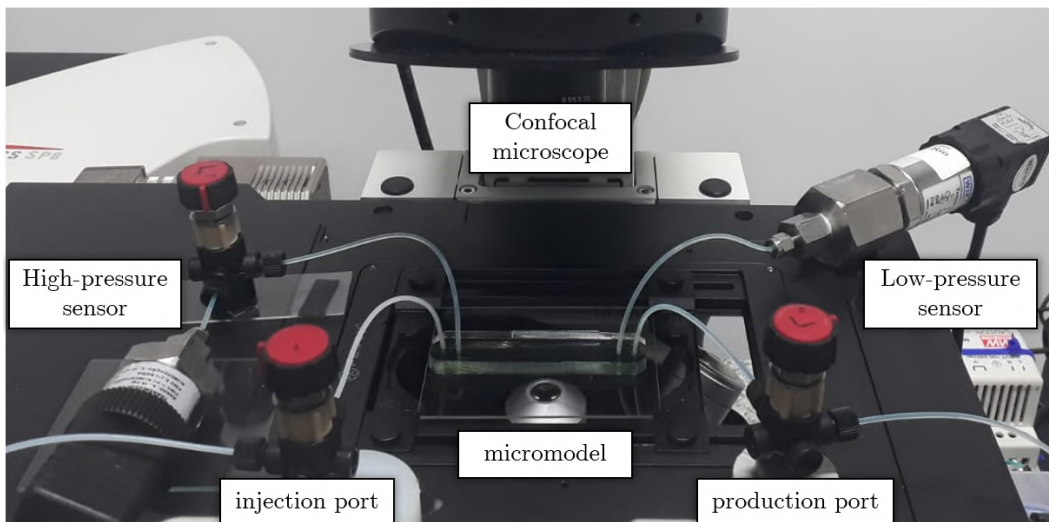


Figure 4.4: Experimental setup on the microscope motorized stage.

4.2

Fluids and their properties

Model fluids of aqueous and oleic phases were selected for the two-phase flow experiments in porous media micromodels. Milli-Q® water was used as the aqueous phase and two paraffinic base oils as oleic phases: Drakeol® 7, a lower-viscosity mineral oil, and 500 PS®, a higher-viscosity oil (both from Agecom, Brazil). Fluorescent pigments were added to all fluids. Methylene blue (Merck, Germany) to the aqueous phase at 0.0004 wt.% and Oil-Glo® Ultra SPI-OGG-16 (SpectroLine, USA) to the oleic phases at 0.1 (v/v)%.

After preparation, the fluids were filtered using Millipore® Membranes in order to ensure dust-free conditions within the micromodels. The aqueous phase was filtered at 0.45 μm and the oleic phases at 5 μm .

Based on the experiments, two water-oil systems were considered:

- ✘ *System 1* comprises the aqueous phase and the low-viscosity oil, which were used to perform steady-state relative permeability measurements.
- ✘ *System 2* comprises the aqueous phase and the high-viscosity oil, which were used to perform oil displacement tests by waterflooding.

All the experiments were performed at 22° C. Viscosity (μ) and interfacial tension (γ_{wo}) were measured at that temperature for fluids of system 1 and system 2. Average values are listed in Table 4.1. The water-oil interfacial tension was measured by a DCAT 25 tensiometer (DataPhysics Instruments) using the Wilhelmy plate method. The dynamic viscosity was measured in a Discovery hybrid rheometer (DHR-3 from TA Instrument), using the double-walled concentric cylinder geometry for the low-viscosity fluids (aqueous phase and Drakeol® 7) and the cone-plate geometry (with 2° angle and 40 mm diameter) for the high viscous fluid (500 PS®). Both the aqueous and oleic phases exhibit Newtonian behavior over a shear rate of 10 to 100 s^{-1} .

Table 4.1: Viscosity (μ) and interfacial tension (γ_{wo}) measured at 22° C for fluids of system 1 and system 2.

	System 1		System 2	
	<i>Aqueous phase</i>	<i>Oleic phase</i>	<i>Aqueous phase</i>	<i>Oleic phase</i>
μ (cP)	0.94 \pm 0.01	20.40 \pm 0.03	0.94 \pm 0.01	232.0 \pm 0.1
γ_{wo} (mN/m)	13.2 \pm 0.3		15.9 \pm 0.1	

4.3

PDMS/glass porous media micromodels

2D porous media micromodels were fabricated following standard soft lithography techniques [74, 75]. The microfabrication process was carried out in a clean room facility of the Laboratory of Microhydrodynamics and Flow in Porous Media (LMMP) at PUC-Rio. Single-use devices were produced for each experiment. The complete microfabrication protocol is described below.

4.3.1

Porous media design

Porous media with different pore space arrangements were designed using AutoCAD®. In this work, four pore space configurations were contemplated: a homogeneous porous matrix without vugs and three porous media with vugs (the homogeneous porous matrix with embedded vugs).

The Porous Matrix

Figure 4.5 shows the general design of the micromodels. The porous matrix consists of a capillary network with a repetitive 3 mm · 3 mm cell of 10 · 10 connected-channel arrangement of randomly distributed straight and constricted microcapillaries. All the channels have square profile of approximately 100 μm depth · 100 μm width, and the constrictions have a width of either 45 μm or 75 μm.

The micromodel has two rectangular cross-section chambers between the inlet/outlet points and the porous medium, intended for better distribution of fluids that are injected into and produced from the pore space.

The vugular porous media

Identical vugs with rectangular geometries at random positions were embedded in the porous matrix. As illustrated in Figure 4.6, three configurations were considered and are classified based on their vug geometry and macroporosity. The geometric parameter considered was the aspect ratio of the vug (AR), defined as the ratio between the length of the vug in the main direction of flow (L_v) and its width (W_v). The area-based macroporosity (ϕ_v) was defined as the ratio between the total vug area and the 2D porous media area. In configurations T_1 and T_2 , the macroporosity was set at 12.6% with aspect ratios of 1.6 and 5.9, respectively. In configuration T_3 , the macroporosity was set at 8.4% keeping the same aspect ratio of T_1 . Hereinafter, these designs will be referred to as *vugular porous media*.

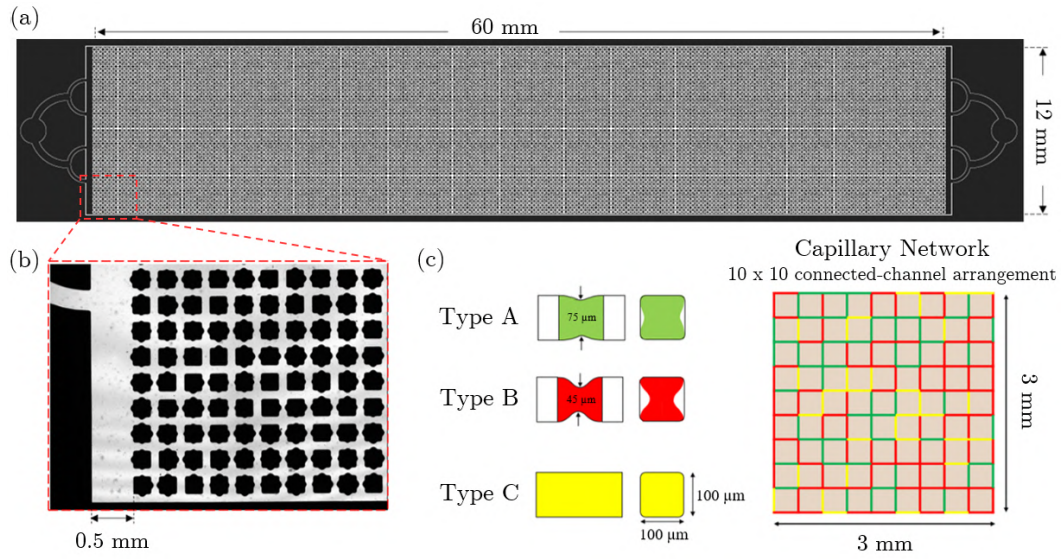


Figure 4.5: General design of the 2D porous media micromodels. (a) Porous matrix design. (b) Zooming in on the injection chamber and pore space of the porous matrix. (c) Arrangement of constricted (type A, B) and straight (type C) channels on the capillary network cell.

PUC-Rio - Certificação Digital N° 2012357/CA

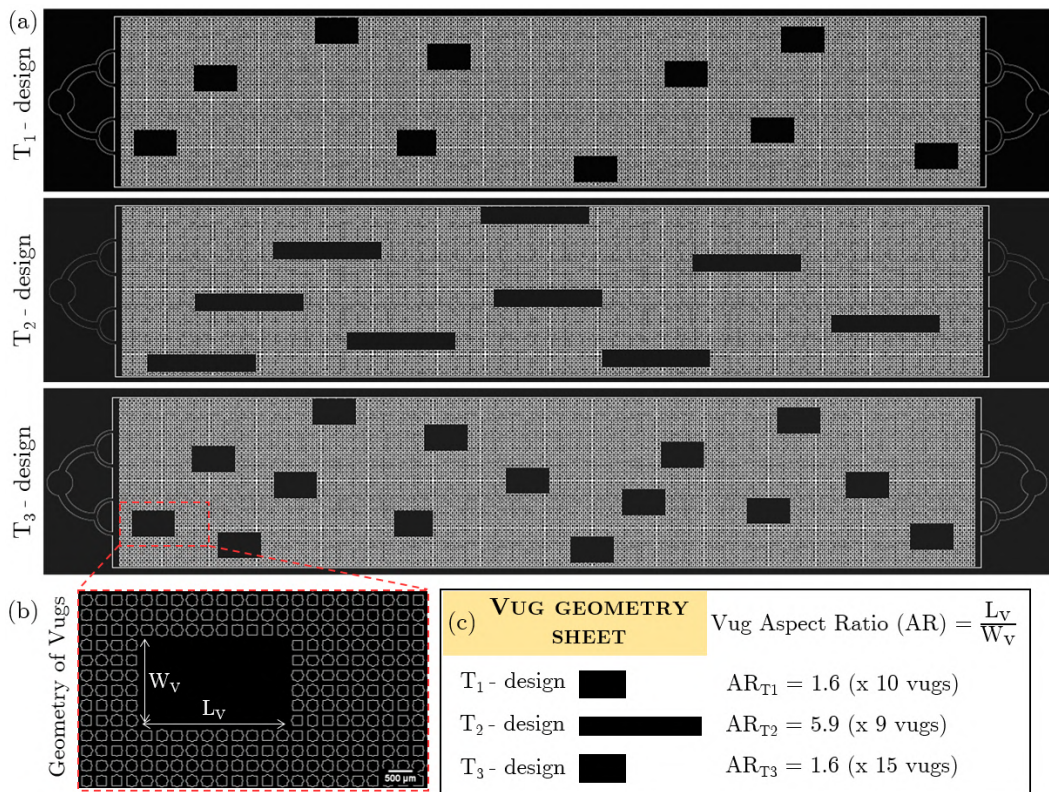


Figure 4.6: Vugular porous media micromodels. (a) Configurations of vugular space. (b) Zooming in on a random vug with W_v width and L_v length. (c) Vug aspect ratio details.

4.3.2

Mold fabrication

In this stage, the porous media designs described above were first transferred to photomasks and then onto silicon wafers by soft-lithography. Master molds of the porous matrix and of the three vugular porous media micromodels were fabricated.

The photomasks were printed by a private printing company (Arte Digital, Brazil) at a resolution of 3000 dpi (dot $\sim 8 \mu\text{m}$ in diameter). Molds were produced in-house from a negative photoresist used as an etch mask with a desired depth of $100 \mu\text{m}$. For the fabrication of each one, a 100 mm silicon wafer was spin-coated at 2100 rpm for 30 s with SU-8 photoresist (Kayaku Advanced Materials, USA), followed by baking steps at 65°C and 95°C . The photomask was then etched into the mold using a UV-KUB 2[®] masking system (Kloé, France) at 84% power for 8 s. After that, the mold was resubmitted to the 65°C and 95°C baking steps and developed using propylene glycol monomethyl ether acetate (PGMEA) as a photoresist solvent. Finally, the mold was dried with compressed air and heated at 120°C for 10 minutes.

4.3.3

PDMS stamps and micromodel sealing

The porous media designs from the master molds were patterned on PDMS pieces, which constitute the main part of the micromodels. For that aim, Polydimethylsiloxane (PDMS, Sylgard 184 elastomer kit from Dow Corning, Germany) was mixed at a 10:1 polymer/cross-linker ratio and placed under vacuum. After degassing, the mixture was poured onto the molds and cured inside an oven at 80°C for 2 h. The PDMS stamps were then peeled off from each mold, cut into desired shapes, punched to make the inlet/outlet and pressure measurement holes, and cleaned with Scotch[®] Magic[™] tape.

Microscope glass slides (Perfecta, Brazil) constitute the bottom surface of the porous media micromodels. Prior to sealing, these glass slides were thoroughly washed with acetone and isopropyl alcohol and dried with compressed air. Finally, the PDMS pieces were irreversibly bonded to them by oxygen plasma treatment using a plasma cleaner (model PDC-001 from Harrick Plasma) at 0.5 Torr and 30 W for 2 min.

Figure 4.7 exemplifies the transfer sequence of porous media designs from the photomasks to the final device.

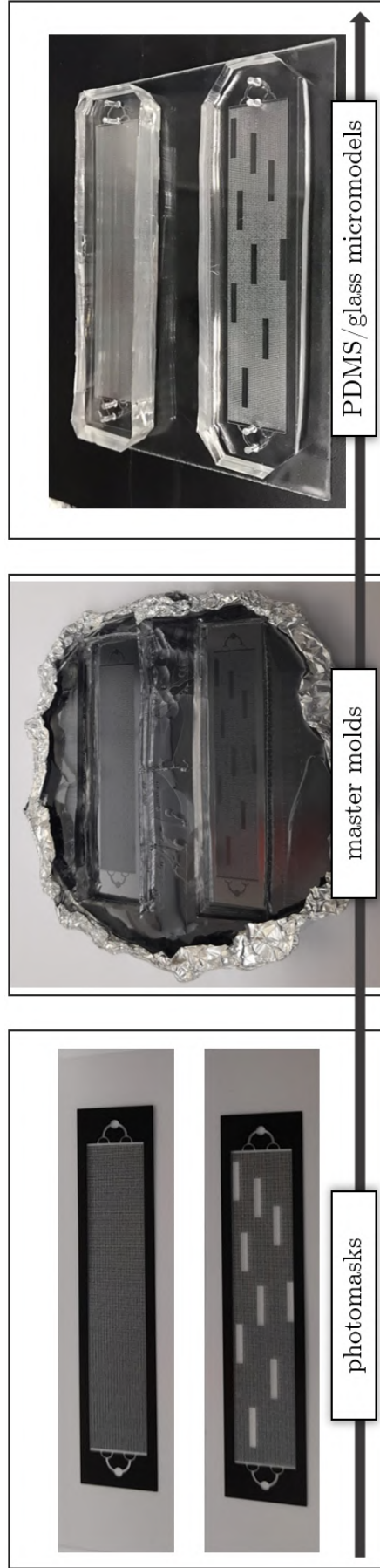


Figure 4.7: Transfer sequence of the porous matrix and T_2 vugular porous media designs from the photomasks to the final devices.

4.3.4 Pressure measurement holes

As illustrated in Figure 4.8, the pressure measurements were made through two 1 mm OD holes located at the center of the inlet and outlet distribution chambers. It was observed that external measurements are not reliable, since the pressure drop along the connections of the experimental set-up and the inlet and outlet channels of the micromodels is comparable to that exclusively caused by the porous medium.

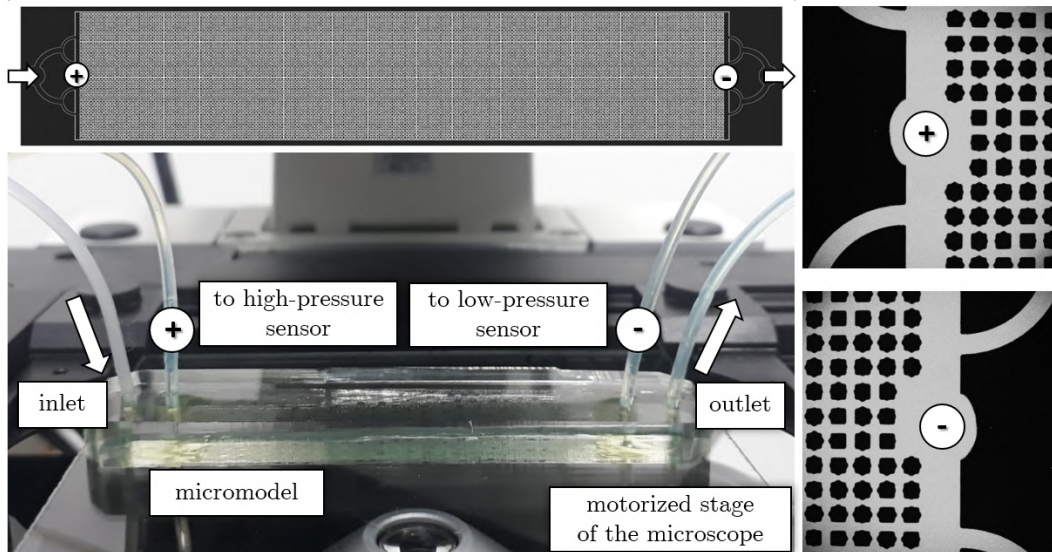


Figure 4.8: Details of the inlet/outlet flow lines and pressure measurement points in the PDMS/glass micromodel.

4.4 Geometric characterization of micromodels

The micromodel characterization was carried out by optical imaging using confocal and fluorescence microscopy techniques. It included the determination of the mean cross-sectional height, channel-size distribution and porosity for the porous matrix and the vugular porous media micromodels.

The *cross-sectional height* was obtained by quantifying the light reflected from the lower (glass) and upper (PDMS) interior surfaces that enclose the pore space. An entire optical scan along the z-axis was performed on $1.5 \mu\text{m} \cdot 1.5 \mu\text{m}$ horizontal sections of the porous media exposed to a 638 nm laser. As shown in Figure 4.9, the difference between the two peaks exhibited on the light intensity profile corresponds to the local height in that section of the micromodel. These peaks are associated with the position of the interior surfaces.

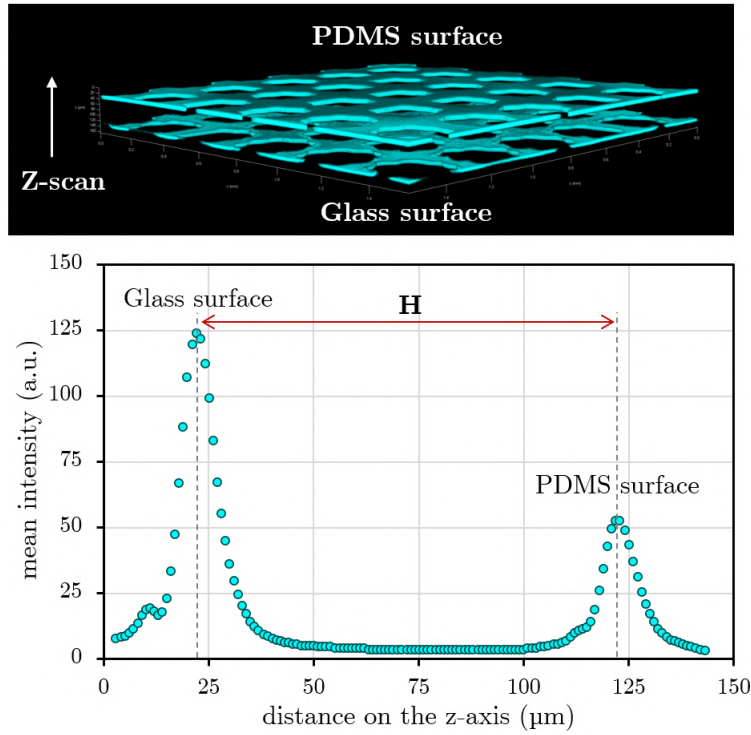


Figure 4.9: Confocal microscopy-based method to determine average height of the PDMS/glass porous media micromodels. (a) Detection of the chip's borders along a Z-scan by quantifying the light reflected from the lower (glass) and upper (PDMS) interior surfaces. (b) Light intensity profile, enabling the determination of local height (H).

Next, the average height (\bar{H}) of each micromodel was calculated by combining the z-scan with a tile-scan over the entire micromodel area. In order to make the surface detection sufficiently fine, the z-step size was defined to be $1 \mu\text{m}$. This novel non-contact technique for height determination was validated in two commercial glass micromodels: Dolomite® and Micronit® devices, whose exact height is known (100 and $20 \mu\text{m}$). The absolute error resulted in less than 5% .

The *channel-size distribution* and *porosity* were obtained from high-resolution imaging of the porous media saturated with the oleic phase of system 1. This fluid was selected due to its lower viscosity and reliability in saturating the whole pore space at low injection flow rates. The distance between every two neighboring pillars throughout the porous media (D) and the 2D projection of the pore volume (A_p) were measured by means of image processing.

The area-based micromodel porosity (ϕ) was calculated as $\phi = A_p/A_t$, where A_t is the total area covered by the porous media. Similarly, the area-based macroporosity (ϕ_v) was calculated as $\phi_v = A_v/A_t$, where A_v is the 2D projection of the pore volume occupied by vugs.

In addition, the 2D projection of the pore volume and the average height were useful to calculate the micromodel pore volume (V_p) as $V_p = A_p \cdot \bar{H}$.

4.5 Surface wettability characterization

According to contact angle measurements with water in an air atmosphere, PDMS is a hydrophobic material ($\theta > 90^\circ$), while glass is naturally hydrophilic ($\theta < 90^\circ$) [76]. During microfabrication, the oxygen plasma treatment performed to bond the devices renders the PDMS surfaces of microchannels water-wet during the first 8 hours, but after 72 hours their hydrophobic nature is completely recovered [77]. In this work, all the micromodels were used after 72 hours of bonding to guarantee their natural surface wettability.

Contact angle measurements with the same fluids involved in the two-phase flow experiments were carried out in a Tracker™ drop tensiometer (Teclis) using the sessile drop method. Two surfaces were studied: a non-patterned layer of PDMS and a glass slide. Both samples were prepared, cleaned and plasma-treated in the same manner as described in the microfabrication protocol.

To perform the measurement, each sample was submerged in a transparent cell filled with the oleic phase. After 30 minutes, a 30 μl drop of the aqueous phase was deposited on the surfaces using a motor-driven syringe. The static contact angle was then measured from images of the sessile drop until it showed no significant variation. Mean values were averaged from three independent samples. Figure 4.10 displays the measurement scheme adopted.

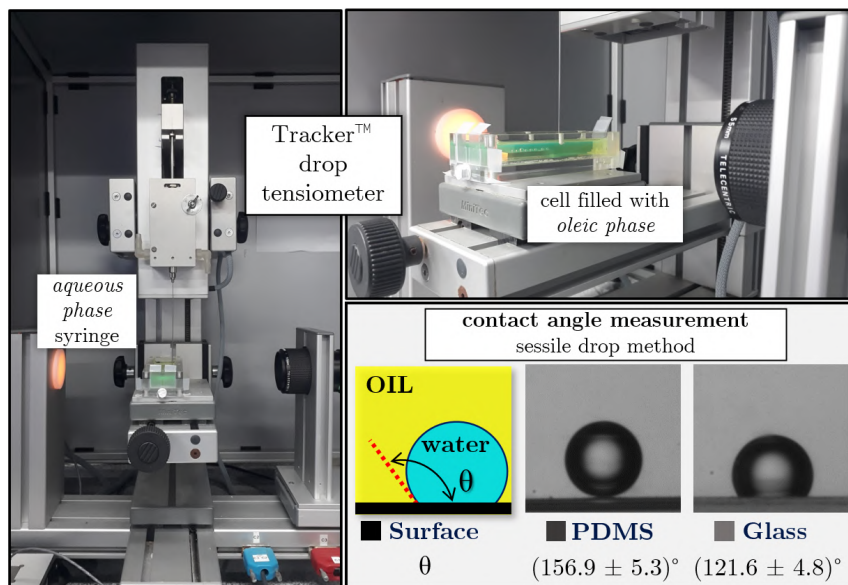


Figure 4.10: Contact angle measurement scheme for a sessile drop of aqueous phase on PDMS and glass surfaces submerged in Drakeol® 7 atmosphere.

For system 1, the contact angle of the aqueous phase in the oil atmosphere was measured to be $(156.9 \pm 5.3)^\circ$ on PDMS and $(121.6 \pm 4.8)^\circ$ on glass. Measurements with system 2 showed similar results.

4.6

Experimental procedure

4.6.1

Single-phase flow Experiments

The absolute permeability of micromodels (K_{abs}) was calculated from measured values of pressure drop across the porous media (ΔP) during the flow of Drakeol® 7 at different flow rates (Q). This measurement scheme is based on Darcy's law equation (Eq. 2-1).

The experiments were conducted in the micromodel-flooding set-up by switching the mode to single-phase flow. Single-use micromodels were flooded with the oleic phase at a constant flow rate of 0.25 ml/h until complete saturation of the pore space. From this point forward, increasing injection flow rates were set (0.5, 0.75, 1, 1.25 and 1.5 ml/h), and at the steady state, the pressure at the inlet (P_i) and at the outlet (P_o) of the porous media was recorded. The steady-state condition was considered after at least 30 minutes of injection when the pressure did not show variation over time. The absolute permeability of the porous matrix and the three vugular porous media micromodels was calculated from the average of three independent experiments.

4.6.2

Two-phase flow Experiments: Relative Permeability Measurement

Measurements of steady-state relative permeability to water and oil were performed under identical two-phase flow conditions in the porous matrix and in the vugular porous media micromodels. The micromodel-flooding set-up was used to conduct the experiments with the fluids of system 1: the aqueous phase and the low-viscosity oleic phase.

Initially, single-use micromodels were completely saturated with the oleic phase following the protocol described in the previous subsection. Next, both the aqueous and oleic phases were simultaneously injected into the porous media at a constant total flow rate (Q_t) of 2 ml/h. Depending on the individual flow rates of water (Q_w) and oil (Q_o), a predefined fractional flow of water ($f_w = Q_w/Q_t$) was established in the co-flow stream. By manipulating the

value of f_w , various steady state saturation levels were reached in the pore space.

At each steady state condition, the pressure at the inlet and at the outlet of the porous media was recorded and a complete image of the micromodel was acquired. It is important to note that the steady state condition was assumed from a stable value of pressure drop ($\Delta P = P_i - P_o$) after at least 30 minutes of simultaneous injection of water and oil. In addition, during image acquisition, the injection was not stopped in order not to alter the pore occupancy of fluids in the porous media.

Based on the multiphase extension of Darcy's Law (Eq. 2-3), the effective permeability of each phase ($K_{eff,i}$) was calculated from the injection flow rate of this phase (Q_i) and the pressure drop at steady state (ΔP). The relative permeability ($K_{r,i}$) corresponds to the ratio between the effective permeability and the absolute permeability of the porous media.

As a key point of this measurement scheme, the predefined f_w value in the co-flow stream provides the relative permeability to water and to oil at the steady state saturation level achieved in porous media. Consequently, by changing the water flow ratio in a stepwise fashion, and repeating pressure measurements as the new equilibrium is reached, several relative permeability values were calculated at several saturation levels. The value of f_w was swept in 0.1 increments from 0 (oil injection) to 1, which corresponds to the endpoint of the experiment where only the aqueous phase was injected. The relative permeability curves were finally calculated from the average of two independent experiments.

The saturation of each phase in the entire porous medium was calculated by means of image processing. The method used is explained in detail in Section 4.8.

4.6.3

Two-phase flow Experiments: Oil displacement by water injection

Oil displacement experiments by water injection were performed in the porous matrix and in the three vugular porous media micromodels at $Ca = 10^{-5}$. In this case, to make the residual oil saturation in the porous medium higher, the high-viscosity oil was used. The experiments were carried out with the fluids of system 2.

In single-use micromodels initially saturated with the oleic phase, 15 pore volumes of the aqueous phase were injected at a constant flow rate of 0.58 ml/h. The advance of the waterfront was monitored in order to quantify the breakthrough time. After waterflooding, a complete image of the micro-

model was acquired to observe the phase distribution and quantify the residual oil saturation and/or oil recovery. The large injected volume of the displacing phase guaranteed the achievement of the residual oil saturation, no further mobilization of oil in the porous media was observed at the end of the experiments.

4.7

Image acquisition

The acquisition of high-resolution images of the porous media in the previously described experiments was carried out in the confocal microscope by means of tile scan operations over the PDMS micromodels. The 8-bit images that were obtained are composed of 110 tiles with 10% overlap, arranged in a mesh of 22 tiles in the X direction and 5 tiles in the Y direction. Each tile was acquired with a 5x objective lens in the format of $512 \cdot 512$ pixels. This makes the tile dimensions $3.11 \text{ mm} \cdot 3.11 \text{ mm}$ and the pixel resolution $6.06 \mu\text{m} \cdot 6.06 \mu\text{m}$.

Preliminary studies demonstrated that Methylene blue and Oil-Glo® Ultra SPI-OGG-16 are appropriate pigments to exclusively and independently visualize the aqueous and oleic phases without interference from the porous matrix. These pigments provide maximum light emission over different frequency ranges of the visible spectrum.

In a single tile acquisition sequence, the oleic phase emission was detected between 417-469 nm from excitation with a 405 nm laser (at 50% power), while the aqueous phase emission was detected between 674-740 nm with a 638 nm laser (at 40% power). In this manner, all the images acquired in the two-phase flow experiments were composed of two channels corresponding to the detection of the oleic phase (visualized in yellow color) and the aqueous phase (visualized in cyan color). Figure 4.11 exemplifies this image acquisition scheme. As expected, in the single-phase flow experiments, only the oleic phase channel was needed to visualize the entire pore space.

4.8

Image processing

The independent detection of the aqueous and oleic phases made possible their direct analysis in terms of pore occupancy and distribution throughout the porous media. Image processing was performed individually for each channel, and can be divided into two steps: segmentation and quantitative analysis. Both steps were performed using ImageJ® software.

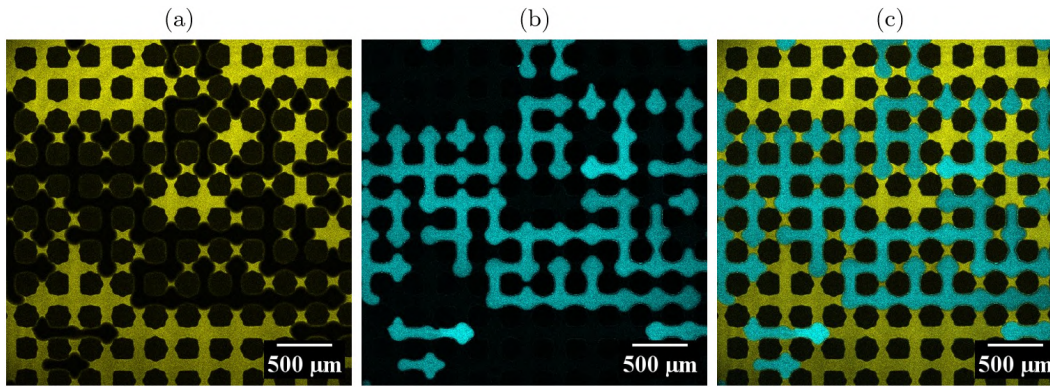


Figure 4.11: Individual tile of the porous media occupied by the oleic and aqueous phases. (a) channel 0: detection of the oleic phase (visualized in yellow color), (b) channel 1: detection of the aqueous phase (visualized in cyan color), (c) merging of channels 0 and 1: the porous matrix is visualized in black color.

In the segmentation step, each pixel on the phase of interest was isolated from the rest of the image by adjusting the 8-bit intensity threshold. The widely used Otsu thresholding method was adopted in this work [78]. The segmentation operation was executed individually on the 110 tiles that make up the complete image of the porous media. In addition, noisy particles were removed using two built-in noise reduction methods (size and despeckling filters) in order to improve image quality. At the end of this step, the total number of pixels in each image had only two intensities: 0 (black in color, rest of the image) and 255 (white in color, phase of interest). Figure 4.12 exemplifies the segmentation of the oleic phase channel from Figure 4.11.

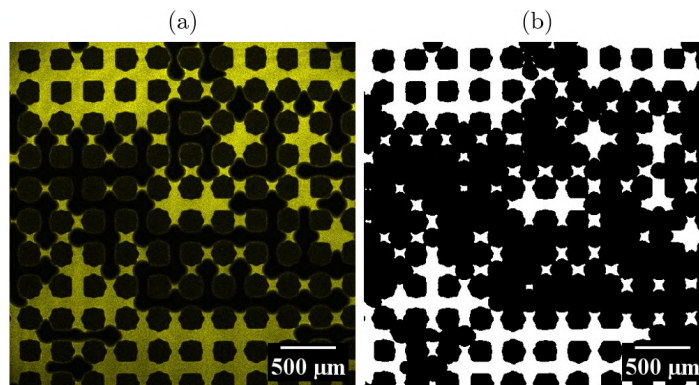


Figure 4.12: Illustration of the segmentation step in image processing. The intensity threshold of channel 0 (a) is suitably adjusted in order to segment the pore occupancy of the oleic phase from the rest of the image (b).

In the quantification step, the pore area occupied by pixels with an intensity of 255 was determined (A_i). This area in relation to the 2D projection of the pore volume (A_p) represents the saturation level of the fluid phase i in the porous medium. Both the area occupied by the oleic phase (A_o) and the

area occupied by the aqueous phase (A_w) were individually determined, and the difference between the total area ($A_o + A_w$) and the 2D projection of the pore volume (A_p) was indicative of the degree of accuracy in the quantification technique used. Differences of less than 2% were found in all fluid saturation measurements.

In that sense, different parameters were calculated according to the approach of the experiment.

- (i) In the single-phase experiments, the 2D projection of the pore volume (A_p) from images of the porous media 100% saturated with the oleic phase ($A_p = A_o$).
- (ii) In the relative permeability experiments, the water and oil saturations (S_w and S_o) from the pore area occupied by the aqueous phase and oleic phases ($S_i = A_i/A_p$).
- (iii) In the oil displacement experiments, the residual oil saturation (S_{or}) from the pore area occupied by the oleic phase after waterflooding ($S_{or} = A_o/A_p$).

In addition to the saturation levels, morphological characteristics of the fluid units that occupy the porous media were analyzed. The size distribution of the oleic phase was determined using a Particle Analysis Filter, which classifies all elements of intensity 255 based on their pixel area.

5

Results and discussions

This chapter reports the results in five main parts: geometric and hydraulic characterization of the PDMS-glass porous media micromodels, analysis of steady-state co-flow and pore occupancy of water and oil in porous media with and without vugs, measurements of steady state relative permeability, and finally, evaluation of oil displacement by water injection in the porous media micromodels.

5.1

Characterization of the PDMS-glass porous media micromodels

5.1.1

Dimensions and pore space features

Figures 5.1 and 5.2 display 2D images of the fabricated porous media micromodels after saturation with the oleic phase. Details of the porous matrix and a partial 3D reconstruction of the randomly-constricted capillary network are included in Figure 5.1. From these images all the characteristic dimensions of the porous media were measured, and the results are listed below.

- ✘ The porous medium is (57.6 ± 0.3) mm long, (11.4 ± 0.2) mm wide and (100 ± 6) μm height in all devices. In addition, the rectangular distribution chambers before and after the porous medium are (0.45 ± 0.05) mm long.
- ✘ The pore volume (V_P) of the porous matrix micromodel is 36 μL , which corresponds to a porosity of $\phi = (0.54 \pm 0.01)$.
- ✘ The macroporosity of the T_1 vugular micromodel is $\phi_v = 7.5\%$, while that of the T_2 and T_3 vugular micromodels is $\phi_v = 11.4\%$. Consequently, the total micromodel porosity is $\phi = 0.57$ in the T_1 , and $\phi = 0.59$ in the T_2 and T_3 devices.
- ✘ The aspect ratio of the vugs (AR) did not show significant differences from the photomasks after microfabrication. It is $AR = 1.7$ in the T_1 and T_3 vugular micromodels, and $AR = 6.2$ in the T_2 device.

Porous matrix

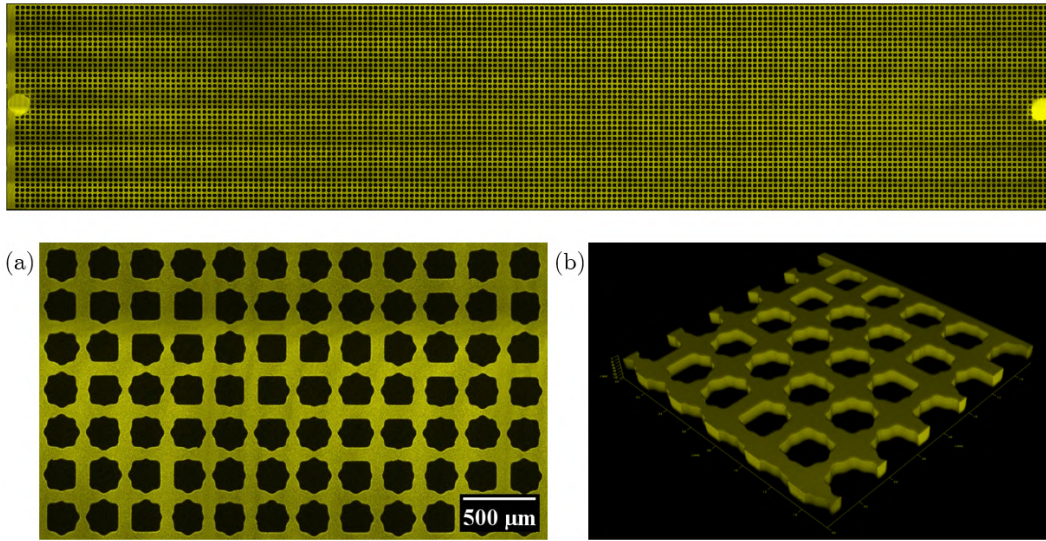
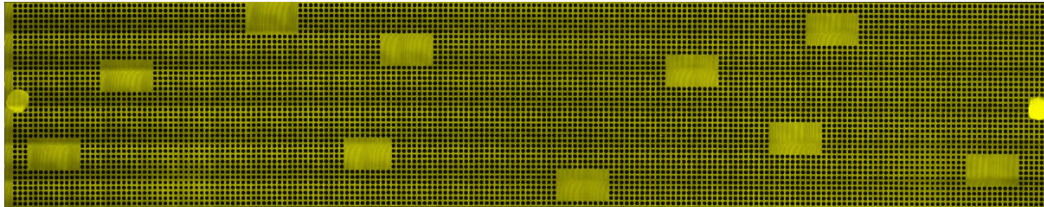
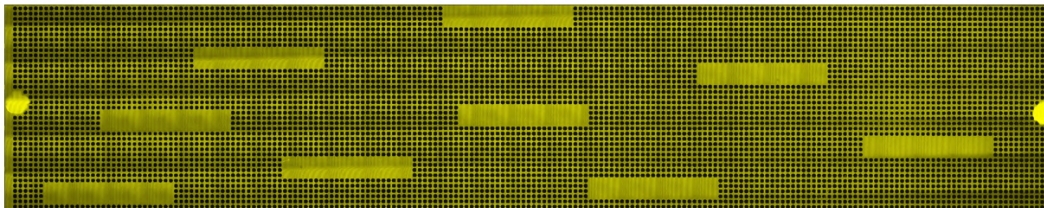


Figure 5.1: Porous matrix micromodel saturated with the oleic phase. (i) Pore-scale details. (ii) Partial 3D reconstruction of the randomly-constricted capillary network.

T_1 vugular media



T_2 vugular media



T_3 vugular media

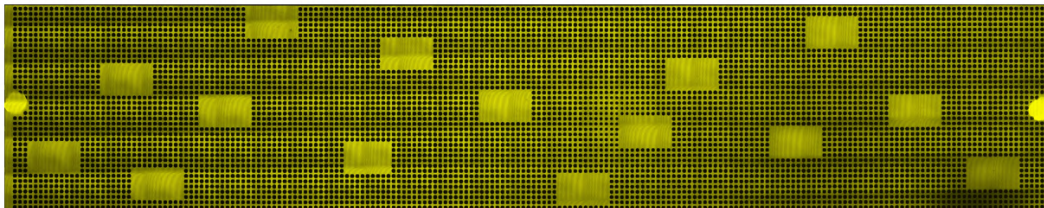


Figure 5.2: Vugular porous media micromodels saturated with the oleic phase.

Figure 5.3 shows the size distribution of straight and constricted channels that forms the pore space of the porous matrix micromodel. Limitations in the printing resolution of the photomasks (dot $\sim 8 \mu\text{m}$ in diameter) led to obtaining a tri-modal distribution with some variation in size for each channel type. The modal size was measured to be $47.8 \mu\text{m}$, $75.6 \mu\text{m}$ and $98.1 \mu\text{m}$ for channels of type A, B and C, respectively. Despite the small differences from the original design, a homogeneous porous matrix with pore throats and channels of various sizes was considered to increase the realism of the fabricated porous media micromodels.

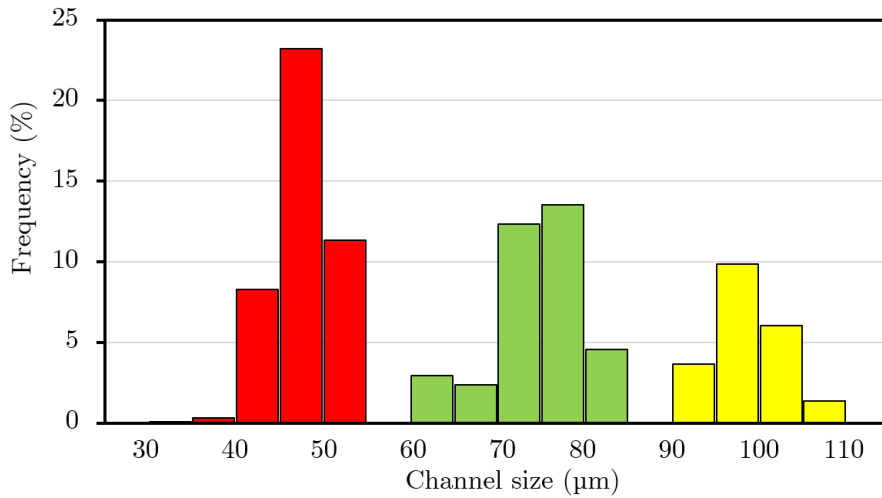


Figure 5.3: Size distribution of straight (type C) and constricted (type A and B) channels of the porous media micromodels.

A key point in this work is the similarity between the porous matrix in the vugular micromodels and the porous matrix in the micromodel without vugs. Differences of no more than $3 \mu\text{m}$ in the modal sizes and no more than 2% in the porosity were found. The latter enables a direct comparison of fluid flow behavior in the porous matrix (micromodel without vugs) with that in the vugular porous media (micromodels T_1 , T_2 and T_3).

Accordingly, the results in the next subsections will be addressed based on three points of comparison: *effect of vug inclusions*, at which the porous matrix without vugs and all vugular micromodels are compared (for the same porous matrix), *effect of macroporosity*, at which T_1 and T_3 micromodels are compared (for the same vug geometry), and *effect of vug geometry*, at which T_2 and T_3 micromodels are compared (for the same macroporosity).

5.1.2

Hydraulic Properties: Absolute Permeability of the porous matrix

Reliable measuring of pressure drop across the porous media in the fabricated micromodels was a matter of great importance prior to starting the fluid flow experiments. As detailed in Section 4.3, the pressure measurement points were located in the inlet and outlet distribution chambers of micromodels. Figure 5.4 shows the steady-state pressure drop (ΔP) across the porous matrix micromodel without vugs versus the flow rate of Drakeol® 7 (Q). From the slope of the best-fit straight-line along the Darcy linearity regime, the absolute permeability of the porous matrix was accurately measured to be $K_{abs} = (105.3 \pm 0.2) D$

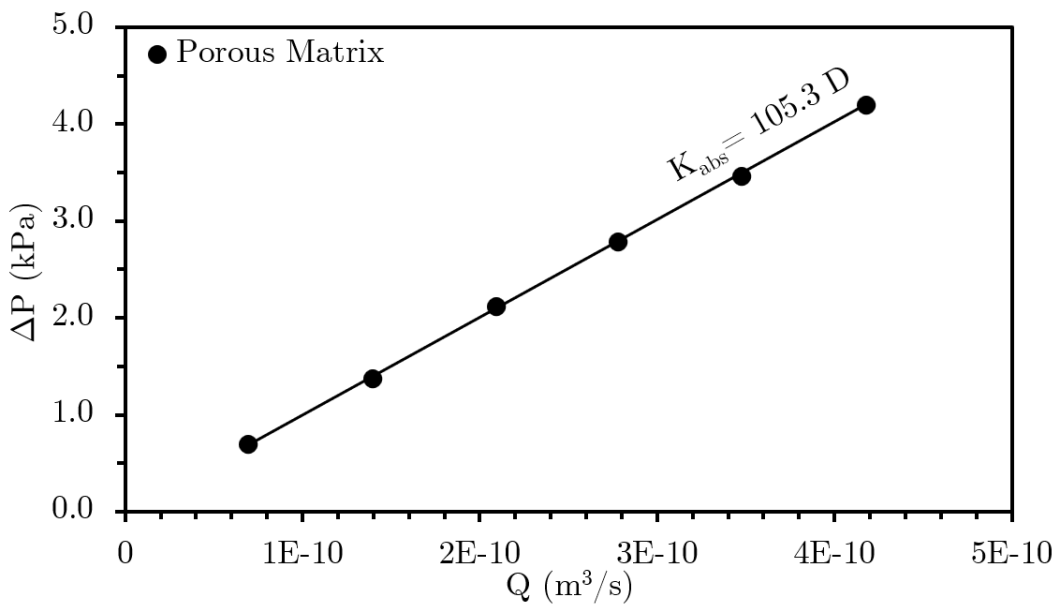


Figure 5.4: Pressure drop measurements (ΔP) against flow rate of Drakeol® 7 (Q) in the porous matrix micromodel. Calculations of absolute permeability (K_{abs}) are based on Darcy's Law, which provides K_{abs} directly from the slope.

5.1.3

Equivalent Absolute Permeability of the vugular micromodels

The equivalent absolute permeability of the three vugular porous media micromodels was determined and compared with the absolute permeability of the porous matrix. Figure 5.5 shows the steady-state pressure drop (ΔP) across the different configurations of porous media. Clearly, the inclusion of free flow regions in the porous matrix reduces the pressure drop at a fixed flow rate, which corresponds to an increase in the equivalent permeability of the *porous matrix + vugs* system.

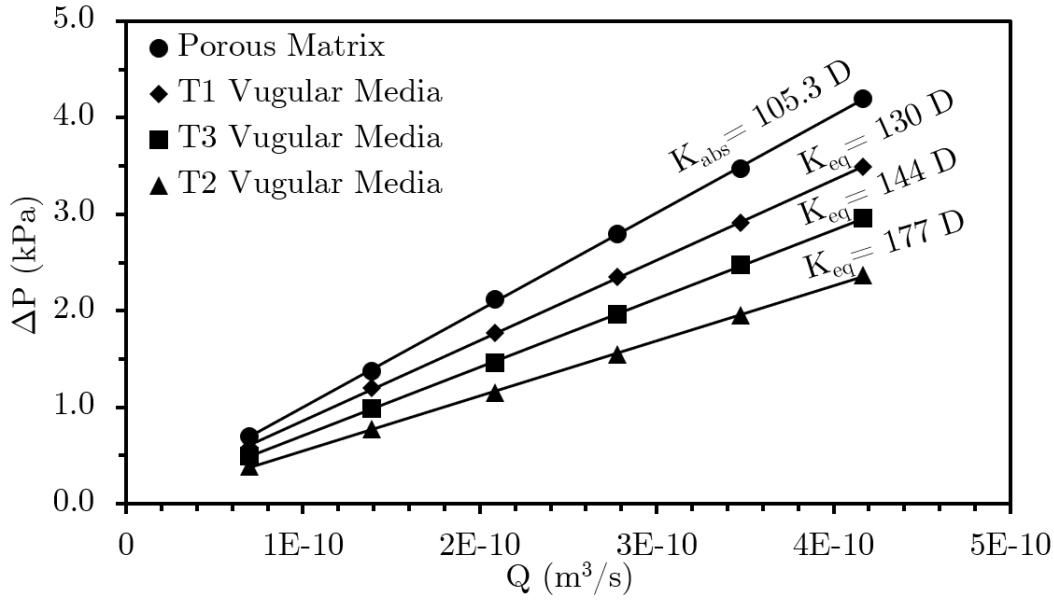


Figure 5.5: Pressure drop measurements (ΔP) against flow rate of Drakeol® 7 (Q) in the different configurations of porous media. Calculations of absolute (K_{abs}) and equivalent (K_{eq}) permeability are based on Darcy's Law, which provides K_{abs} and K_{eq} directly from the slope.

For the vugular porous media T_1 , T_2 and T_3 , the equivalent absolute permeability (K_{eq}) was measured to be (130 ± 1) D, (177 ± 1) D and (144 ± 2) D, respectively.

The inclusion of medium-long vugs ($AR = 1.7$) in the porous matrix generates an increase of $\sim 24\%$ and $\sim 37\%$ at macroporosities of 7.5% and 11.4%, respectively. When the aspect ratio of vugs is considerably higher ($AR = 6.2$), but the macroporosity of the vugular space is kept at 11.%, the increase in absolute permeability is $\sim 68\%$.

The hydraulic characterization of the vugular porous media micromodels shows that long cavities aligned in the main flow direction (thus, higher AR) and increased density of cavities with the same geometry (thus, higher macroporosity) lead to higher equivalent absolute permeability for the heterogeneous porous media. In that sense, the proposed porous matrix is sensitive to the inclusion of vugs in the sizes and distributions presented. Most importantly, the vugular design arrangement (T_1 to T_3 micromodels) reproduces the single-phase flow physics that has been widely discussed for heterogeneous porous media with small to medium isolated vugs [22, 23, 24, 61, 65].

5.2

Temporal behavior of pressure drop and fluid saturation during steady-state two-phase flow in the porous media micromodels

The next point that is explored corresponds to the steady-state simultaneous flow of water and oil through the porous media micromodels with and without vugs. In the stepwise injection experiments, steady-state values of pressure drop and fluid saturation in the porous media were gathered for relative permeability calculations. Before addressing these results, some observations on the temporal behavior of both variables are discussed.

Results from the porous matrix micromodel without vugs and from the porous matrix domain in the vugular micromodels are considered first. In Section 5.4, explanations will be extended to the vugular domain.

Figure 5.6 shows the variation of the pressure drop (ΔP) and the water saturation (S_w) in the porous matrix micromodel after 30 minutes of simultaneous flow of water and oil at 2 ml/h and $f_w = 0.5$. Pressure was recorded every 1 second and fluid saturations were measured on a 3 mm · 3mm region of the porous media every 1.7 seconds. Figure 5.7 provides live-photomicrographs of the pore space during the sampling time. The aqueous and oleic phases are marked in blue and yellow, respectively.

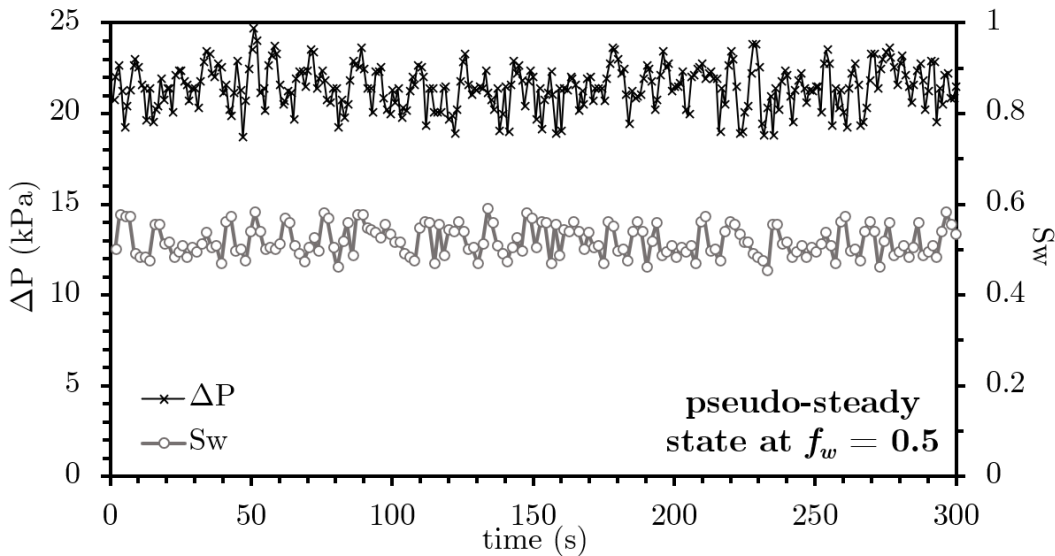


Figure 5.6: Pressure drop (ΔP) and water saturation (S_w) in the porous matrix micromodel after 30 minutes of simultaneous flow of water and oil at 2 ml/h and $f_w = 0.5$.

The pressure drop and water saturation exhibit time-dependent fluctuations around a constant time-average value. Pore-scale visualization further reveals that contrary to what would be expected, the aqueous phase does not flow through connected 2D pathways but rather as discrete fluid units of

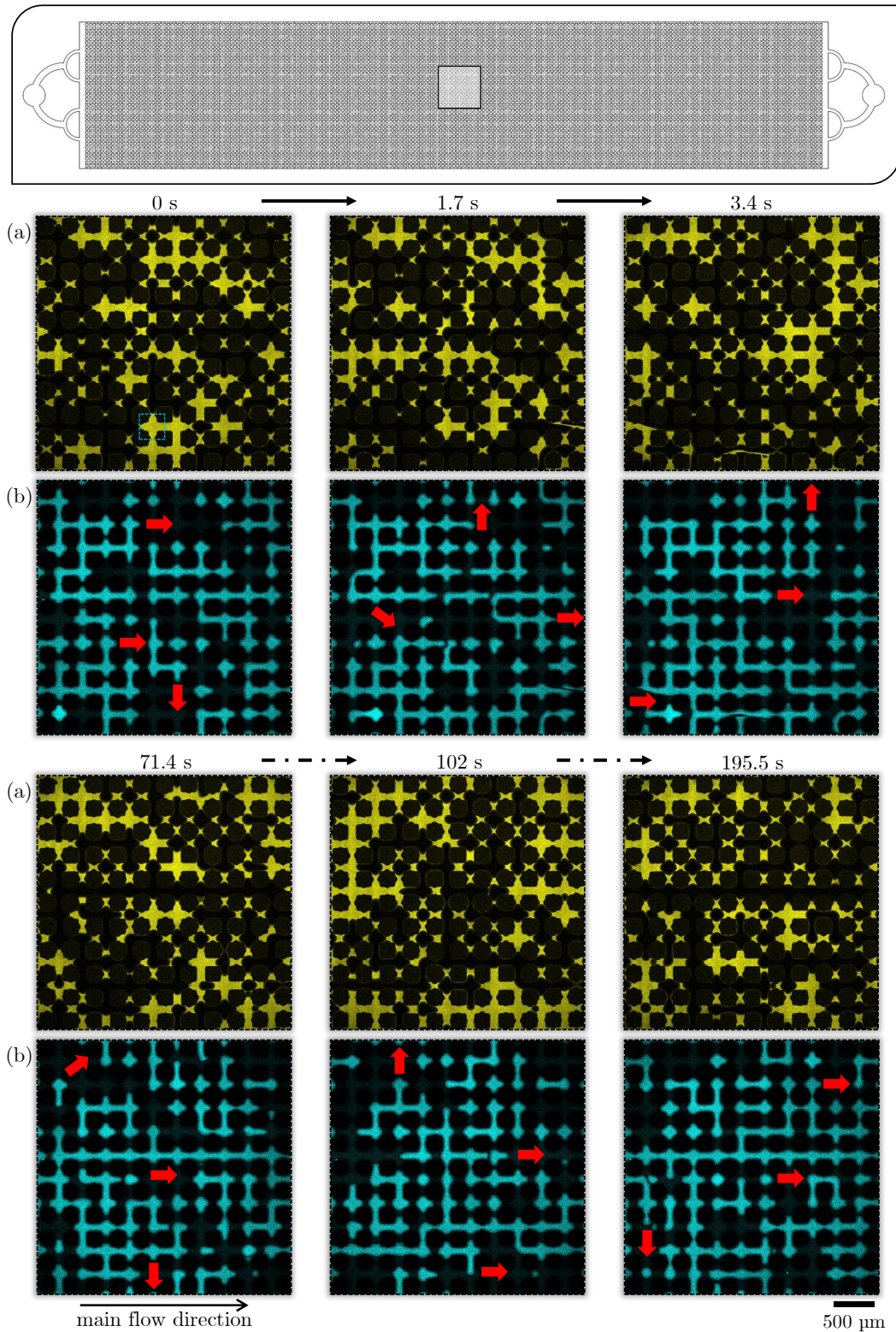


Figure 5.7: Pore-scale visualization of the oleic (a) and aqueous (b) phases when simultaneously flowing at steady state through the porous matrix micromodel. Images show multiple frames, acquired at different times, of a single tile in the middle region of the micromodel. Fractional flow of water is 0.5, main flow direction is from left to right, and the red arrows denote the movement of some of the water units. A unitary pore is indicated by a blue square.

several pores in size. These units intermittently occupy the pore space and continually coalesce (or break up) to form larger (or smaller) ones. The red arrows in Figure 5.7 denote the movement of some of them, and Movie 1 in the supplementary material¹ displays the dynamic phenomenon. It is important to remind here that the micromodel is wetted by oil.

The oleic phase, instead, flows like an ever-changing network of oil ganglia, which tend to preserve their connectivity by wetting the walls of the pore space. On this basis, the water fluid units are advected through the porous matrix by the wetting phase: being temporarily immobilized in some constricted channel entrances, eventually pushed through others, and ultimately mobilized from the porous media. Such dynamic fluid connectivity causes the relative saturation and pressure drop to vary around a constant value over a pseudo-steady state condition as shown in Figure 5.6. Similar observations were obtained in the porous matrix domain of the vugular micromodels.

It should be noted that although the *temporal fluid saturation* was quantified from a individual tile (exclusively for this analysis), it was also monitored at 25 random positions throughout the porous matrix. One-tile measurements were confirmed to be representative of the entire porous medium.

The fluid flow behavior previously described is consistent with novel observations on intermittent pore occupancy by the non-wetting phase during steady-state co-flow of two immiscible phases reported in core flooding experiments [62, 63, 53, 72, 54]. This phenomenon has been suggested to be a consequence of increasing the energy of the non-wetting phase injected into the system, which allows it to occupy the pores intermittently. Furthermore, it has been suggested that it is controlled by the competition between the viscous forces exerted on the flowing non-wetting phase and the capillary forces at the pore scale [63, 73].

Further studies performed on the porous matrix micromodel indicate that the intermittent pore occupancy of the aqueous phase is maintained even at total water-oil flow rates of 1 and 4 ml/h. The latter in capillary number (Ca) based on the total flow rate and the viscosity of the aqueous phase, ranges from $2 \cdot 10^{-5}$ to $7 \cdot 10^{-5}$. These values are within the interval reported by Gao et al. [54] for intermittent flow of brine and pentane at $f_w = 0.5$ in a homogeneous sandstone sample. Moreover, our observations reveal that for all fractional flows of water investigated between 0.1 and 0.9, the steady-state pore occupancy of the aqueous phase throughout the porous matrix of micromodels is intermittent.

¹Supplementary material: <https://youtube.com/shorts/tc8MeLmvrvc>

Contrarily, *at the endpoint of the stepwise injection*, in which only the aqueous phase is injected into the porous media ($f_w = 1$), we noted that the steady-state flow regime of this phase becomes non-intermittent. Figure 5.8 shows the transition behavior of the pressure drop (ΔP) and the water saturation (S_w) in the porous matrix when the fractional flow of water is changed from 0.9 (in the pseudo-steady state) to 1.

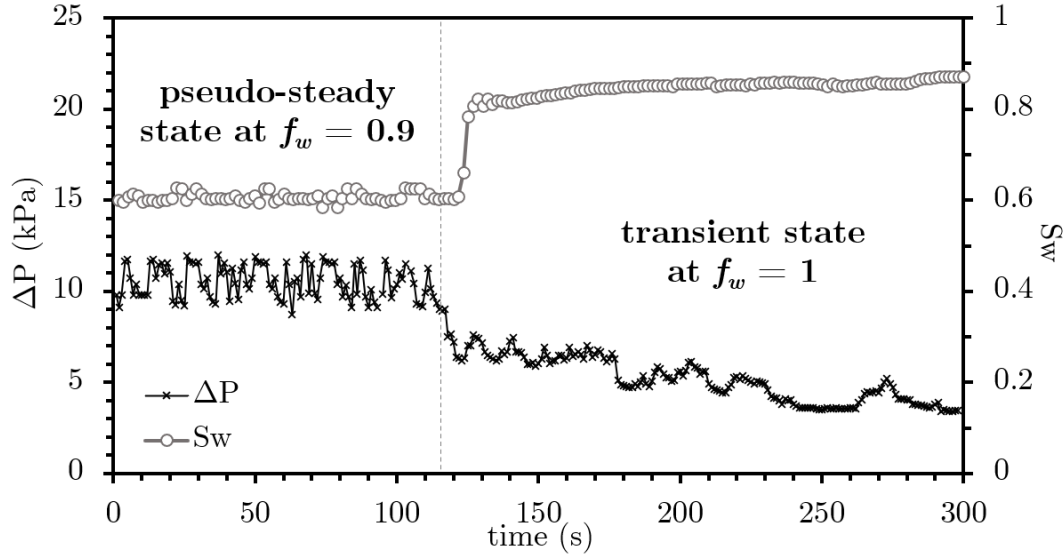


Figure 5.8: Transition of the pressure drop (ΔP) and water saturation (S_w) in the porous matrix micromodel when the fractional flow of water is changed from 0.9 to 1, at total flow rate of 2 ml/h.

The exclusive invasion of water into the porous matrix leads to a long transient state, in which the pressure drop first decreases rapidly and then goes through a long period of fluctuating slow decrease. Initially, continuous water flow pathways are created through the porous medium, breaking up oil islands and advecting fractional oil units toward the outlet. After that, the remaining oil units wetting the pore space walls are continuously reduced to smaller ones, ending up in some regions as pendular rings. Live-photomicrographs of the pore space in Figure 5.9 support these observations and Movie 2 in the supplementary material² displays the dynamic phenomenon.

Once the residual oil saturation is reached in the pore space, which implies that the oil ganglia are immobile, the pressure drop (ΔP) and the water saturation (S_w) remain stable at a single value. Figure 5.10 shows the temporal variation of both variables after 60 minutes of water injection. The non-time dependent behavior is a consequence of the continuous flow of water through unchanging pathways across the porous media micromodel.

²Supplementary material: <https://youtu.be/CFWGMCEZ-c>

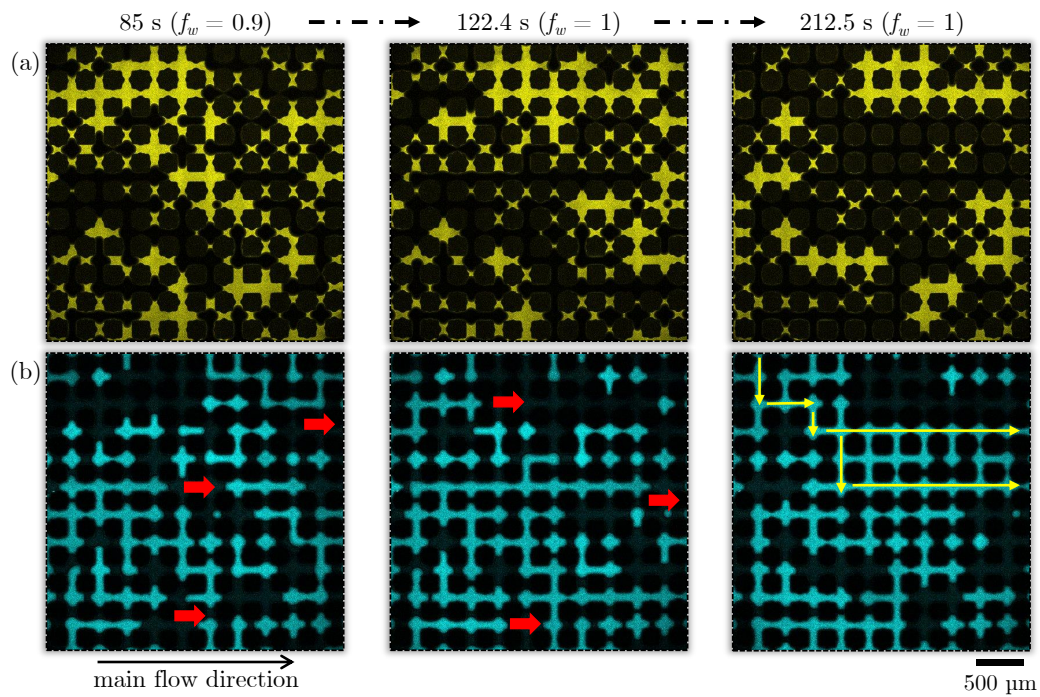


Figure 5.9: Pore-scale visualization of the oleic (a) and aqueous (b) phases in the porous matrix micromodel when the fractional flow of water is changed from 0.9 to 1. Main flow direction is from left to right. The red arrows denote the movement of some of the water units and the yellow arrows denote the flow of water through unchanging pathways.

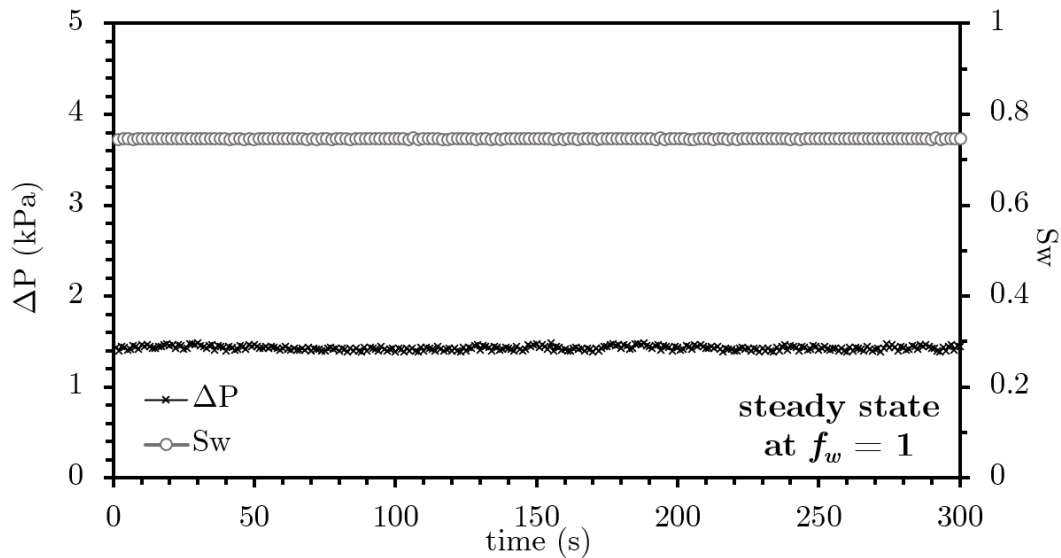


Figure 5.10: Pressure drop (ΔP) and water saturation (S_w) in the porous matrix micromodel after 60 minutes of flow of water at 2 ml/h ($f_w = 1$).

Figure 5.11 presents live-photomicrographs of the pore space at the steady-state condition at $f_w = 1$.

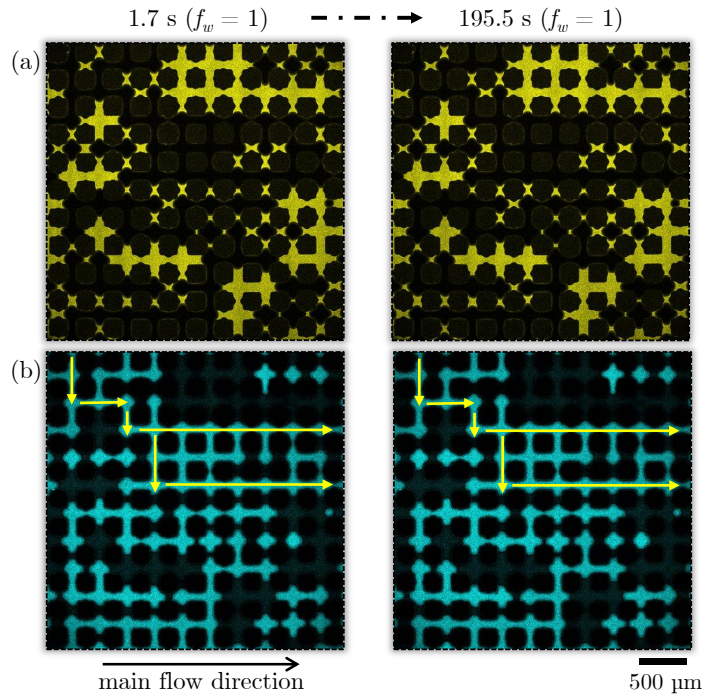


Figure 5.11: Pore-scale visualization of the oleic (a) and aqueous (b) phases in the porous matrix micromodel after 60 minutes of flow of water at 2 ml/h ($f_w = 1$). Main flow direction is from left to right. The yellow arrows denote the flow of water through unchanging pathways.

The identification of the fluid flow behaviors described above suggests a good scaled representation of a porous medium with the micromodels. In particular, we highlight the replication of phenomena that derive from the competition between viscous and capillary forces at the pore scale.

As a final comment on this section, it is remarkable that all values of pressure drop and fluid saturations that will be reported from now on correspond to time-average values at (pseudo-) steady state. In all cases excellent reproducibility was found in duplicates.

5.3

Accounting for oil saturation in the porous media micromodels

The time-average values of fluid saturation inside the porous media micromodels were examined as a function of the fractional flow of water (f_w). Accounting for oil saturation was conducted first.

Figure 5.12 compares the average oil saturation (S_o) in the porous matrix micromodel to that in the whole porous medium of T_1 to T_3 vugular micromodels. As expected, in all cases, oil saturation falls as the water frac-

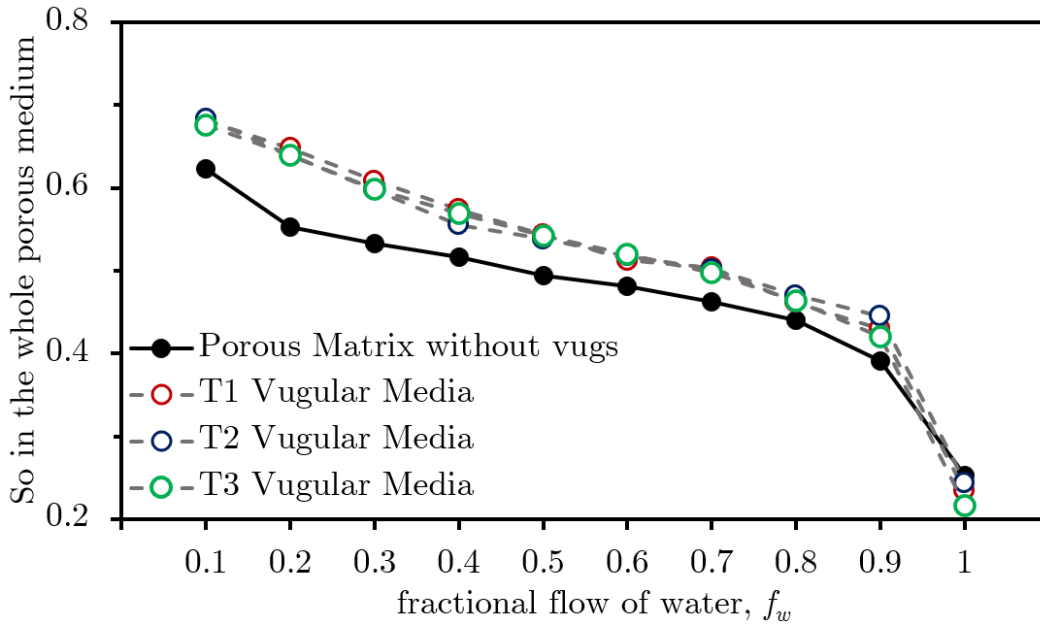


Figure 5.12: Oil saturation (S_o) in the porous matrix micromodel and in the whole porous medium of T_1 to T_3 vugular micromodels as a function of the fractional flow of water.

tional flow rises. For $0.1 \leq f_w \leq 0.9$, the oil saturation in the porous media with vugs is found to be higher than in the porous matrix without vugs. It is observed, however, that this increase in saturation becomes less important as the proportion of flowing water increases. In fact, when only water is injected ($f_w = 1$), the total oil saturation in the vugular porous media is lower. This apparently contradictory result of higher oil recoveries in vugular media will be clarified later.

Visual observations within the pore space of micromodels allow us to identify preliminary fluid flow behavior. Figure 5.13 shows live-photomicrographs of the pseudo steady-state water/oil distributions in the porous matrix without vugs and in the vugular porous media T_1 to T_3 at $f_w = 0.3$. These pictures correspond to 2D grid stitchings formed by 40 live-image tiles acquired from the middle region of micromodels.

Most importantly, (i) the originally oil-saturated vugs are now partially and non-uniformly saturated with water, and (ii) the porous matrix of the vugular media seems to have higher oil saturation than the porous matrix without vugs. These observations are consistent with those reported in relation to non-uniform distributions of water and oil in heterogeneous media [13, 14, 21]. In addition, they bring the need to evaluate the fluid saturations separately for each porosity domain, that is, for the porous matrix and for the vugs.

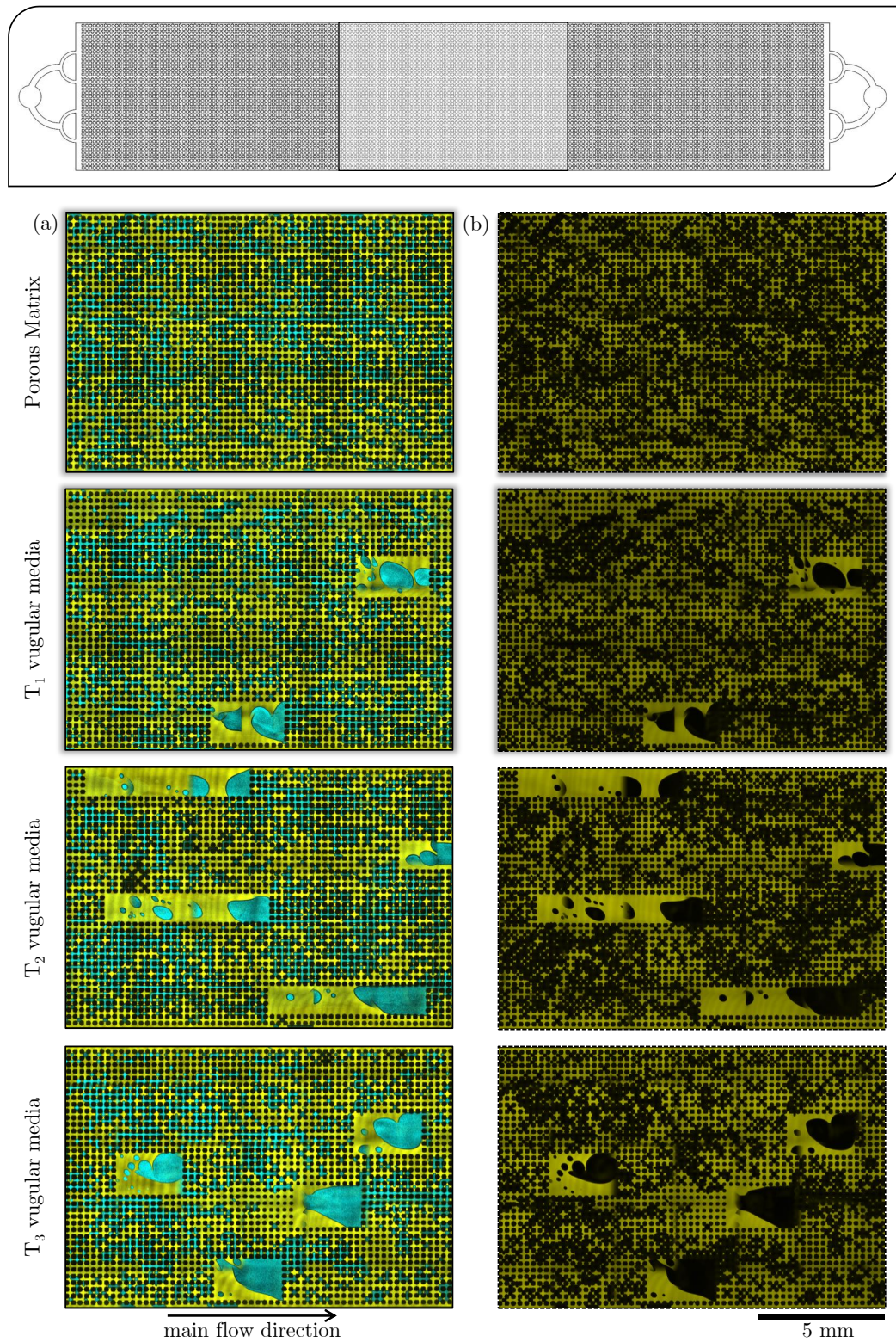


Figure 5.13: Pore-scale visualization of the aqueous and oleic phases (a) when simultaneously flowing at steady state through the porous media micromodels. The oleic phase is detected exclusively in (b). Fractional flow of water is 0.3 and the main flow direction is from left to right. All images are formed by 40 live-image tiles acquired from the middle region of micromodels.

The average oil saturation exclusively inside the porous matrix of all micromodels is presented in Figure 5.14. It is confirmed that the oil saturation in the porous matrix of the micromodels with vugs is higher than that in the porous matrix of the micromodel without vugs. It is also confirmed that these increases are higher than the uncertainty in the saturation measurement ($< 2\%$) for all fractional flows of water between 0.1 and 0.9. We can affirm that the distribution of fluids in the heterogeneous porous media is altered by the presence of the vugs in such a way that the oil occupancy in the porous matrix remains greater. Even at $f_w = 1$ in the T_2 vugular media, the endpoint is consistent with the lower oil displacement efficiencies by water injection reported for heterogeneous media [13, 15, 27].

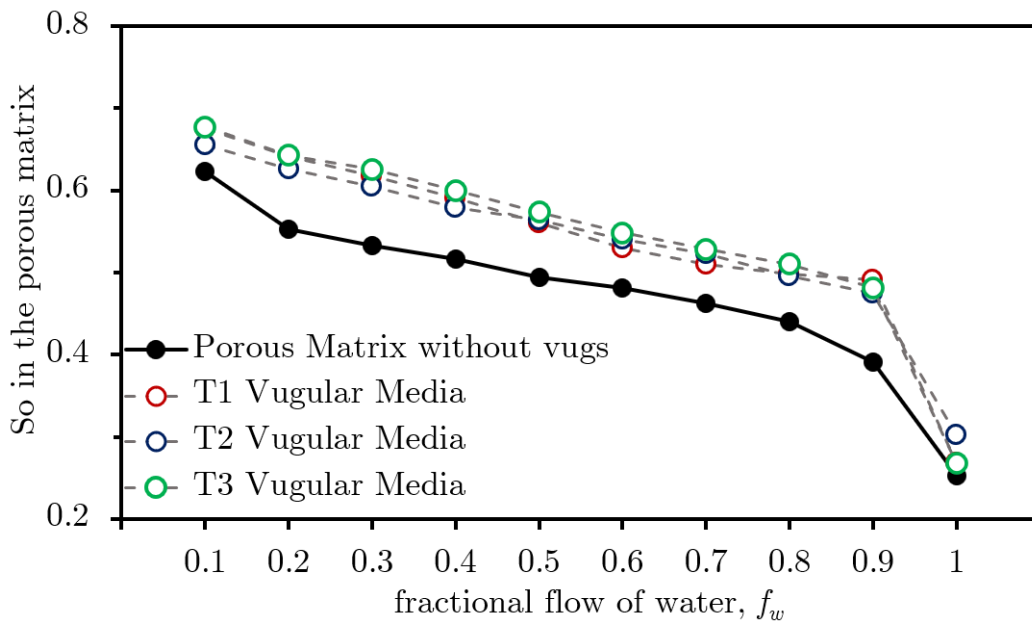


Figure 5.14: Oil saturation (S_o) in the porous matrix micromodel and in the porous matrix domain of T_1 to T_3 vugular micromodels as a function of f_w .

Quantitative comparisons of the oil saturation in the porous matrix of the different configurations of vugular media (T_1 to T_3) does not provide clear evidence regarding the effect of macroporosity (when comparing T_1 with T_3) or vug geometry (when comparing T_2 to T_3). However, it can be stated that 7.5% macroporosity based on non-touching and non-elongated vugs is sufficient to increase the oil saturation in the porous matrix by up to 25%.

Further examination of the average oil saturation in the porous media micromodels is addressed in Figure 5.15. The 45-degree line corresponds to the porous matrix without vugs, in which both the oil saturation in the porous matrix and in the whole porous medium are identical. The other locus correspond to the vugular porous media micromodels, for which some observations can be highlight.

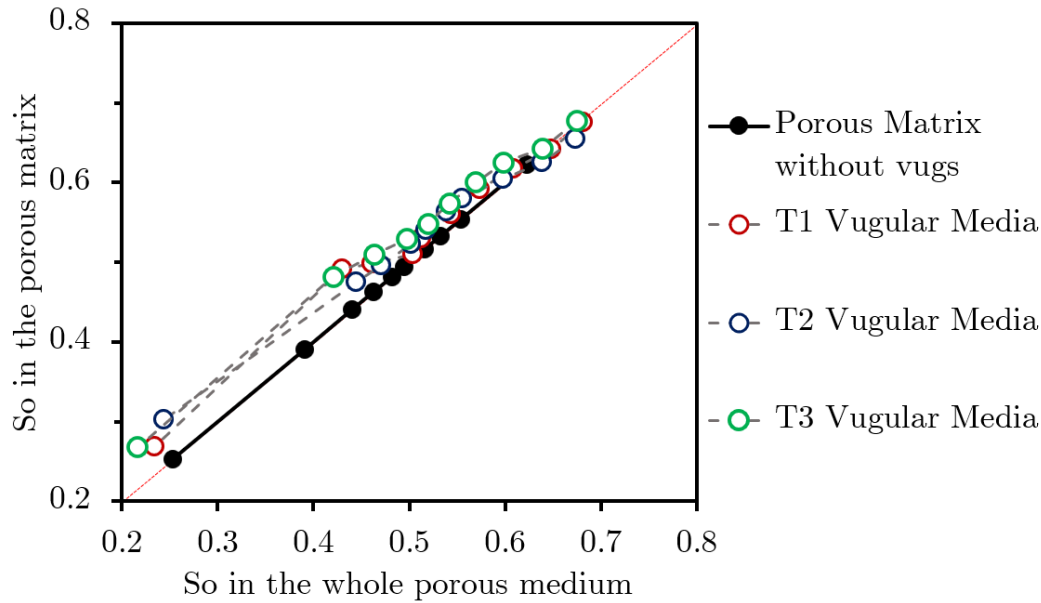


Figure 5.15: Oil saturation in the porous matrix versus oil saturation in the whole porous medium of micromodels.

At $S_o > 0.6$ (or $f_w < 0.3$), there are no large differences between the saturation of the whole porous medium and the saturation of the porous matrix domain. The oil initially stored in the vugs contributes to increasing the total oil saturation compared to that of the porous matrix without vugs. Then, when $S_o < 0.5$ (or $f_w > 0.7$), the divergence between oil saturation exclusively in the porous matrix of the vugular media and the whole porous medium becomes sharper. This suggests that as the water saturation in the whole porous medium increases, vugs and porous matrix are not occupied/drained in the same proportion. The next subsection further discuss this phenomenon.

5.4

Accounting for water saturation in the porous matrix and vug domains of porous media micromodels

The previous observations about the higher oil saturations in the porous matrix of the vugular porous media allow us to intuit that, in terms of fluid distribution, there is a competition for the preferential flow of the aqueous phase between the porous matrix and the vugular space.

Figures 5.16 to 5.18 show live-photomicrographs of the water distributions in the vugular micromodels T_1 to T_3 at different fractional flows of water (f_w). Each picture corresponds to a 2D grid stitching formed by 25 live-image tiles acquired at the steady state of the referred value of f_w . Movies 3 and 4 in the supplementary material³ display the vug-scale flow dynamics.

³Supplementary material: <https://youtube.com/shorts/Trnr1LuwKuI> and <https://youtube.com/shorts/lM8oGVDaFzg>

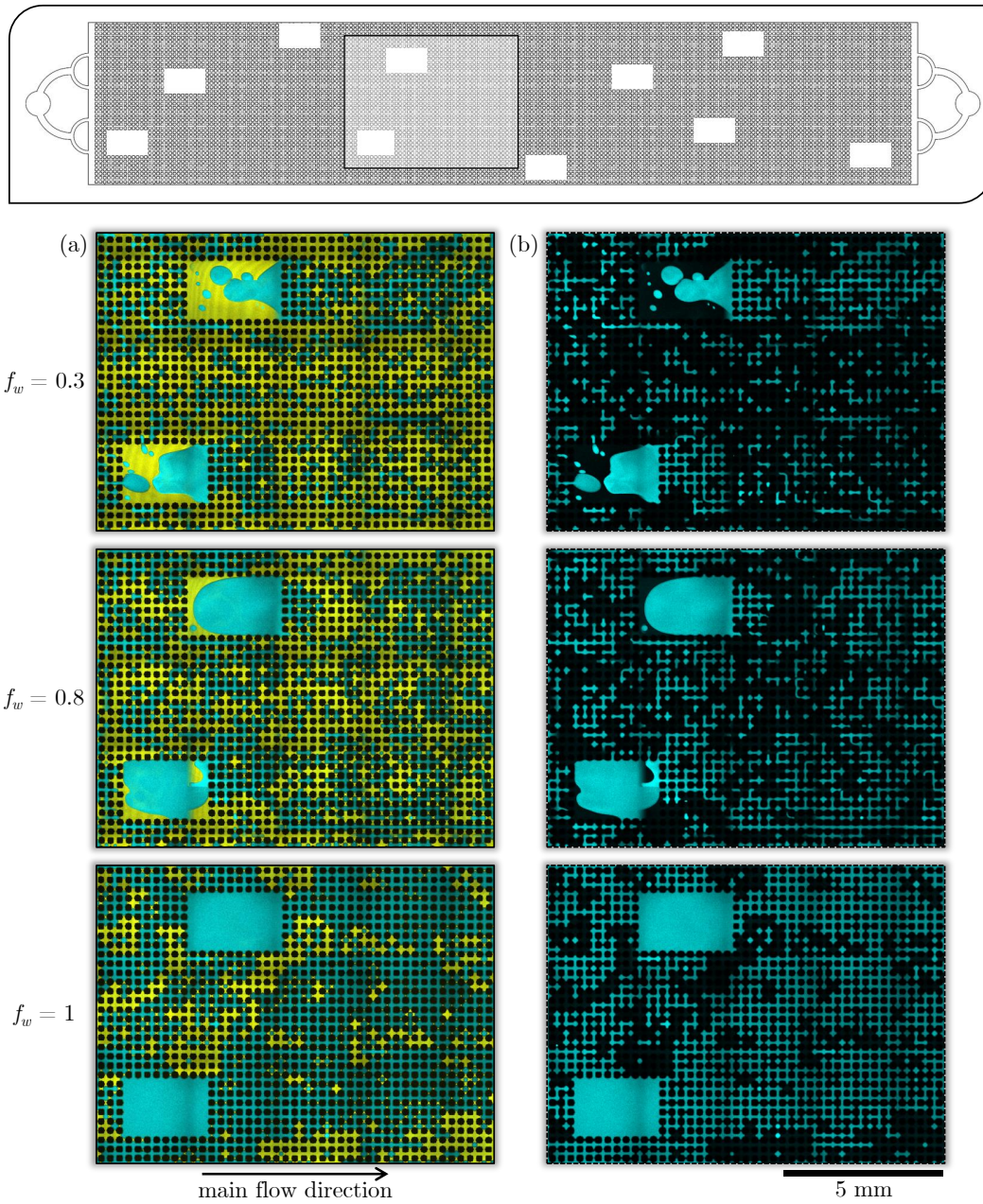


Figure 5.16: Vug-scale visualization of the aqueous and oleic phases (a) when simultaneously flowing at steady state through the vugular porous media micromodel T_1 . The aqueous phase is detected exclusively in (b). Fractional flows of water are 0.3, 0.8 and 1, and the main flow direction is from left to right. All images are formed by 25 live-image tiles acquired from the middle region of micromodels.

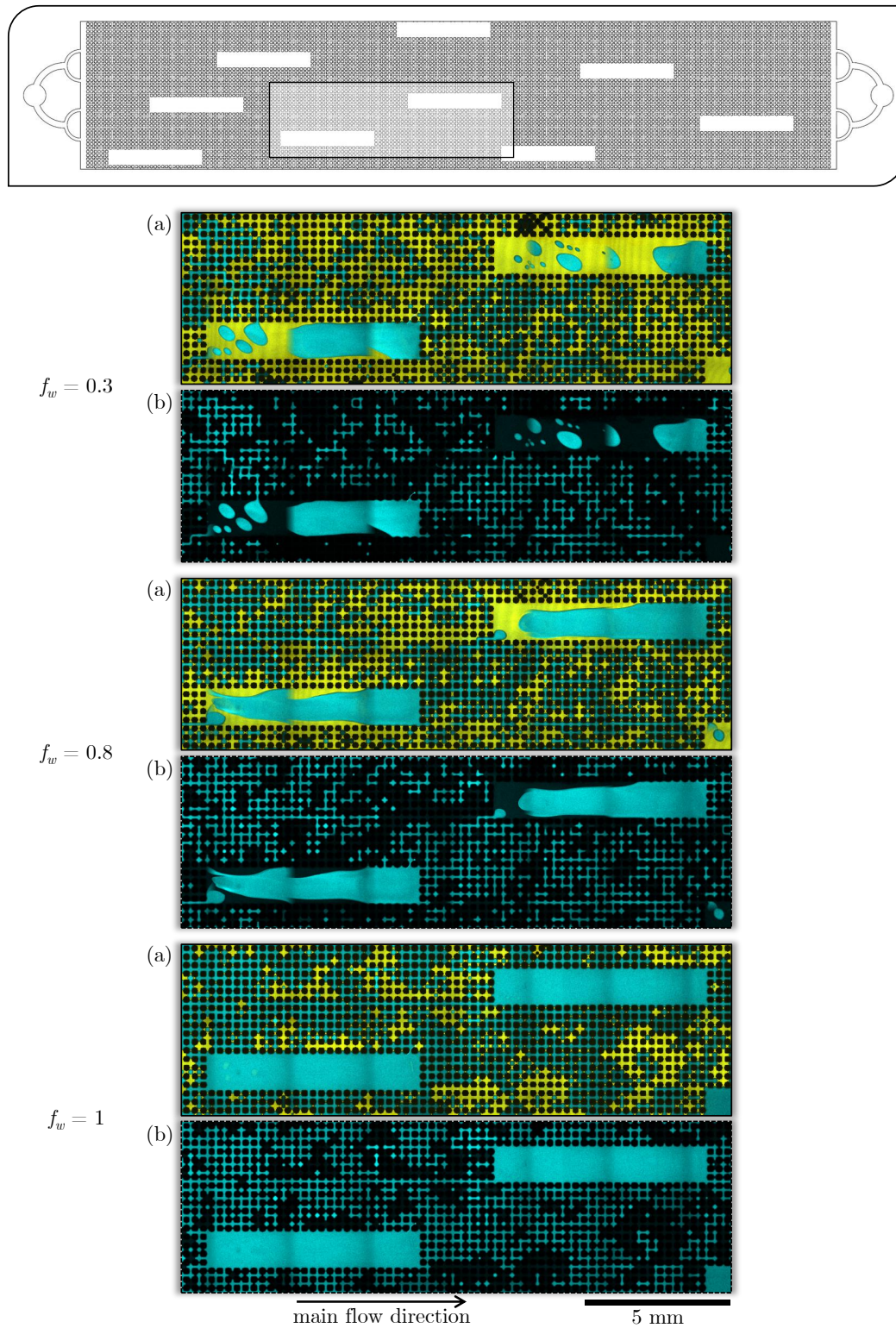


Figure 5.17: Vug-scale visualization of the aqueous and oleic phases (a) when simultaneously flowing at steady state through the vugular porous media micromodel T_2 . The aqueous phase is detected exclusively in (b). Fractional flows of water are 0.3, 0.8 and 1, and the main flow direction is from left to right. All images are formed by 25 live-image tiles acquired from the middle region of micromodels.

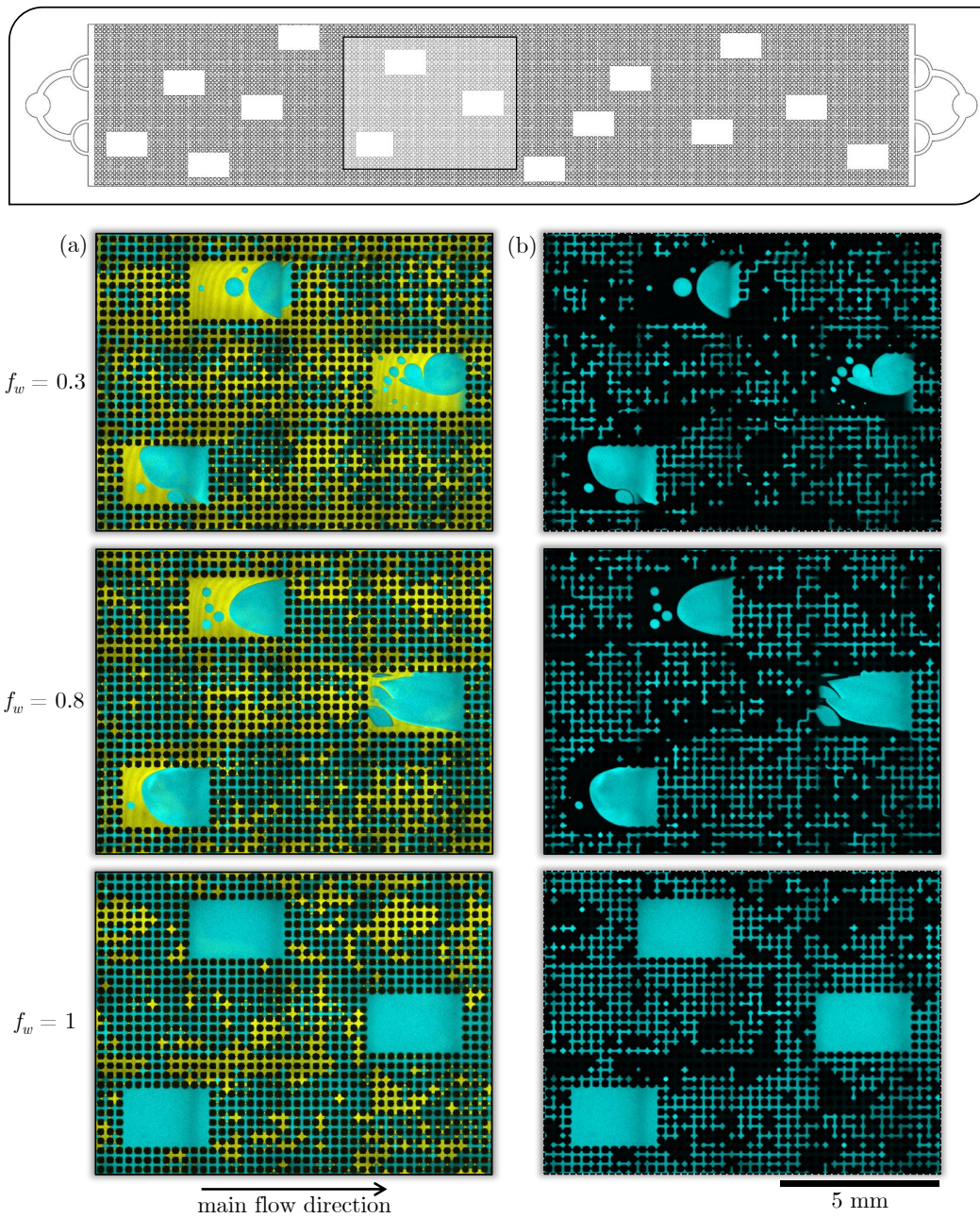


Figure 5.18: Vug-scale visualization of the aqueous and oleic phases (a) when simultaneously flowing at steady state through the vugular porous media micromodel T_3 . The aqueous phase is detected exclusively in (b). Fractional flows of water are 0.3, 0.8 and 1, and the main flow direction is from left to right. All images are formed by 25 live-image tiles acquired from the middle region of micromodels.

In our model of vugular porous media, vugs are embedded in the porous matrix and are not connected to each other, so they can only be accessed through the porous matrix/vug interface. The vug occupancy by the fluids follows the way in which they move through the porous matrix, that is, in an intermittent flow regime for the aqueous phase and by wetting the walls for the oleic phase.

The vug-scale visualization shows that during the steady-state two-phase flow, the vug domain is occupied partially and intermittently by flowing water units; and, as the porous matrix is drained by larger fractional flows of water, the oil in the vug space also decreases. In detail, it is observed that part of the water units flowing through the porous matrix converge towards the front side of the vugs and, depending on their frequency, coalesce inside them to form larger units. These volumes of water flow across the oil-flooded cavities and ultimately leave them from their back side.

The absence of single fluid fronts makes it difficult to identify preferential 2D pathways in the porous matrix that could result from the presence of vugs. Even so, at high values of f_w , continuous and connected flow pathways for the aqueous phase are identified in some regions of the porous matrix between neighboring vugs. Figures 5.17 and 5.18 evince some of these flow pathways in the vugular porous media at $f_w \geq 0.8$.

On a quantitative basis, Figure 5.19 presents the water saturation profiles in the vug domain as a function of the water saturation in the porous matrix domain for vugular micromodels T_1 to T_3 . The results are conveniently coupled as (a) T_1 - T_3 micromodels, which have the same vug geometry and different macroporosity, and (b) T_2 - T_3 , which have the same macroporosity and different aspect ratio.

First, when comparing the profiles against a 45-degree line, it is noticeable that the average water occupancy in vugs increases faster than the average water occupancy in the porous matrix for all the configurations of vugular media. However, vugs do not become 100% saturated with water until the porous media is exclusively invaded by water - i.e. $f_w = 1$.

Then, when comparing the individual profiles, it is revealed that the water saturation level in the vugular space is not very sensitive to increases in macroporosity, but moderately sensitive to changes in the vug geometry. In micromodels T_1 and T_3 , the change in macroporosity is due to an increase in the number of cavities distributed throughout the whole porous medium (10 vugs to 15 vugs), which subtly favors their saturation with water. In micromodels T_2 and T_3 , instead, even though the total macroporosity is the same, it is observed

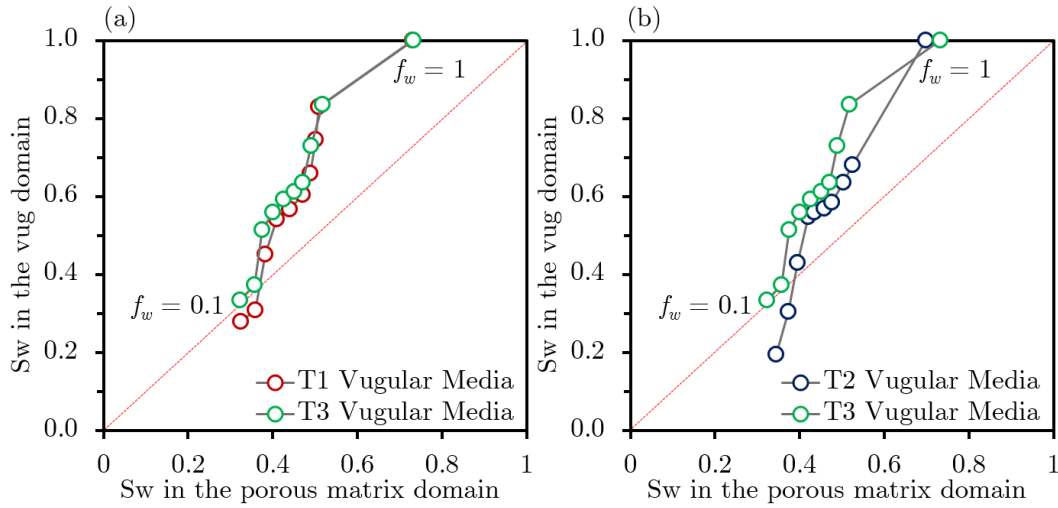


Figure 5.19: Water saturation in the vug domain versus water saturation in the porous matrix domain of vugular micromodels T_1 to T_3 . (a) T_1 - T_3 have the same vug geometry and different macroporosity, and (b) T_2 - T_3 have the same macroporosity and different aspect ratio.

that for $f_w < 1$ the more elongated vugs ($AR = 6.2$) are less saturated with water than the other ones ($AR = 1.7$).

This behavior can be explained in terms of the number of channels surrounding the individual vugs. Cavities in the micromodel T_2 have 5 front channels \cdot 26 lateral channels, while those in the micromodels T_1 and T_3 have 7 front channels \cdot 11 lateral channels. For longer cavities (more lateral channels), a significant part of the elongated vug-porous matrix interface does not contribute to the entry of water into the vug. Moreover, for larger cavities (more lateral and front channels), more water is required up to 100% saturation.

The reported changes in the water distribution of the vugular porous media micromodels suggest that the invasion of the aqueous phase into the porous matrix domain is less efficient than the one into a porous media without vugs. In section 5.3, it was shown that the oil saturation in the porous matrix of vugular porous media is higher, which supports our hypothesis. In the next section, the morphology of the oil units that occupy the porous matrix is analyzed, and compared to that of the porous matrix without vugs.

5.5

Morphological details of the oleic phase distribution in the porous matrix of micromodels with and without vugs

Images of the porous media were also used to determine the morphology (size distribution) of the oil occupying the pore space of micromodels during the steady-state simultaneous flow of water and oil. The size of the fluid units is presented in units of a unitary pore (UP), which is defined as the average area of a single pore and half of the four channels connected to it. In Figure 5.7, a unitary pore is indicated by a blue square.

The accumulated oil saturation in the porous matrix of the micromodel without vugs and in that of the vugular micromodel T_2 is presented in Figure 5.20 as a function of the relative size of oil units. In general, it is found that as the fractional flow of water increases, the contribution of smaller oil units on the average oil saturation becomes more representative at the expense of a decrease in the contribution of larger oil units. The decrease in the average oil saturation in the porous matrix as f_w increases is related not only to oil drainage, but also to the reduction in the size of the oil units distributed throughout the pore space.

This tendency, however, is weaker in the vugular porous media, where larger units of oil remain in the porous matrix over the entire range of f_w . For example, at $f_w = 0.5$, the oil saturation in the porous matrix of the vugular media is still associated with large oil units (> 1000 UP), unlike the porous matrix without vugs in which the larger units have already been reduced to medium ones (< 500 UP).

The presence of vugs in the porous media micromodels affects the two-phase flow in such a way that invasion of the aqueous phase into the porous matrix domain becomes less efficient. The convergence and transport of large volumes of water through the vugs prevents the drainage of some of the oil ganglia that occupy the porous matrix, leaving behind less efficiently drained regions, especially those lateral to the position of the vugs and those that are not aligned between neighboring vugs. The higher oil saturations for the porous matrix domain of the vugular micromodels are a consequence of these larger fluid units. All vugular porous media configurations studied exhibited similar results.

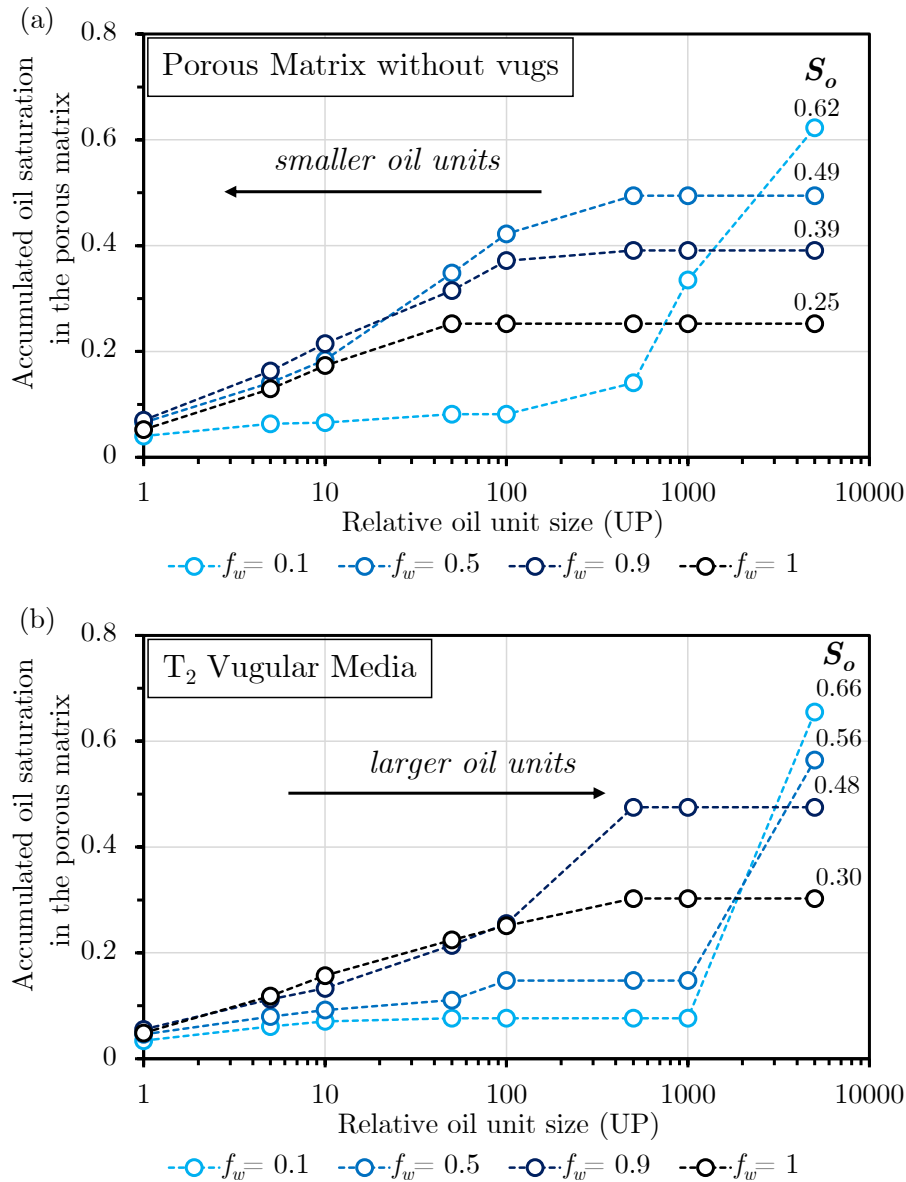


Figure 5.20: Distribution of the oleic phase in the (a) porous matrix without vugs and in the (b) porous matrix of T_2 vugular media as a function of the oil unit size (in unitary pore units, UP).

5.6

Sensitivity of two-phase flow pressure drop to the inclusion of vugs in the porous media micromodels

The steady-state pressure drop during the flow of water and oil in the porous media micromodels (ΔP) is shown in Figure 5.21 as a function of the water saturation in the whole porous medium (S_w). Similar to the single-phase flow behavior explained in Section 4.1, the inclusion of vugs in the porous matrix reduces the pressure drop across the whole porous medium. The highest sensitivity is found at higher macroporosity, when comparing devices T_3 with T_1 , and at higher vug aspect ratio, when comparing devices T_2 with T_3 .

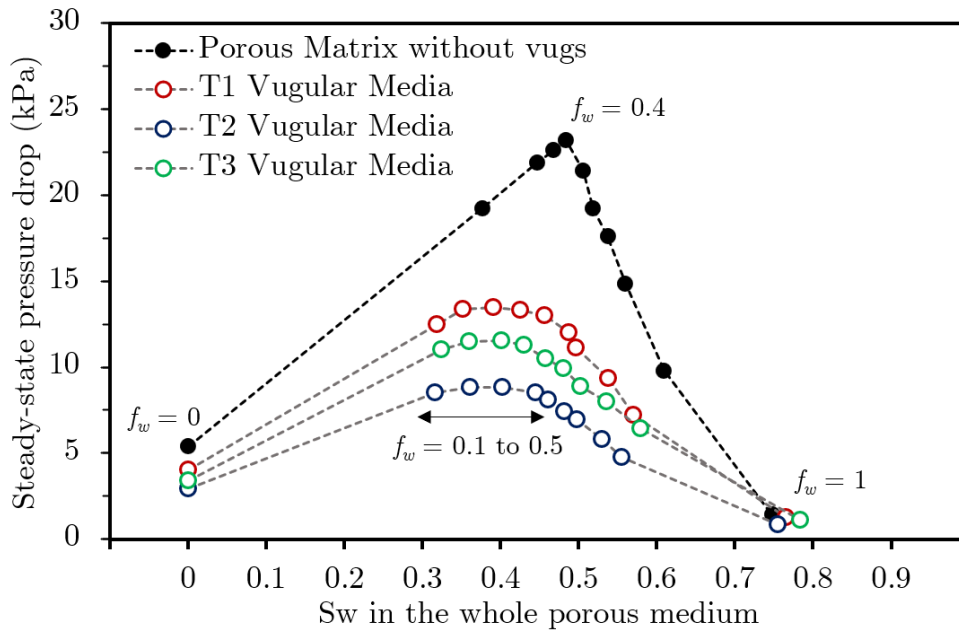


Figure 5.21: Steady-state pressure drop during the flow of water and oil in the porous media micromodels as a function of the water saturation (S_w) in the whole porous medium.

The trend followed by the pressure drop variation with water saturation reveals some additional characteristics of the fluid flow behavior at the pore scale. First of all, it is remarkable the strong growth in pressure drop through the porous matrix micromodel without vugs as the fractional flow of water (f_w) increases from 0.1 up to 0.4. Both the reduction of the pore space available for the flow of the wetting phase (oil) and raising of capillary resistance to the flow of the non-wetting phase (water), may justify this increase in the macroscopic resistance to the simultaneous flow of water and oil across the porous matrix.

In the vugular porous media micromodels, instead, the initial trend of the pressure drop profile (i.e., at $0.1 < f_w < 0.5$) does not exhibit strong increases, rather becomes almost independent of the fractional flow of water. The entire porous medium is provided, in this case, with regions of lower resistance to flow, in which large volumes of water are transported. Accordingly, the water saturation in the porous matrix domain is little increased and, therefore, the macroscopic resistance to the simultaneous flow of water and oil remains almost unchanged.

Next, when the fractional flow of water rises from 0.5 to 1, the steady-state pressure drop decreases in both the porous matrix without vugs and the vugular porous media. Such a decrease occurs as a consequence of lower viscous resistance to the flow of an increasingly water-rich stream and lower oil saturation in the porous medium (which increases the effective porosity for the flowing aqueous phase).

A further analysis in this section is based on the temporal behavior of pressure drop after switching the fractional flow of water from 0.9 to 1. Figure 5.22 contrasts the dynamics of the pressure drop across the porous matrix without vugs (already presented in Figure 5.8) with that of the vugular porous media T_1 to T_3 . In this case, ΔP is plotted in terms of pore volumes (PV) of injected aqueous phase.

In general, the presence of vugs in the porous matrix reduces the volume of injected water needed for the pressure drop to become stable. In the vugular media, after 2 PV , fluctuations are significantly reduced, while in the porous matrix without vugs at least 6 PV are necessary. This period of slow and fluctuating decline in pressure drop was previously associated with drainage and reduction of oil units by water flooding in the oil-wet porous media. Observations on faster drainage kinetics at $f_w = 1$ support the higher remaining oil saturations found in the vugular porous media micromodels.

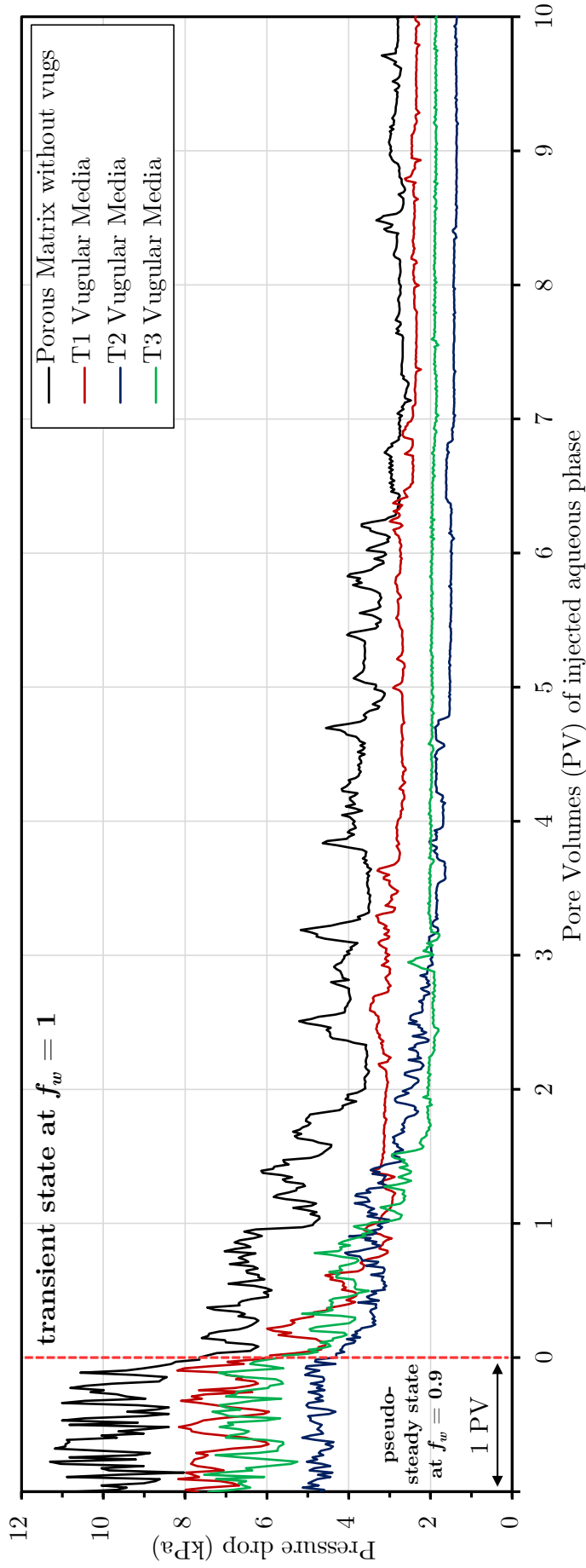


Figure 5.22: Transition of the pressure drop across the porous media micromodels when the fractional flow of water is changed from 0.9 to 1, at total flow rate of 2 ml/h.

5.7

Sensitivity of steady-state relative permeability to the inclusion of vugs in the porous media micromodels

The pseudo-steady state measurements of pressure drop and fluid saturations were used to construct relative permeability curves. Figure 5.23a compares the relative permeability to water ($K_{r,w}$) and to oil ($K_{r,o}$) in the porous matrix micromodel without vugs to that in the vugular porous media micromodels T_1 to T_3 . Figure 5.23b presents the relative permeability values on a logarithmic scale.

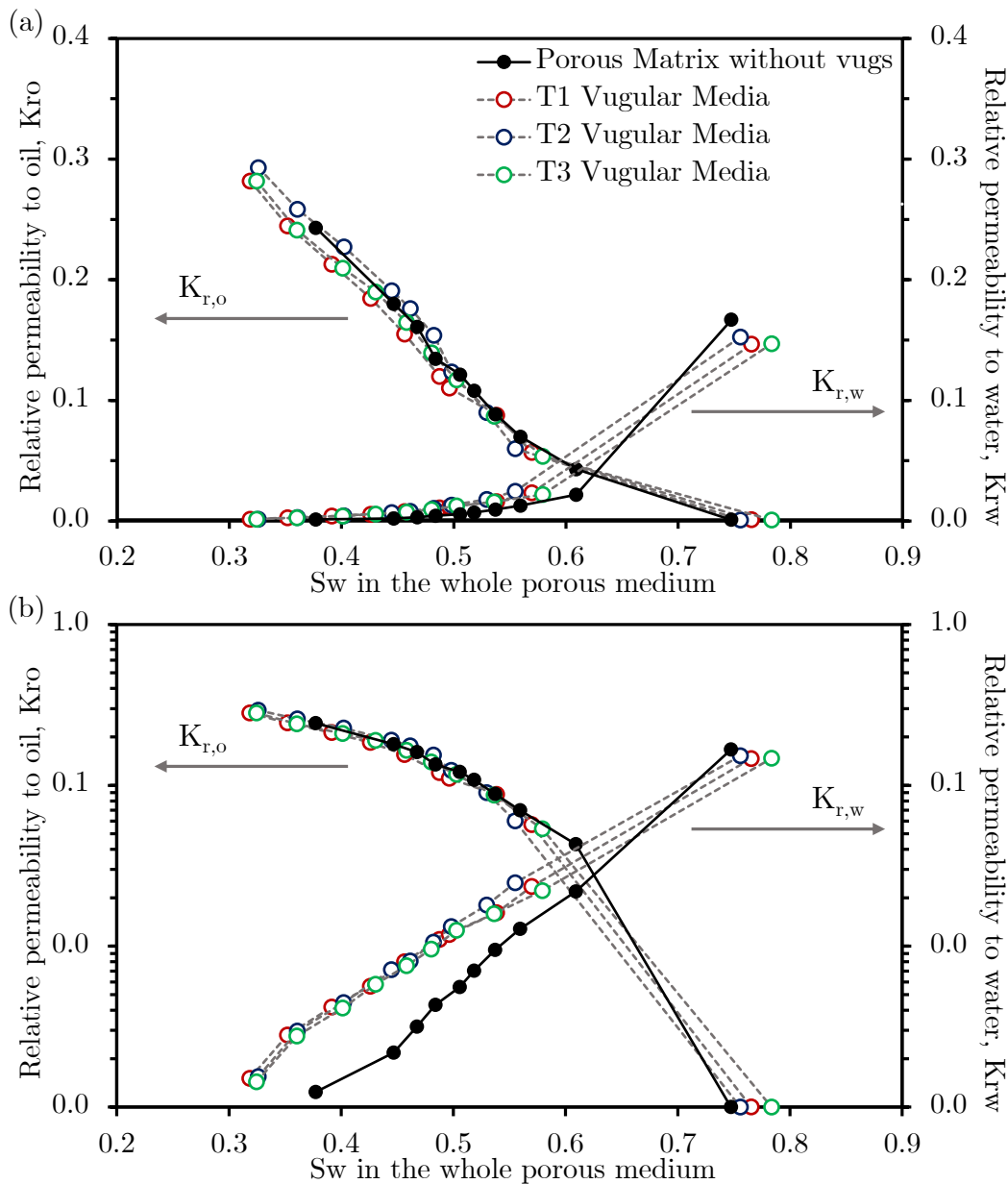


Figure 5.23: Relative permeability to the aqueous ($K_{r,w}$) and to the oleic ($K_{r,o}$) phases in the porous matrix without vugs and in the vugular porous media micromodels as a function of water saturation (Sw). $K_{r,w}$ and $K_{r,o}$ are represented on (a) linear and (b) logarithmic scale.

The average water saturation (S_w) in the entire porous medium was considered as the only argument to project the K_r - curves. In that sense, comparisons for the same S_w are subject to differences in the distribution of fluids throughout the porous space. As previously observed, in vugular media, oil retention in the porous matrix domain is higher and water transport through the vug domain is favored. In terms of relative permeability, it is seen that the oil relative permeability curves are quite similar to that of the porous matrix without vugs, while the water relative permeability curves exhibit a different behavior. During simultaneous flow of water and oil, $K_{r,w}$ is higher in the vugular media. Conversely, at the endpoint when only water flows, $K_{r,w}$ becomes moderately higher in the porous matrix without vugs.

One possible physical mechanism that explains the observed changes in the relative permeability curves is based on the capillary resistance that each porosity domain offers to the flow of the wetting and non-wetting phases. The porous media micromodels are strongly oil-wet. Consequently, it is expected that the oil displacement through the porous matrix domain is favored by capillary forces. In the vugular micromodels, however, the aqueous phase is also expected to flow more easily through the vug domain due to the lower capillary resistance these cavities offer.

The first mechanism would explain the high relative permeability to oil in all micromodels (with and without vugs). Whereas, the exclusive increase in the relative permeability to water in the vugular media would come as a consequence of the second mechanism.

The experimental study conducted by Kusanagi et al. [21] on vuggy carbonate rocks had already reported alterations in the shape of steady-state non-wetting phase relative permeability curves and their dependence on vug connectivity. However, direct comparisons with the relative permeability of the porous matrix without vugs have only been conducted through theoretical studies by Moctezuma-Berthier et al. [9] and Akin and Erzeybek [69]. In our microfluidic approach to an oil-wet vugular porous medium, increases in the relative permeability to the non-wetting phase and no changes in the relative permeability to the wetting phase are evidenced for the first time with respect to an identical porous medium without vugs.

Regarding the configuration of the vugular space, and based on the characteristics of the relative permeability to water attained in the vugular porous media T_1 (7.5% macroporosity of non-elongated, non-touching vugs), it should be noted that neither increases in macroporosity (higher number of vugs in T_3) nor changes in the geometry of vugs (more elongated vugs in T_2) cause additional increases in the relative permeability to water.

It is presumed that the considered changes in the vugular configuration of micromodels T_2 and T_3 are not drastic enough to alter the distribution of the aqueous phase in the porous space in such a way that the relative permeability of the heterogeneous porous medium becomes further sensitive. The latter is consistent with the observations of Kusanagi et al. [21] in rock samples with non-touching vugs distributed throughout the core body, for which the relative permeability curves did not change significantly among samples.

Figure 5.24 addresses an alternative representation of the relative permeability values collected from the porous media micromodels. The relative permeability to water ($K_{r,w}$) is mapped to the relative permeability to oil ($K_{r,o}$). On this basis, in addition to the clear increase of $K_{r,w}$ in all vugular porous media, it is confirmed that $K_{r,w}$ is even somewhat higher in the micromodel T_2 . The more elongated shape of the vugs, aligned in the main flow direction, would lead to a more effective transport of the aqueous phase towards the outlet of the porous medium.

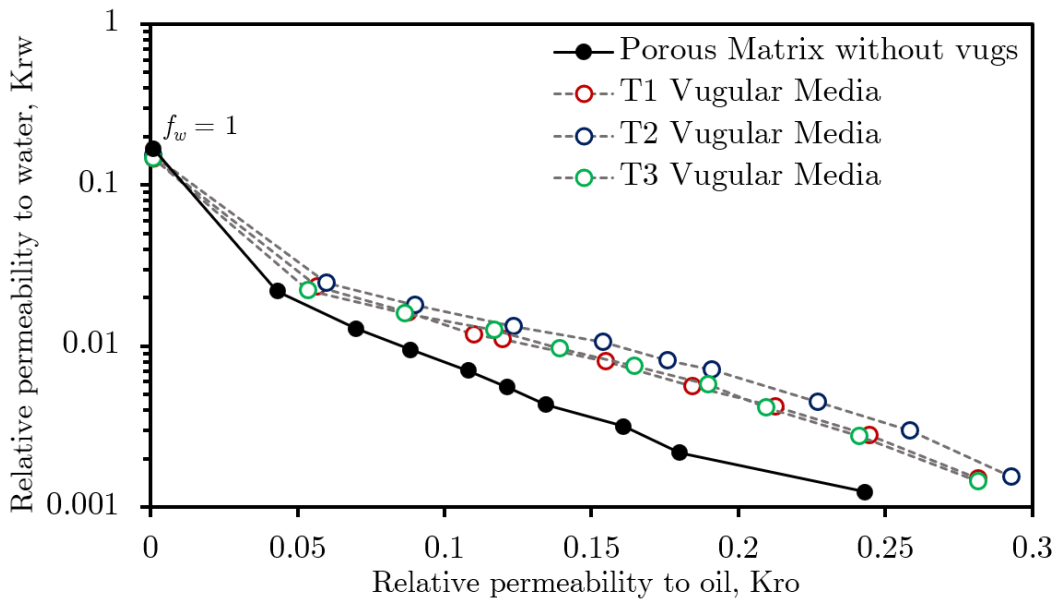


Figure 5.24: Relative permeability to the aqueous phase ($K_{r,w}$) as a function of the relative permeability to the oleic phase ($K_{r,o}$) in the porous matrix without vugs and in the vugular porous media micromodels.

On the other hand, it is worth noting that during the flow of water and oil, the higher relative permeability to water in the vugular porous media is what leads to the oil saturation in the porous matrix domain ending up higher than the remaining oil saturation in the porous matrix micromodel without vugs. Table 5.1 lists the remaining oil saturations and the endpoint relative (and effective) permeabilities to water.

Table 5.1: Characteristics of the *water relative permeability endpoints* in the porous media micromodels. $S_{o,1}$ is the remaining oil saturation in the whole porous medium, $S_{o,2}$ is the remaining oil saturation in the porous matrix domain, $K_{eff,w}$ is the effective permeability to water, and $K_{r,w}$ is the relative permeability to water.

Micromodel	$S_{o,1}$	$S_{o,2}$	$K_{eff,w}$ (Da)	$K_{r,w}$
Porous Matrix without vugs	0.253	0.253	18.62	0.167
T_1 Vugular Media	0.234	0.269	21.76	0.146
T_2 Vugular Media	0.244	0.303	29.6	0.153
T_3 Vugular Media	0.217	0.268	24.07	0.147

At the *endpoint of the relative permeability to water* (highest value of S_w), a contrasting behavior is observed. $K_{r,w}$ in the vugular media becomes lower than that in the porous matrix without vugs. The vug contribution to improve water transmission through the whole porous medium seems to have been mitigated by the higher degree of connectivity that is already attained in the porous matrix domain.

In Section 5.1, it was seen that the hydraulic properties of the porous media micromodels are sensitive to the configuration of the pore space by means of the equivalent absolute permeability. In this section, the concept was extended to relative permeability, which normalizes the absolute values of effective permeabilities to water and to oil with respect to the intrinsic equivalent absolute permeability of each porous media configuration.

In that regard, despite the fact that the inclusion of vugs does not affect the relative permeability to oil and that, at the endpoint, the relative permeability to water is higher in the porous matrix without vugs, the intrinsic capacity for transmission of water and oil is confirm to be higher in the vugular porous media. Moreover, depending on the configuration of the vugular space, it follows the same increasing trend as the equivalent absolute permeability by higher macroporosity and by more elongated vugs. The effective permeabilities to water at the endpoint are listed in Table 5.1 and exemplify the trends previously described.

5.8

Evaluation of oil displacement by water injection in the porous media micromodels with and without vugs

Oil displacement experiments by water injection ($f_w = 1$) were performed in the porous media micromodels. In this case, the capillary number of the aqueous phase was set at $Ca = 10^{-5}$ and the oil-to-water viscosity ratio was increased to $M \sim 250$ by using a higher viscosity oleic phase.

Figure 5.25 details the oil saturations at the water breakthrough (*WBT*) and at the steady state (*SS*) in the porous matrix without vugs and in the vugular porous media. The steady-state water/oil distributions are display in Figure 5.26.

In the porous matrix without vugs, the invasion of water into the pore space leads to the growth of advancing fingers in the main flow direction. These fingers eventually converge into a single central flow pathway that percolates the porous medium and leaves behind large lateral banks of oil. The water breakthrough is reached at 0.16 pore volumes (PV) of injected water, at which the remaining oil saturation is 0.84.

In the vugular porous media micromodels, instead, the water breakthrough is reached at 0.31 (T_1), 0.22 (T_2) and 0.32 (T_3) PV of injected water. The presence of vugs in the porous matrix prevents the convergence of the advancing fingers into a central flow pathway, diverting them toward the vugs. As note in the previous sections, and based on the oil-wet nature of micromodels, the flowing aqueous phase preferentially occupies the vug domain. Accordingly, vugs are sequentially saturated with water, and while saturated, the water front remains immobile in the porous matrix. These observations are consistent with those reported by Vik et al. [15], Dabbouk et al. [27] and Pairoys et al. [68] from drainage experiments in vuggy core-samples.

Both in the T_1 and T_3 vugular media, 80% of the original oil in the vug domain has already been drained at the *WBT*, and the oil saturation in the porous matrix domain is lower than in the porous matrix without vugs. Smaller vugs scattered throughout the porous medium promote movement of advancing fingers into a broader region of the pore space and therefore more efficient early drainage. This is not the case in the T_2 vugular medium, in which the transport of water through elongated vugs, aligned in the main flow direction, hinders the drainage of the porous matrix.

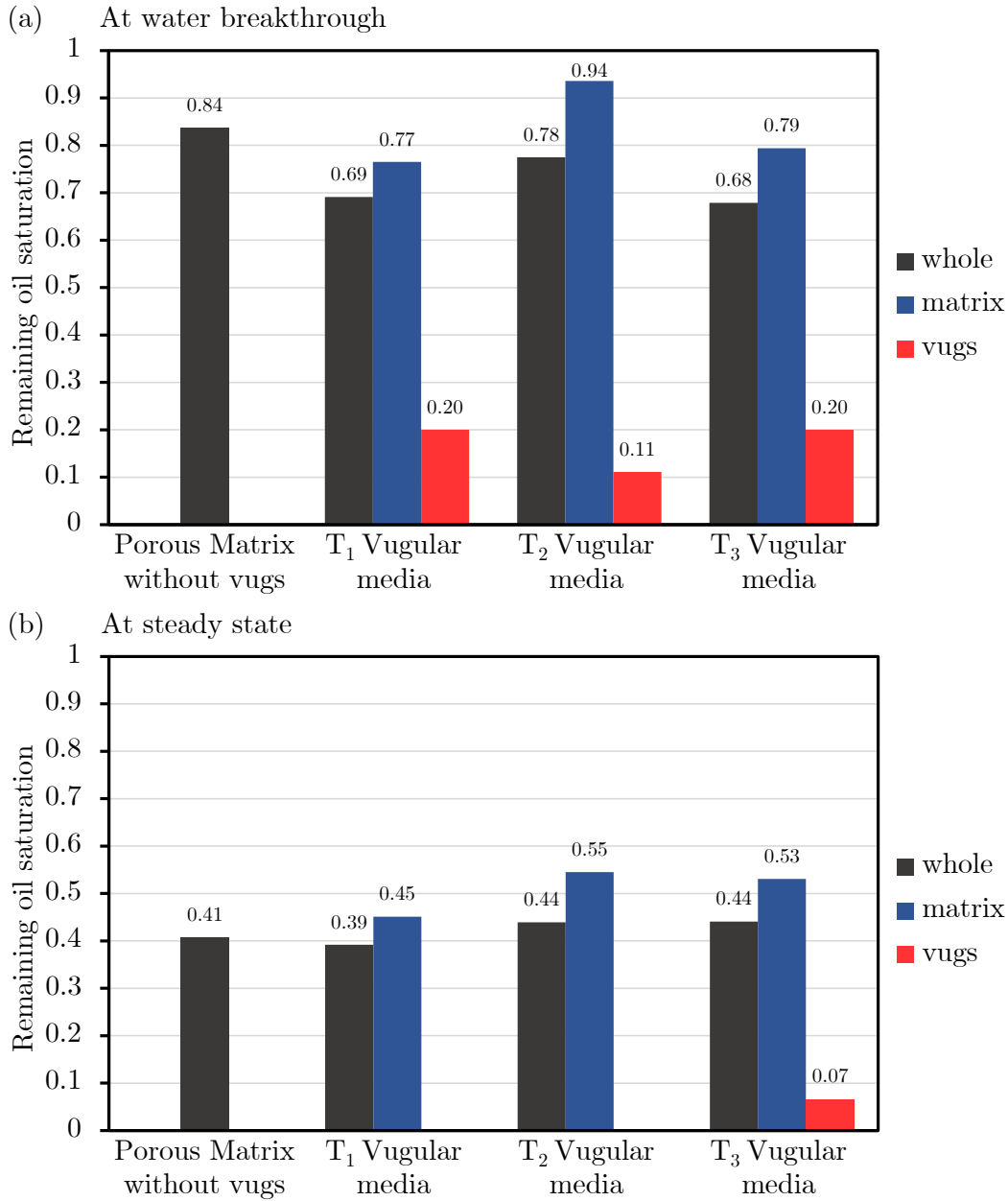


Figure 5.25: Remaining oil saturation in the porous media micromodels after water injection up to (a) water breakthrough and (b) steady state. In vugular media, oil saturation is quantified in each porosity domain, i.e., porous matrix and vugs.

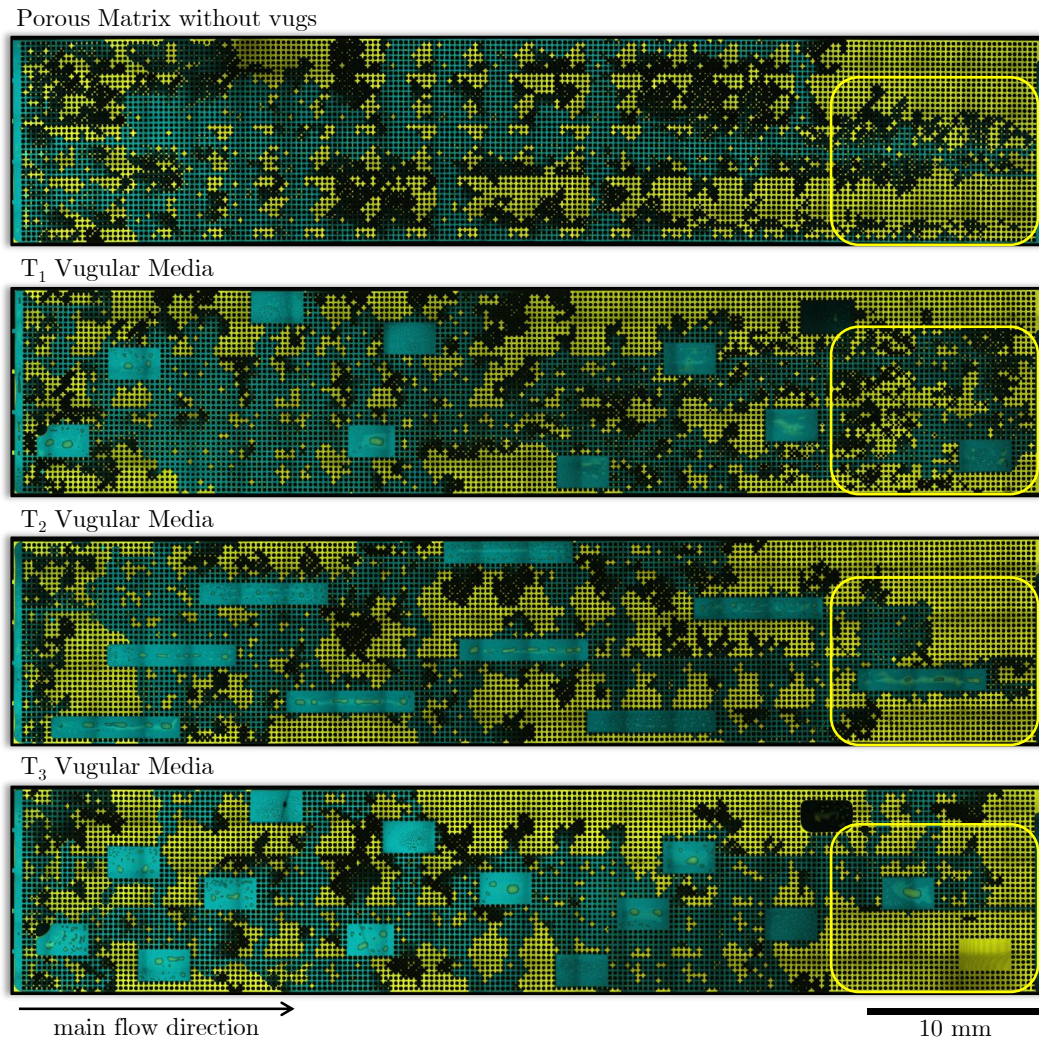


Figure 5.26: Steady-state water/oil distributions in the porous media micro-models with and without vugs after water injection. Vug inclusions modify the water pathways in the porous matrix, preventing oil drainage. This phenomenon is highlighted in the yellow square.

After the *WBT*, oil recovery is maintained in the long term. The oil saturation values reported in Figure 5.25 demonstrate that in the porous matrix micromodel without vugs, more than 40% of the original oil in place is additionally recovered after the injection of 15 PV of water (at which there are no further changes in the remaining oil saturation). This behavior is characteristic of oil-wet porous media, in which oil recovery before the *WBT* is relatively small, and therefore more water must be injected to recover larger amounts of oil [51].

The water/oil distributions in Figure 5.26 reveal that in the vugular micromodels, even if the vug domain is almost completely drained at *SS*, the porous matrix domain is less efficiently drained in the long term. The steady-state values reported in Figure 5.25 confirm the higher remaining oil

saturations in the porous matrix of all vugular media. These results suggest that once the oil-wet vugular porous medium is percolated by water, further displacement of the aqueous phase towards unswept regions of the porous matrix is prevented by the presence of vugs.

Regarding the effect of the vugular space configuration on the oil displacement dynamics, it is found that more elongated vugs (in the micromodel T_2) and a higher number of non-elongated vugs (in the micromodel T_3) led to less efficient oil displacement by water injection. On this basis, oil recovery in the micromodels T_2 and T_3 was measured to be 45% and 47%, respectively; while in the micromodel T_1 and in the porous matrix without vugs, 55% and 59%, respectively.

At steady state, large pockets of oil are left in regions lateral to the vug position or between unaligned neighboring vugs. Moreover, it is worth noting that oil recovery is highly sensitive to the location of the isolated vugs in the porous matrix. In T_1 and T_3 micromodels, for example, the inclusion of an additional vug near the outlet of the porous medium completely modifies the trajectory of the water flow, preventing oil drainage in an extensive region of the porous matrix. This phenomenon is highlighted in a yellow square in Figure 5.26.

The observations gathered from the oil displacement experiments by water injection are consistent with the conventional wisdom on reduced sweep efficiency in heterogeneous porous media. However, it is remarkable that despite the increased relative permeability to water in the vugular media, the higher remaining oil saturations are not caused by an earlier water breakthrough when compared to the porous matrix without vugs, but due to less efficient oil displacement through the oil-wet porous medium after the water breakthrough.

6

Conclusions

This chapter presents the conclusions and final considerations drawn from the study of two-phase flow in micromodels of vugular porous media.

1. Different configurations of 2D porous media micromodels were designed and successfully fabricated in-house using standard soft lithography techniques. The surface wettability of micromodels was verified to be oil-wet, and their pore space and geometric attributes were fully characterized by means of high-resolution confocal microscopy.

2. Absolute permeability measurements highlighted the reliability of quantifying the pressure drop across the porous media micromodels and the sensitivity of their porous matrix to the inclusion of non-touching vugs. Higher equivalent absolute permeabilities (by up to 68%) were observed, especially in micromodels with elongated vugs ($AR = 6.2$) and higher macroporosity ($\phi_v = 0.11$).

3. A comprehensive methodology of co-injection of water and oil into the porous media micromodels was developed in order to visualize the two-phase flow behavior at the pore scale and characterize the distribution of fluids in the whole porous medium. Based on this methodology, fluid saturations were quantified and the morphology of oil ganglia was determined. Realistic fluid flow phenomena of porous media were identified, e.g., the intermittent pore occupancy by the non-wetting phase during steady state two-phase flow, and the formation of pendular rings of the wetting phase as the saturation of this fluid is reduced.

4. Combining reliable pressure drop measurement with high-resolution fluid distribution images, steady-state relative permeability curves of the porous media micromodels were determined. The relative permeability to oil was found to be higher than the relative permeability to water even at elevated fractional flows of water (i.e., 0.9). The pore-scale observations corroborated that oil flows wetting the walls of the pore space and, therefore, its movement through the porous matrix is expected to be mainly driven by capillary forces.

5. By comparing the relative permeability in vugular porous media against the results obtained from an equivalent porous matrix without vugs, we state that the inclusion of vugs leads to:

- ✘ Lower pressure drop during two-phase flow, since the effective transmission capacity through the whole porous medium is improved;
- ✘ Increased oil saturation in the porous matrix as larger oil ganglia remain due to less efficient drainage process;
- ✘ Higher relative permeability to water, which flows preferentially through the vugs;
- ✘ Progressive saturation of the vugular space with water as the fractional flow of this phase is increased;
- ✘ No change in the relative permeability to oil, which flows preferentially through the porous matrix due to surface wettability;
- ✘ No further sensitivity in relative permeability curves to increases in the number of vugs (ϕ_v from 0.08 to 0.11) or in the vug length (AR from 1.7 to 6.2).

6. During oil displacement experiments by water injection, the presence of vugs in the porous media micromodels diverted the expected water flow pathways through the porous matrix. In that regard, the remaining oil saturation was affected by the distribution and geometry of the vugs, as follows:

- ✘ Prior to the water breakthrough, the presence of smaller vugs throughout the whole porous medium ($AR = 1.7$ at $\phi_v = 0.08$ and 0.11) contributed to a more extended water invasion into the porous matrix, leading to an early drainage more efficient. 15% more oil was recovered from the porous matrix compared to the porous matrix without vugs, and up to 80% of the oil stored in the vugs was also drained.
- ✘ After the water breakthrough, instead, these vugs distributions attenuated the long-term oil displacement typical of oil-wet systems, leading to a late drainage less efficient. 12% less oil was recovered from the porous matrix compared to the porous matrix without vugs.
- ✘ Most importantly, elongated vugs ($AR = 6.2$), aligned in the main flow direction, facilitated the transport of water across the whole porous medium, hindering the invasion of water into the porous matrix. Both the early and late drainage were less efficient, with up to 14% less oil recovered from the porous matrix.

7. In order to demonstrate the quality of the relative permeability measurements in vugular porous media presented in this work, estimates of the representative elementary volume must be carried out. Micromodels with porous media in various sizes can be manufactured maintaining the same porosity of the porous matrix domain, and both the same macroporosity and vug geometry of the vugs domain. It is presumed that the distribution of the vugs could play a fundamental role, so several random distributions should be considered for the same size of porous medium, matrix porosity, macroporosity and vug geometry.

8. Our low-cost microfluidic approach to heterogeneous porous media opens up new opportunities to systematically study more complex porous network and fluid systems. It is expected that relative permeability curves of vugular and fractured porous media can be determined based on the relative permeability curves of the porous matrix and the morphology of the vug and fracture domains. More importantly, it is contemplated that the collected experimental data may be useful for the validation of numerical simulations of single and two-phase flow in heterogeneous porous media.

Bibliography

- [1] DOMINGUEZ, G. C.; FERNANDO, S. V. ; CHILINGARIAN, G. V.. **Chapter 12 simulation of carbonate reservoirs**. In: Chilingarian, G.; Mazzullo, S. ; Rieke, H., editors, **CARBONATE RESERVOIR CHARACTERIZATION: A GEOLOGIC-ENGINEERING ANALYSIS, PART I**, volumen 30 de **Developments in Petroleum Science**, p. 543–588. Elsevier, 1992.
- [2] HIDAJAT, I.; MOHANTY, K.; FLAUM, M. ; HIRASAKI, G.. **Studdy of vuggy carbonates using nmr and x-ray ct scanning**. **SPE Reservoir Evaluation & Engineering**, 7, 04 2013.
- [3] YAO, J.; HUANG, Z.-Q.. **Fractured Vuggy Carbonate Reservoir Simulation**, p. 1–8. Springer Berlin Heidelberg, Berlin, Heidelberg, 2016.
- [4] AZERÊDO, A. C.; DUARTE, L. V. ; SILVA, A. P.. **The challenging carbonates from the pre-salt reservoirs offshore brazil: facies, palaeoenvironment and diagenesis**. **Journal of South American Earth Sciences**, 108:103202, 2021.
- [5] SOLTANMOHAMMADI, R.; IRAJI, S.; ALMEIDA, T.; RUIDIAZ, E.; FIORAVANTI, A. ; VIDAL, A.. **Insights into multi-phase flow pattern characteristics and petrophysical properties in heterogeneous porous media**. p. 1–5, 01 2021.
- [6] LUCIA, F.. **Petrophysical Parameters Estimated From Visual Descriptions of Carbonate Rocks: A Field Classification of Carbonate Pore Space**. **Journal of Petroleum Technology**, 35(03):629–637, 03 1983.
- [7] VIK, B.; DJURHUUS, K.; SPILDO, K. ; SKAUGE, A.. **Characterisation of Vuggy Carbonates**. **SPE Reservoir Characterisation and Simulation Conference and Exhibition**, 10 2007.
- [8] LUCIA, F. J.. **Rock-Fabric/Petrophysical Classification of Carbonate Pore Space for Reservoir Characterization1**. **AAPG Bulletin**, 79(9):1275–1300, 09 1995.

- [9] MOCTEZUMA-BERTHIER, A.; VIZIKA, O.; THOVERT, J.-F. ; ADLER, P.. **One- and two-phase permeabilities of vugular porous media.** *Transport in Porous Media*, 56:225–244, 08 2004.
- [10] BRUNSON, D.. **Simulating Fluid Flow In Vuggy Porous Media.** PhD thesis, Faculty of the Graduate School of The University of Texas, Austin, United States of America, 8 2005.
- [11] WU, Y.-S.; DI, Y.; KANG, Z. ; FAKCHAROENPHOL, P.. **A multiple-continuum model for simulating single-phase and multiphase flow in naturally fractured vuggy reservoirs.** *Journal of Petroleum Science and Engineering*, 78(1):13–22, 2011.
- [12] EHRLICH, R.. **Relative Permeability Characteristics of Vugular Cores - Their Measurement and Significance.** volumen All Days de SPE Annual Technical Conference and Exhibition, 10 1971.
- [13] DEZABALA, E.; KAMATH, J.. **Laboratory Evaluation of Waterflood Behavior of Vugular Carbonates.** volumen All Days de SPE Annual Technical Conference and Exhibition, 10 1995.
- [14] MOCTEZUMA-BERTHIER, A.; VIZIKA, O. ; ADLER, P.. **Water–oil relative permeability in vugular porous media: experiments and simulations.** In: SCA INTERNATIONAL SYMPOSIUM OF THE SOCIETY OF CORE ANALYSTS, MONTEREY, CA, p. 22–26, 2002.
- [15] VIK, B.; BASTESSEN, E. ; SKAUGE, A.. **Evaluation of representative elementary volume for a vuggy carbonate rock — part i: Porosity, permeability, and dispersivity.** *Journal of Petroleum Science and Engineering*, 112:36–47, 2013.
- [16] ROSA, A.; DE SOUZA CARVALHO, R. ; XAVIER, J.. **Engenharia de reservatórios de petróleo.** Interciência, 2006.
- [17] HUANG, Z.; YAO, J.; LI, Y.; WANG, C. ; LÜ, X.. **Permeability analysis of fractured vuggy porous media based on homogenization theory.** *Science China Technological Sciences*, 53:839–847, 03 2010.
- [18] KUSANAGI, H.; WATANABE, N.; SHIMAZU, T. ; YAGI, M.. **Permeability-Porosity Relation and Preferential Flow in Heterogeneous Vuggy Carbonates.** volumen All Days de SPWLA Formation Evaluation Symposium of Japan, 10 2015.

- [19] ARCHER, J. S.; WONG, S.. **Use of a Reservoir Simulator To Interpret Laboratory Waterflood Data.** Society of Petroleum Engineers Journal, 13(06):343–347, 12 1973.
- [20] KAMATH, J.; NAKAGAWA, F.; MEYER, R.; KABIR, S. ; HOBLET, R.. **Laboratory evaluation of waterflood residual oil saturation in four carbonate cores.** Paper SCA, 12(2001):80, 2001.
- [21] KUSANAGI, H.; WATANABE, N.; SHIMAZU, T. ; YAGI, M.. **Relative Permeability Curves for Two-Phase Flows Through Heterogeneous Vuggy Carbonates.** volumen All Days de SPWLA Formation Evaluation Symposium of Japan, 09 2016.
- [22] ARBOGAST, T.; BRUNSON, D.; BRYANT, S. ; JENNINGS, J.. **A preliminary computational investigation of a macro-model for vuggy porous media.** In: Miller, C. T.; Farthing, M. W.; Gray, W. G. ; Pinder, G. F., editors, COMPUTATIONAL METHODS IN WATER RESOURCES: VOLUME 1, volumen 55 de **Developments in Water Science**, p. 267–278. Elsevier, 2004.
- [23] POPOV, P.; EFENDIEV, Y. ; QIN, G.. **Multiscale modeling and simulations of flows in naturally fractured karst reservoirs.** Communications in computational physics, 6(1):162, 2009.
- [24] HUANG, Z.; YAO, J.; LI, Y.; WANG, C. ; LV, X.. **Numerical calculation of equivalent permeability tensor for fractured vuggy porous media based on homogenization theory.** Communications in Computational Physics, 9(1):180–204, 2011.
- [25] DALI, M.. **Flow in porous media with macropores using brinkman’s model.** Master’s thesis, Mechanical Engineering Department of PUC-Rio, 2019.
- [26] OKABE, H.; BLUNT, M. J.. **Pore space reconstruction of vuggy carbonates using microtomography and multiple-point statistics.** Water Resources Research, 43(12), 2007.
- [27] DABBOUK, C.; ALI, L.; WILLIAMS, G. ; BEATTIE, G.. **Waterflood in Vuggy Layer of a Middle East Reservoir - Displacement Physics Understood.** volumen All Days de Abu Dhabi International Petroleum Exhibition and Conference, 10 2002.
- [28] KUSANAGI, H.; WATANABE, N.; SHIMAZU, T.; YAGI, M.; KOMAI, T. ; TSUCHIYA, N.. **X-ray ct based numerical analysis for fluid flows**

- through vuggy carbonate cores. In: SPWLA 20TH FORMATION EVALUATION SYMPOSIUM OF JAPAN. OnePetro, 2014.
- [29] CRUZ, R. F.. **Numerical evaluation of equivalent permeability in 3d vuggy porous media using brinkman model.** Master's thesis, Mechanical Engineering Department of PUC-Rio, 2020.
- [30] CHATENEVER, A.; CALHOUN, JOHN C., J.. **Visual Examinations of Fluid Behavior in Porous Media - Part I.** Journal of Petroleum Technology, 4(06):149–156, 06 1952.
- [31] KUMAR GUNDA, N. S.; BERA, B.; KARADIMITRIOU, N. K.; MITRA, S. K. ; HASSANIZADEH, S. M.. **Reservoir-on-a-chip (roc): A new paradigm in reservoir engineering.** Lab Chip, 11:3785–3792, 2011.
- [32] XU, W.; OK, J. T.; XIAO, F.; NEEVES, K. B. ; YIN, X.. **Effect of pore geometry and interfacial tension on water-oil displacement efficiency in oil-wet microfluidic porous media analogs.** Physics of Fluids, 26(9):093102, 2014.
- [33] BEAR, J.. **Dynamics of Fluids in Porous Media.** Dover Civil and Mechanical Engineering. Dover Publications, 2013.
- [34] CHHABRA, R.; RICHARDSON, J.. **Chapter 5 - particulate systems.** In: Chhabra, R.; Richardson, J., editors, NON-NEWTONIAN FLOW AND APPLIED RHEOLOGY (SECOND EDITION), p. 249–315. Butterworth-Heinemann, Oxford, second edition edition, 2008.
- [35] DULLIEN, F.. **Porous Media Fluid Transport and Pore Structure.** Elsevier Science, 2012.
- [36] COREY, A.. **Mechanics of Immiscible Fluids in Porous Media.** Water Resources Publications, 1994.
- [37] RIGBY, S. P.; FLETCHER, R. S.; RAISTRICK, J. H. ; RILEY, S. N.. **Characterisation of porous solids using a synergistic combination of nitrogen sorption, mercury porosimetry, electron microscopy and micro-focus x-ray imaging techniques.** Phys. Chem. Chem. Phys., 4:3467–3481, 2002.
- [38] SIBIRYAKOV, B.; LEITE, L. ; SIBIRIAKOV, E.. **Porosity, specific surface area and permeability in porous media.** Journal of Applied Geophysics, 186:104261, 2021.

- [39] HONARPOUR, M.; MAHMOOD, S.. **Relative-Permeability Measurements: An Overview**. Journal of Petroleum Technology, 40(08):963–966, 08 1988.
- [40] AHMED, U.; CRARY, S. ; COATES, G.. **Permeability Estimation: The Various Sources and Their Interrelationships**. Journal of Petroleum Technology, 43(05):578–587, 05 1991.
- [41] HOFFMANN, M. R.. **Macroscopic equations for flow in unsaturated porous media**. Wageningen University and Research, 2003.
- [42] BEAR, J.; BACHMAT, Y.. **Introduction to Modeling of Transport Phenomena in Porous Media**. Theory and Applications of Transport in Porous Media. Springer Netherlands, 2012.
- [43] FARAMARZI-PALANGAR, M.; MIRZAEI-PAIAMAN, A.; GHOREISHI, S. A. ; GHANBARIAN, B.. **Wettability of carbonate reservoir rocks: A comparative analysis**. Applied Sciences, 12(1), 2022.
- [44] LAURÉN, S.. **How to alter wettability in carbonate reservoir?**, 2019.
- [45] RUIDIAZ, E.; WINTER, A. ; TREVISAN, O.. **Oil recovery and wettability alteration in carbonates due to carbonate water injection**. Journal of Petroleum Exploration and Production Technology, 8, 04 2017.
- [46] MELROSE, J.. **Role of capillary forces in detennining microscopic displacement efficiency for oil recovery by waterflooding**. Journal of Canadian Petroleum Technology - J CAN PETROL TECHNOL, 13, 10 1974.
- [47] LØVOLL, G.; MÉHEUST, Y.; MÅLØY, K.; AKER, E. ; SCHMITTBUHL, J.. **Competition of gravity, capillary and viscous forces during drainage in a two-dimensional porous medium, a pore-scale study**. Energy, 30:861–872, 05 2005.
- [48] LENORMAND, R.; TOUBOUL, E. ; ZARCONE, C.. **Numerical models and experiments on immiscible displacements in porous media**. Journal of Fluid Mechanics, 189:165–187, 1988.
- [49] NIASAR, V.; HASSANIZADEH, S.. **Analysis of fundamentals of two-phase flow in porous media using dynamic pore-network models: A review**. Critical Reviews in Environmental Science and Technology, 42:1895–1976, 09 2012.

- [50] LENORMAND, R.; LENORMAND, G.. **Recommended procedure for determination of relative permeabilities**. International Symposium of the Society of Core Analysts, 08 2016.
- [51] ANDERSON, W. G.. **Wettability Literature Survey Part 5: The Effects of Wettability on Relative Permeability**. Journal of Petroleum Technology, 39(11):1453–1468, 11 1987.
- [52] KANTZAS, A.; BRYAN, J. ; TAHERI, S.. **Fundamentals of fluid flow in porous media**, 2022.
- [53] REYNOLDS, C.; MENKE, H.; ANDREW, M.; BLUNT, M. ; KREVOR, S.. **Dynamic fluid connectivity during steady-state multiphase flow in a sandstone**. Proceedings of the National Academy of Sciences, 114, 07 2017.
- [54] GAO, Y.; Q. RAEINI, A.; BLUNT, M. ; BIJELJIC, B.. **Dynamic fluid configurations in steady-state two-phase flow in bentheimer sandstone**. Physical Review E, 103, 01 2021.
- [55] KOKAL, S.; AL-KAABI, A.. **Enhanced oil recovery: challenges & opportunities**. World Petroleum Council: Official Publication, 64:64–69, 2010.
- [56] KARGOZARFARD, Z.; RIAZI, M. ; AYATOLLAHI, S.. **Viscous fingering and its effect on areal sweep efficiency during waterflooding: an experimental study**. Petroleum Science, 16, 10 2018.
- [57] AVENDAÑO, J.; LIMA, N.; QUEVEDO, A. ; CARVALHO, M.. **Effect of surface wettability on immiscible displacement in a microfluidic porous media**. Energies, 12(4), 2019.
- [58] GUTIERREZ CASTILLO, E. B.. **Modeling with hysteresis for oil reservoir simulation**. Master's thesis, Delft University of Technolog, 2016.
- [59] MARKOV, M.; KAZATCHENKO, E.; MOUSATOV, A. ; PERVAGO, E.. **Permeability of the fluid-filled inclusions in porous media**. Transport in Porous Media, 84:307–317, 09 2010.
- [60] CONSULTANTS, S.. **Skill target: Quantifying multiple porosity types in a carbonate reservoir**, 2022.
- [61] HIDAJAT, I.; MOHANTY, K. K.; FLAUM, M. ; HIRASAKI, G.. **Study of Vuggy Carbonates Using NMR and X-Ray CT Scanning**. SPE Reservoir Evaluation Engineering, 7(05):365–377, 10 2004.

- [62] GAO, Y.; LIN, Q.; BIJELJIC, B. ; BLUNT, M.. **X-ray microtomography of intermittency in multiphase flow at steady state using a differential imaging method.** *Water Resources Research*, 53, 11 2017.
- [63] SPURIN, C.; BULTREYS, T.; BIJELJIC, B.; BLUNT, M. ; KREVER, S.. **Intermittent fluid connectivity during two-phase flow in a heterogeneous carbonate rock.** *Physical Review E*, 100, 10 2019.
- [64] PAL, M.. **A unified approach to simulation and upscaling of single-phase flow through vuggy carbonates.** *International Journal for Numerical Methods in Fluids*, 69:1096–1123, 06 2012.
- [65] GOLFIER, F.; LASSEUX, D. ; QUINTARD, M.. **Investigation of the effective permeability of vuggy or fractured porous media from a darcy-brinkman approach.** *Computational Geosciences*, 19:63–78, 02 2015.
- [66] COREY, A. T.; RATHJENS, C.. **Effect of stratification on relative permeability.** *Journal of Petroleum Technology*, 8(12):69–71, 1956.
- [67] JOHNSON, E.; BOSSLER, D. ; BOSSLER, V. N.. **Calculation of Relative Permeability from Displacement Experiments.** *Transactions of the AIME*, 216(01):370–372, 12 1959.
- [68] PAIROYS, F.; LASSEUX, D. ; BERTIN, H.. **An experimental and numerical investigation of water-oil flow in vugular porous media.** *Symp. Soc. Core Analysts. Pau, France*, 09 2003.
- [69] AKIN, S.; ERZEYBEK, S.. **Pore Network Modeling of Two Phase Flow in Vuggy Carbonates.** *volumen All Days de SPE Europec featured at EAGE Conference and Exhibition*, 06 2008.
- [70] SCHIOZER, D.; MUÑOZ MAZO, E.. **Modeling fracture relative permeability - what is the best option?** 06 2013.
- [71] BERG, S.; RUECKER, M.; OTT, H.; GEORGIADIS, A.; LINDE, H.; ENZMANN, F.; KERSTEN, M.; ARMSTRONG, R.; WITH, S.; BECKER, J. ; WIEGMANN, A.. **Connected pathway relative permeability from pore-scale imaging of imbibition.** *Advances in Water Resources*, 90, 02 2016.
- [72] GAO, Y.; QASEMINEJAD RAEINI, A.; BLUNT, M. J. ; BIJELJIC, B.. **Pore occupancy, relative permeability and flow intermittency measurements using x-ray micro-tomography in a complex carbonate.** *Advances in Water Resources*, 129:56–69, 2019.

- [73] SPURIN, C.; BULTREYS, T.; RÜCKER, M.; GARFI, G.; SCHLEPÜTZ, C. M.; NOVAK, V.; BERG, S.; BLUNT, M. J. ; KREYER, S.. **The development of intermittent multiphase fluid flow pathways through a porous rock.** *Advances in Water Resources*, 150:103868, 2021.
- [74] XIA, Y.; WHITESIDES, G. M.. **Soft lithography.** *Annual Review of Materials Science*, 28(1):153–184, 1998.
- [75] MCDONALD, C.; WHITESIDES, G.. **Poly(dimethylsiloxane) as a material for fabricating microfluidic devices.** *Accounts of Chemical Research*, 35:491–499, 07 2002.
- [76] BHATTACHARYA, S.; DATTA, A.; BERG, J. ; GANGOPADHYAY, S.. **Studies on surface wettability of poly(dimethyl) siloxane (pdms) and glass under oxygen-plasma treatment and correlation with bond strength.** *Journal of Microelectromechanical Systems*, 14(3):590–597, 2005.
- [77] BACHAROUCHE, J.; HAIDARA, H.; KUNEMANN, P.; VALLAT, M.-F. ; ROUCOULES, V.. **Singularities in hydrophobic recovery of plasma treated polydimethylsiloxane surfaces under non-contaminant atmosphere.** *Sensors and Actuators A: Physical*, 197:25–29, 2013.
- [78] ABERA, K. A.; MANAHILOH, K. N. ; MOTALLEB NEJAD, M.. **The effectiveness of global thresholding techniques in segmenting two-phase porous media.** *Construction and Building Materials*, 142:256–267, 2017.